The Dissertation Committee for Ashish Kumar
Certifies that this is the approved version of the following Dissertation:

Coupling Geomechanics with Flow and Tracer Transport in Complex Fracture Networks

Committee:

Mukul M. Sharma, Supervisor

Kishore Mohanty

Matthew Balhoff

Ryosuke Okuno

Roger Bonnecaze

Coupling Geomechanics with Flow and Tracer Transport in Complex Fracture Networks

by

Ashish Kumar

Dissertation

Presented to the Faculty of the Graduate School of

The University of Texas at Austin

in Partial Fulfillment

of the Requirements

for the Degree of

Doctor of Philosophy

The University of Texas at Austin

December 2020

Dedication

Dedicated to my family for their sacrifices, unconditional love, and encouragement.

Acknowledgments

First and foremost, I would like to express my sincere gratitude to my advisor, Dr. Mukul Sharma, for his invaluable guidance and consistent support throughout my doctoral studies at UT Austin. It has been a pleasure to work under Dr. Sharma and contribute to cutting edge research in hydraulic fracturing. Dr. Sharma offered me full flexibility to explore and choose my research topics and helped me to accomplish those through his supervision and continuous encouragement. I would also like to thank Professors Dr. Mohanty, Dr. Balhoff, Dr. Okuno, and Dr. Bonnecaze for taking their time out to serve on my dissertation committee and provide their invaluable insight and knowledge to improve my research.

I am extremely fortunate to work alongside many exceptional members of Dr. Sharma's research group. I want to thank Dr. Kaustubh Shrivastava for the brainstorming to explore new ideas and collaboration to accomplish them. I would like to mention special thanks to Dr. Ripudaman Manchanda for all the help during OpenFOAM learning. I am really thankful to Dr. Sho Hirose and Shuang for assistance related to C++ and the model debugging. It was a pleasure to discuss and collaborate with Puneet, Brendan, Dr. Deepen Gala, and Dr. Shivam Agrawal.

I appreciate the admin staff at UT PGE, particularly Jin Lee, Amy Stewart, and Frankie Hart, for their support. Special thanks to Jin Lee, who was always ready to help with any administrative issue a student can have.

Of course, I would not have been able to make it so far without the company of my great friends in Austin. I thank Manoj, Madhura, Prasanna, Avani, Ajit, Isha, Soham, Anil, Azmin, Nagaraja, Prajwala, Esha, Saurabh, and others for a lot of enjoyable events. I would

also like to mention my friends who were just a call away to provide me moral support whenever I needed them. Special thanks to Pradeep, Ankur, Ashish, Rajat, Nityendra, and Rakesh. Their friendship helped me to keep me motivated during difficult times.

I will always be grateful to my parents, siblings, parents in law for their sacrifices, unconditional love, and support. Without their sacrifices, this work would not have been possible. Pride and affection from my cousins, sister in law, and brother in law helped me to keep going on the right path. Last but not least, thanks to my wife Trisha Sinha, for her love, care, support, and always believing in me. Her continuous encouragement helped me to work hard to accomplish my objectives. I thank god for providing me the backing of such a great team.

Abstract

Coupling Geomechanics with Flow and Tracer Transport in Complex Fracture Networks

Ashish Kumar, Ph.D.

The University of Texas at Austin, 2020

Supervisor: Mukul M. Sharma

Hydraulic fracturing in horizontal wells has enabled economic production from ultra-low permeability reservoirs. The productivity of these hydraulically fractured wells depends on the fracture dimensions, conductivity, connectivity to the wellbore, and applied drawdown pressure. Traditional numerical simulation models used to analyze the productivity of hydraulically fractured wells assume a planar bi-wing fracture that is open and connected to the wellbore. However, several core-through field studies and fracture propagation models have demonstrated that a hydraulic fracturing process can create non-planar complex fracture networks. The conductivity and connectivity of these complex fractures are highly dependent on the in-situ stress changes due to production. Hence it is critical to consider complex fractures and the impact of geomechanics in the simulation models for analyzing fractured well productivity.

A finite-volume method based geomechanics coupled reservoir model was developed to simulate production from complex fracture networks. An automated meshing method was developed to create the reservoir, and fracture mesh for any given arbitrarily

shaped fracture network. The reservoir-fracture network model accounts for fracture closure effects during production. The model developed in this dissertation was used to investigate the impact of drawdown strategy (choke management) on the productivity of wells producing from complex fracture networks. The competing phenomenon of higher initial production rate and faster fracture closure depending on the applied drawdown strategy was observed. Based on NPV maximization, an optimum drawdown strategy can be calculated. The model was also applied to estimate the effective permeability of the SRV (stimulated reservoir volume) to account for complex fractures in upscaled traditional reservoir simulation models.

Tracer transport was implemented in the geomechanical reservoir simulation model to analyze the impact of (a) fracture geometry, (b) fracture propagation and closure effects, and (c) fracture complexity on the tracer response curves. An effective model was created to simulate tracer tests in complex fracture networks. Closure of activated natural fractures can explain the multiple peaks in the tracer response curves observed in the field tests. A neural network-based inverse modeling was performed to estimate effective connected fracture length using peak tracer concentration values, peak times, and tracer recovery from chemical tracer flowback data. Observations from the chemical tracer analysis were combined with radioactive proppant tracer and pressure interference tests to diagnose well interference for the Hydraulic Fracturing Test Site #1.

Table of Contents

List of Tables

List of Figures

Chapter 1: Introduction

1.1 Background And Motivation

Hydraulically fractured horizontal wells have helped in economical oil and gas production from ultra-low permeability reservoirs. Horizontal drilling combined with hydraulic fracturing has contributed to increases in the USA's oil and gas production in the last decade. As a result, hydraulically fractured horizontal wells accounted for most new oil and natural gas wells in the year 2016 as shown in Figure 1.1 (Cook et al., 2018).

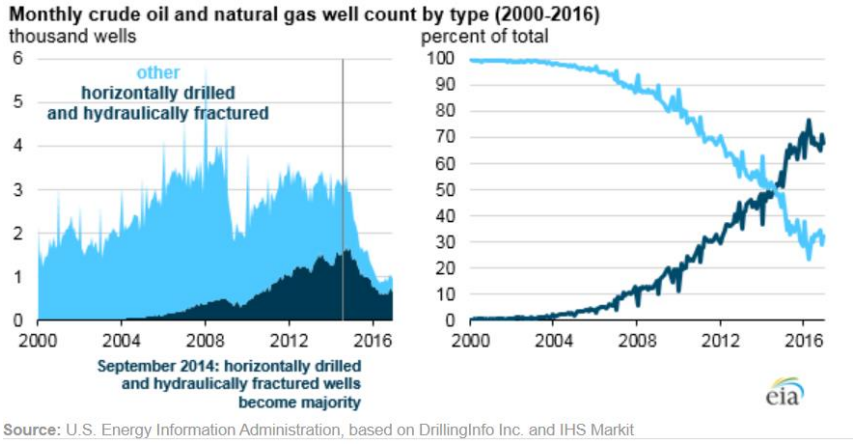

Figure 1.1: Monthly crude oil and natural gas well count by type (from 2000-2016) (Cook et al., 2018)

In a hydraulic fracturing operation, fracturing fluid and proppant are pumped into the reservoir to create cracks to increase the contact area of the reservoir with the wellbore. In the case of horizontal wells, hydraulic fracturing is performed in multiple stages, which helps in creating a large number of fractures. In a field development, multiple horizontal wells with multiple stages are drilled and completed from a single pad location to reduce

the costs and environmental footprints. The productivity of these multi-fractured multi-well pads depends on various fracture properties, reservoir properties, and operating conditions, as shown in Figure 1.2.

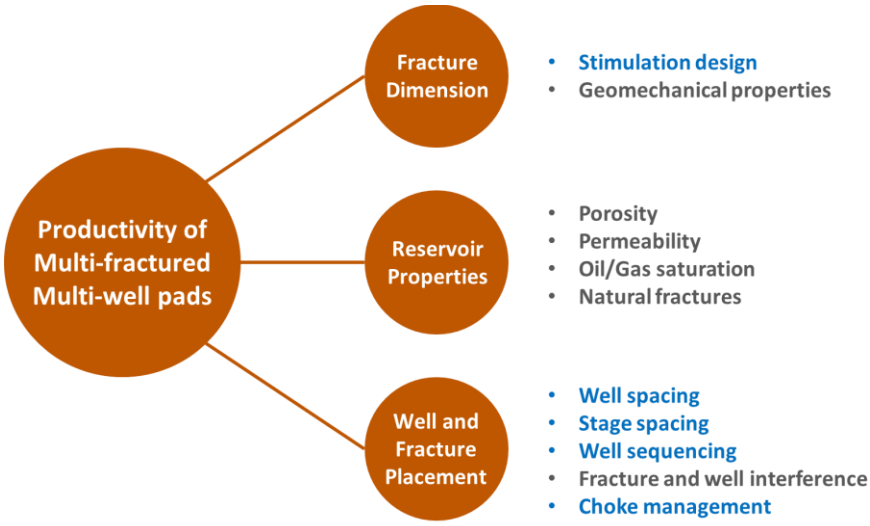

Figure 1.2: Important factors that affect the productivity of multi-fractured multi-well pads. The parameters shown in blue are the parameters over which operators have some degree of control, and those can be optimized for efficient reservoir drainage.

1.1.2 Preliminary Analysis of Pad Drilled Well Productivity

A 3-D, black oil reservoir simulation model was used for the productivity analysis of multifractured horizontal well. A multi-well and multi-fracture model was simplified by simulating only a single fracture to reduce the model complexity and computational time. By assuming uniform fracture growth from all clusters in a stage, a repeating unit was selected with no-flow boundary conditions. Figure 1.3 shows the simulation domain as a dotted area with the no-flow boundary. W and F denote the well spacing and fracture

spacing. Fine-scale gridding was employed near the fracture face along the horizontal wellbore to accurately capture the pressure drop in the regions adjacent to the fractures. The grid size increases away from the fracture face. Sensitivity analysis on flow rate was performed by varying fracture spacing and well spacing.

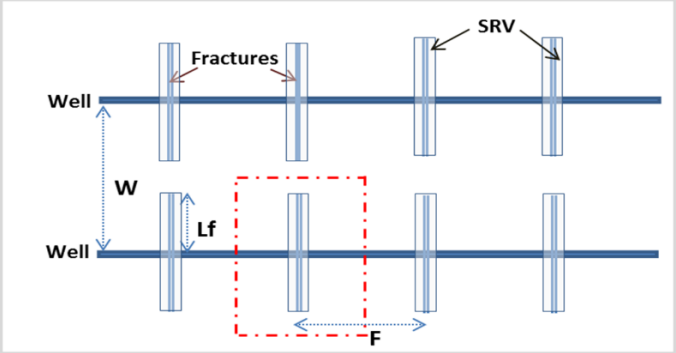

Figure 1.3: A simulation model for pad drilled multifractured well

1.1.2.2 Effect of Fracture Spacing and Well Spacing on rate decline

Early time flow in the reservoir is normal to the fracture face, while flow across the fracture tip is negligible, and there is no interference between the fractures (Wang and Zhang, 2014). The flow rate initially declines with the square root of time as shown by half slope line on rate vs. time log-log plot in Figure 1.4. We observed that rate decline becomes faster at the onset of pressure interference between adjacent fractures and wells.

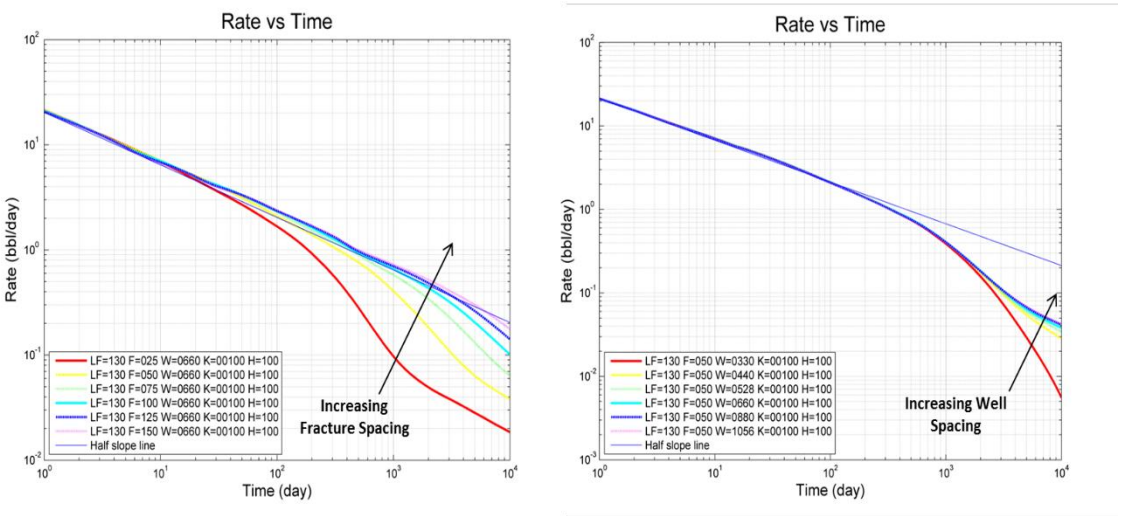

Figure 1.4: Effect of fracture spacing and well spacing on flow rate from a single fracture. (LF is fracture half-length in ft., F is fracture spacing in ft., W is well spacing in ft., K is matrix permeability in nano-Darcy, H is fracture height in ft.)

1.1.2.3 Fracture Spacing and Well Spacing Optimization

The productivity of pad drilled multi-fractured horizontal wells is highly dependent on well spacing and fracture spacing, two factors over which operators have some degree of control. Too small a well spacing (better drainage) would result in high capital costs, and too large a well spacing (low capital cost) results in poor drainage of the reservoir. Well spacing and fracture spacing can be optimized by maximizing the net present value (NPV) for a pad. We developed an integrated fracture modeling and reservoir modeling workflow to estimate the optimum well spacing and fracture spacing as shown in Figure 1.5.

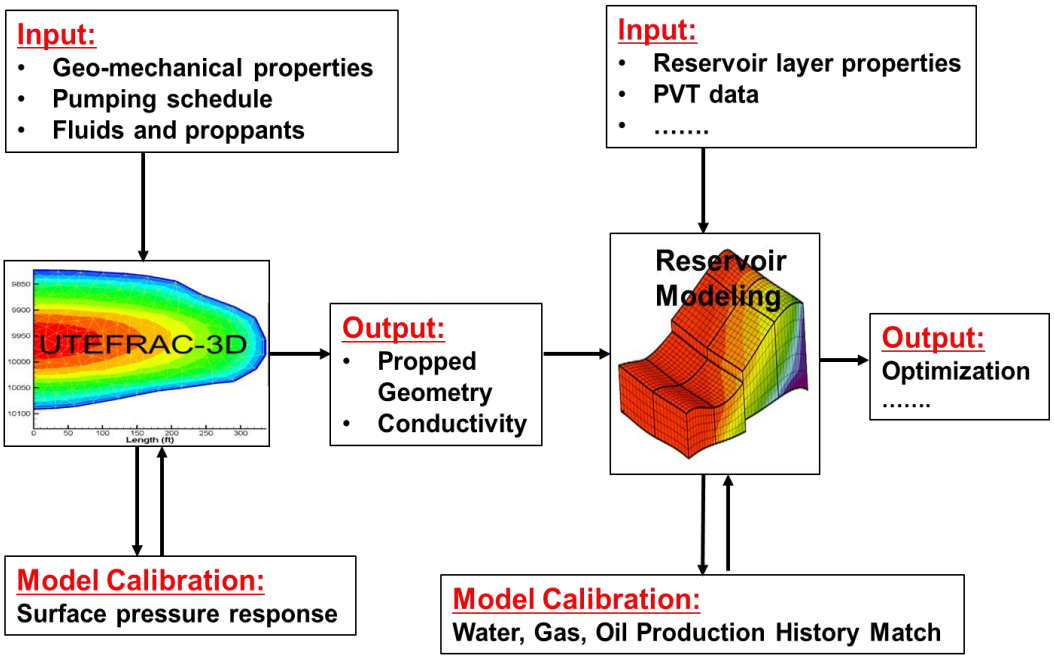

Figure 1.5: Fracture modeling and reservoir modeling combined workflow for well spacing and fracture spacing optimization.

Fracture modeling was performed to obtain the fracture dimensions and fracture conductivity. Production history matching of the oil, gas, and water rates was performed for an existing fracture treatment to estimate the fracture dimensions and the number of fractures per stage. The real costs for drilling and completing the well were used to estimate the upfront capital costs. The completion costs for different fracture lengths and the different fractures per well were extrapolated based on the actual completion costs per unit fracture length. Reservoir simulations were then performed for different well and fracture spacing. The NPV was calculated based on the anticipated cash flow, discount rate, and completion costs. The maximum NPV is then used to select the optimum well spacing and fracture spacing.

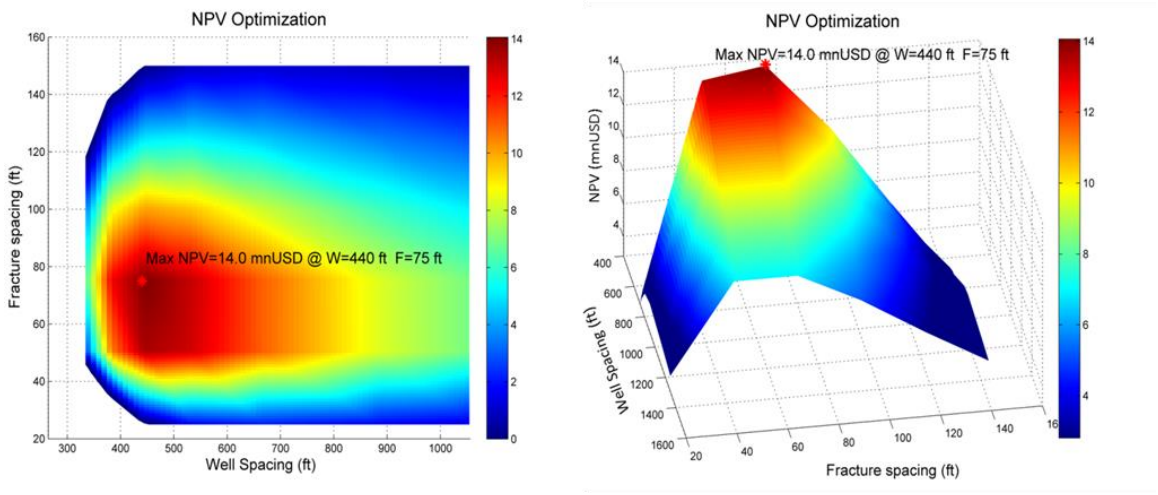

Figure 1.6: NPV vs. fracture spacing and well spacing. (Matrix permeability=100 nD, Fracture half-length=190 ft.)

The impact of reservoir permeability on optimum well and fracture spacing was analyzed. The following conclusions can be drawn:

- The optimum well spacing and fracture spacing increases with an increase in reservoir permeability (Figure 1.7).
- The optimum penetration ratio (2*LF/W) decreases with an increase in reservoir permeability (Figure 1.8).

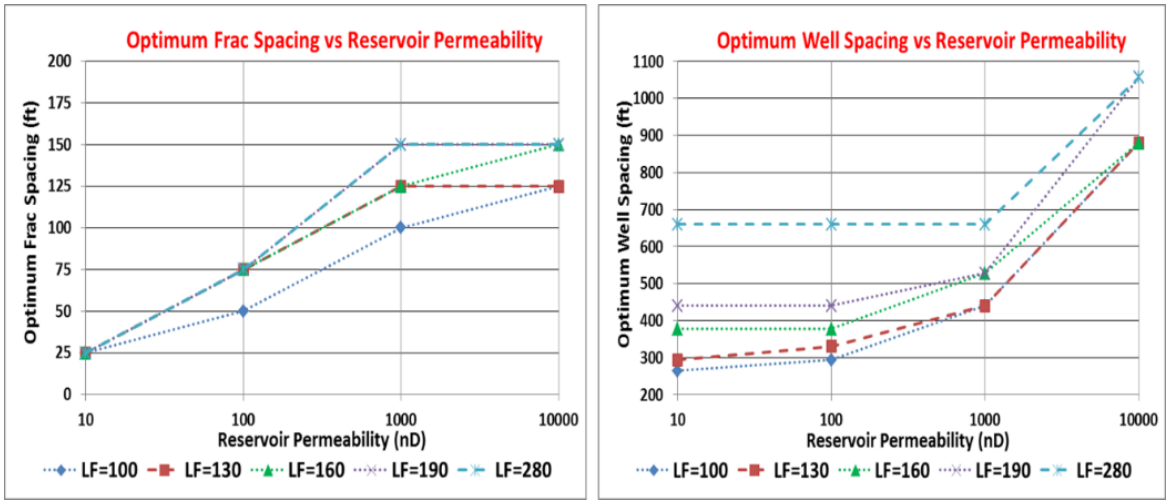

Figure 1.7: Effect of reservoir permeability on optimum fracture spacing and well spacing

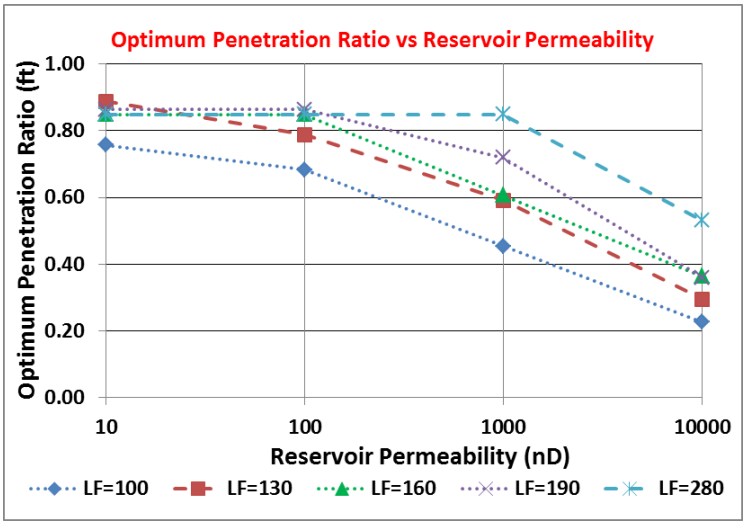

Figure 1.8: Effect of reservoir permeability on optimum penetration ratio

Based on this preliminary analysis, we observed that the Net Present Value (NPV) of a pad is highly sensitive towards fracture length, fracture spacing, and well spacing. This case-study also helped in identifying other important parameters that affect the drainage

around multi-fractured wells and were not included in preliminary simulations. These missing phenomena in the existing workflow are discussed in the next few sections.

1.1.3 Motivations

1.1.3.1 Non-planar complex fracture networks

The evidence of non-planar asymmetric fracture growth during hydraulic fracture propagation was found based on mine-back experiments (Warpinski and Teufel, 1987; Jeffrey et al., 1995). These studies demonstrated that bedding planes, geological discontinuities, and natural fractures might lead to asymmetric fractures and multiple fracture propagation due to fracture branching (Figure 1.9).

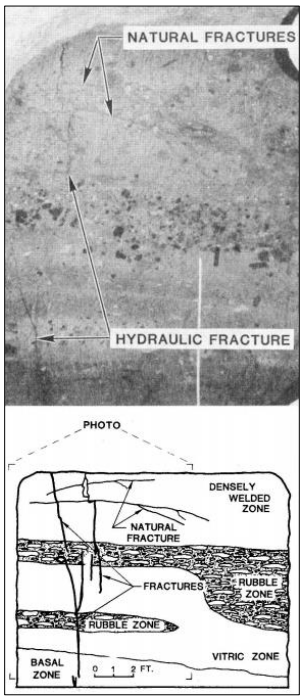

Figure 1.9: Photograph (from mine-back) and sketch of complex fracture creation taken from Warpinski and Teufel (1987).

Complex fracture networks can be created due to the activation of natural fractures by propagating hydraulic fractures. Shear failure of natural fractures can occur due to the stresses generated by propagating hydraulic fracture. Microseismic clouds as observed during hydraulic fracturing, provides the information of these shear failure events and suggests the creation of complex fracture networks (Fisher et al., 2004; Warpinski et al., 2005; Cipolla et al., 2010).

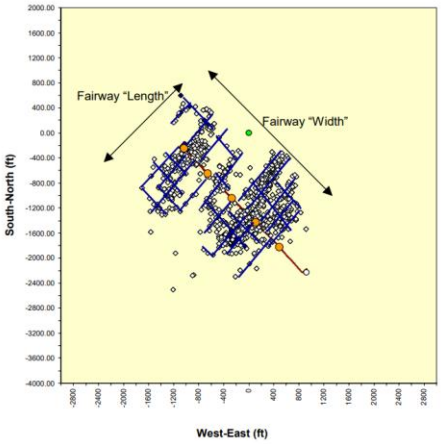

Figure 1.10: Complex fracture illustration based on fracture mapping using microseismic clouds in Barnett. (Fisher et al., 2004)

Several core-through studies (Raterman et al., 2018; Gale et al., 2018) have also provided evidence of complex fracture network formation. These studies analyzed cores that were extracted from a region near a hydraulically fractured well. Hydraulic fracture swarms, as observed in these studies, suggests the creation of complex fracture networks.

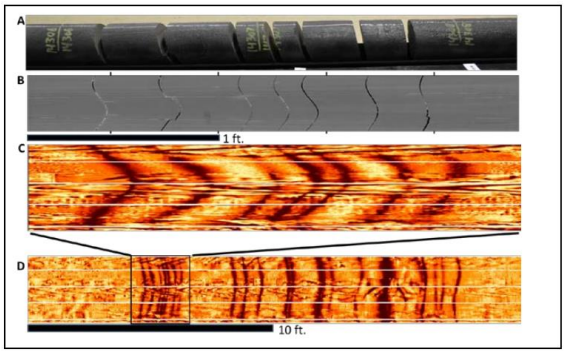

Figure 1.11: Hydraulic fracture swarm consisting of 22 fractures in a 20 ft. section of a well in Eagle Ford (Raterman et al., 2018).

1.1.3.2 Impact of changes in in-situ stress on fracture conductivity

Hydraulic fractures experience a large change in the in-situ stress during production due to the well bottom hole pressure changes. A decrease in the well bottomhole pressure increases the compressive stress acting on the hydraulic fractures. This leads to a reduction in the fracture width and hence fracture conductivity. Several laboratory experiments (Van Dam et al., 2000; Fredd et al., 2000; Wu et al., 2017) and field studies (Okouma Mangha et al., 2011; Sarna et al., 2014) provide the evidence of such fracture closure behavior.

1.1.3.3 Well interference effects

In the existing reservoir simulation studies, a planar bi-wing symmetric fracture geometry is assumed. However, several field studies (Courtier et al., 2016; Walser and Siddiqui, 2016) have demonstrated asymmetric hydraulic fracture propagation towards the depleted region as shown in Figure 1.12.

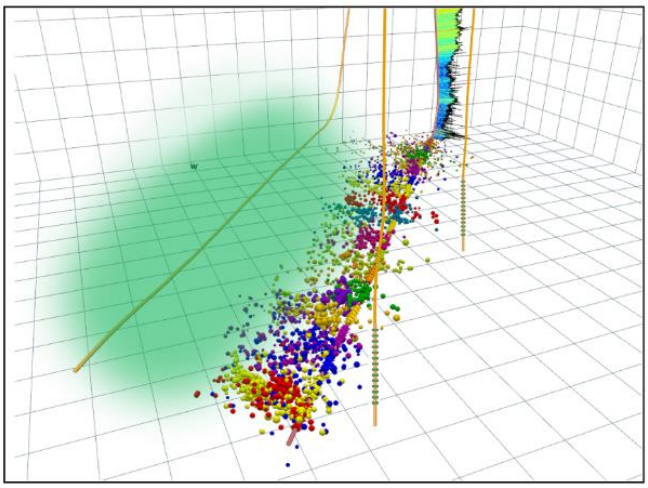

Figure 1.12: Microseismic activity suggesting asymmetric fracture propagation towards a depleted region (Walser and Siddiqui, 2016).

As unconventional basins are getting matured in the USA, a higher number of infill wells are drilled to meet production targets (Miller et al. 2016). Prior depletion in the primary wells leads to a total stress reduction in the reservoir (Roussel et al., 2013; Manchanda et al., 2017). This reduced total stress region around the primary wells leads to an asymmetric fracture propagation from the infill wells (AlTammar et al., 2018; Agrawal and Sharma, 2018).

1.1.3.4 SRV estimation based on geomechanical effects

The stimulated reservoir volume (SRV) concept was introduced by Warpinski et al. (2005) to capture the effect of complex fracture on production in simplified reservoir simulation models. In the existing modeling workflow, SRV parameters (permeability and extent) are used as a calibration factor for history matching and are disassociated from the geomechanical effects and fracture modeling. This type of workflow helps in capturing

early production behavior using simplified simulation models, but this approach can lead to an inaccurate forecast of long term well performance (Cipolla and Wallace, 2014).

1.2 Research Objectives

The main objective of this research is to develop a numerical reservoir simulation model that can be used to analyze the productivity of wells producing from complex fracture networks. An additional objective of this research is to model and analyze chemical tracer tests to understand the important factors affecting well productivity. These objectives can be accomplished through the following tasks:

1. Develop geomechanics coupled reservoir simulation model that can model fluid flow and tracer transport in complex fracture networks.
2. Investigate the impact of fracture closure on well productivity for wells producing from complex fracture networks to optimize drawdown (choke management) strategy.
3. Develop a workflow to estimate the effective permeability of the SRV.
4. Analyze the effect of primary well depletion on infill well fracture growth and overall production from primary and infill wells.
5. Analyze chemical tracer flowback data to understand fracture wellbore connectivity.
6. Investigate well interference for the Hydraulic Fracturing Test Site # 1 by integrating tracer and pressure interference analysis.

1.3 Organization of The Dissertation

This dissertation is divided into eight chapters. Chapter 2 presents the model formulation. Chapters 3, 4, and 5 provide the application of the model related to well

productivity. Chapters 6 and 7 present the model application related to tracer-based fracture diagnostics.

Chapter 2 discusses the mathematical formulation and algorithm for the geomechanical reservoir simulation model for a complex fracture network. An automated meshing algorithm to create the finite-volume mesh for any arbitrarily shaped complex fracture network is described. The model also incorporates a tracer transport model that can simulate tracer injection and flowback coupled with fracture propagation and closure. Finally, model verification cases are presented to verify fluid flow and tracer transport.

Chapter 3 describes the application of the model for analyzing the impact of fracture closure on well productivity. The impact of drawdown management on well productivity is investigated. This chapter discusses the competing phenomena of higher initial production rate and faster fracture closure during production. Optimum drawdown strategy is calculated based on NPV maximization.

Chapter 4 presents a methodology to estimate the effective permeability tensor for the SRV around the hydraulic fracture. The presented workflow includes the coupled effect of fracture modeling and reservoir simulation on SRV parameter estimation. The impact of natural fracture orientation and propagating hydraulic fracture height on the SRV parameters is investigated.

Chapter 5 investigates the primary (parent) and infill (child) well interaction effects on fracture growth and production. Impact of reservoir flow properties and infill timing on the child well fracture growth, and overall production is analyzed. We also investigated the effect of operating conditions on the parent well production due to the parent-child well interference.

Chapter 6 describes the application of the model for chemical tracer flowback analysis. Chemical tracer injection and flowback simulations coupled with fracture modeling, are presented. We also proposed a tracer flowback analysis technique to estimate the fraction of the created fracture area, which is open and connected to the wellbore.

Chapter 7 presents the integrated analysis of chemical fluid tracer, radioactive proppant tracer, and pressure interference test for an 11 well pad in the Permian Basin for the Hydraulic Fracturing Test Site # 1. We analyzed the impact of well stimulation sequence on the onset and duration of interference and explained the difference between early time and late time well interference.

Chapter 8 summarizes the important conclusions of this dissertation and provides recommendations for future work.

Chapter 2: Model Development for Flow Simulation in Complex Fracture Networks

2.1 INTRODUCTION

Hydraulic fracturing is the most effective method for stimulating hydrocarbon production from low and ultra-low permeability reservoirs. The properties of the created hydraulic fracture such as fracture length/height, conductivity, connectivity to the wellbore, and applied drawdown pressure determine the productivity of hydraulically fractured wells. Numerical simulation models are frequently utilized to understand the impact of the fracture properties and operating conditions on the hydrocarbon production from a hydraulically fractured well. Usually, in these simulation models, a planar bi-wing fracture which is open and connected to the wellbore is used for productivity analysis. However, recent fracture diagnostics field studies (Fisher et al., 2002; Raterman et al., 2017; Gale et al., 2018) and several fracture modeling studies (Weng et al., 2011; Wu and Olson, 2014; Shrivastava and Sharma, 2018) indicate that a hydraulic fracturing stimulation can lead to the formation of complex fracture networks. The conductivity and connectivity of these complex fracture networks from the wellbore are highly dependent on the changes in the in-situ stresses due to depletion. Hence it is important to capture this fracture closure behavior along with complex fracture geometry in the reservoir simulation studies while analyzing well productivity.

Some of the ideas presented in this chapter were first presented in SPE-194119 (Kumar, A., Seth, P., Shrivastava, K. and Sharma, M.M., 2018. "Optimizing drawdown strategies in wells producing from complex fracture networks." In SPE International Hydraulic Fracturing Technology Conference and Exhibition. Society of Petroleum Engineers). In this paper, Kumar developed the model equations, methodology, and implemented the code.

We have extended a finite volume method based coupled geomechanical reservoir simulation model (Manchanda, 2015; Bhardwaj et al., 2016; Zheng et al., 2019) to simulate flow in complex fracture networks. The extended model can include the impact of depletion on fracture conductivity and connectivity to the wellbore. We also implemented chemical tracer transport in the model for analyzing the fracture connectivity to the wellbore during flowback or production. The objective of this chapter is to explain the modeling workflow, governing equations, and algorithm for simulating fluid flow and tracer transport in complex fracture networks. An adaptive time-stepping algorithm is also presented which helps in running the simulation at a higher time step size without compromising on accuracy.

2.2 MODEL DESCRIPTION

Traditionally dual-porosity models were used to simulate flow through fractured reservoirs. However, the dual porosity modeling approach has several limitations related to modeling fracture closure, large scale fractures, matrix-fracture transfer function calculations, and modeling disconnected fractures. To overcome these limitations, discrete fracture network models were developed to represent fractures individually (Karimi-Fard et al., 2004; Monteagudo and Firoozabadi, 2004). Xu et al., (2016) proposed an embedded discrete-fracture model to simulate flow in fracture networks by specifying non-neighboring connections between matrix and fractures.

In the existing models, fractures are represented as static high-permeability grid-blocks, with no dependence of stresses on fracture width. The results of this approach can be very grid-size dependent. To explicitly include stress dependent fracture closure, we have developed a discrete fracture modeling approach to represent fractures as

discontinuities in the reservoir. Modeling fractures as an explicit discontinuity is essential to capture the stress variations in the vicinity of the fractures due to reservoir depletion and fracture opening/closure. The advantages of modeling fractures as an explicit discontinuity over static high-permeability grid-blocks are summarized in Table 2.1.

Table 2.1: Advantages of modeling fractures as an explicit discontinuity.

Fractures as explicit discontinuity	**Fractures as static high permeability gridblock**
Essential to capture the stress variations near the fractures due to reservoir depletion and fracture opening/closure.	Not possible to capture stress variations around the fracture caused by fracture opening and closing.
Change in fracture pressure due to the change in fracture volume (strain) is captured accurately.	Fracture pressure does not depend on the change in fracture volume.
Flow in the fracture domain is highly dependent on the fracture width (cubic dependence). Fracture conductivity is coupled with the reservoir flow and geomechanics.	Conductivity changes in high permeability fracture gridblocks are artificially stress-dependent. There is no direct geomechanical coupling.

The complex fracture network geometry can be obtained from a simulation of hydraulic fracture propagation in the presence of natural fractures. We have used a displacement discontinuity method (DDM) based hydraulic fracture simulator Multi-Frac-NF (Shrivastava and Sharma, 2018) to model fracture growth in naturally fractured reservoirs. An example of a complex fracture network generated from Multi-Frac-NF simulation is shown in Figure 2.1. The generated complex fracture geometry can be used as an input for our finite volume method (FVM) based coupled geomechanical reservoir

simulator. An open-source finite volume discretization framework, OpenFOAM (Open Field Operation And Manipulation) is used to develop our geomechanics library, FROGG (FRamework for Operations in General Geomechanics) (Cardiff et al., 2015).

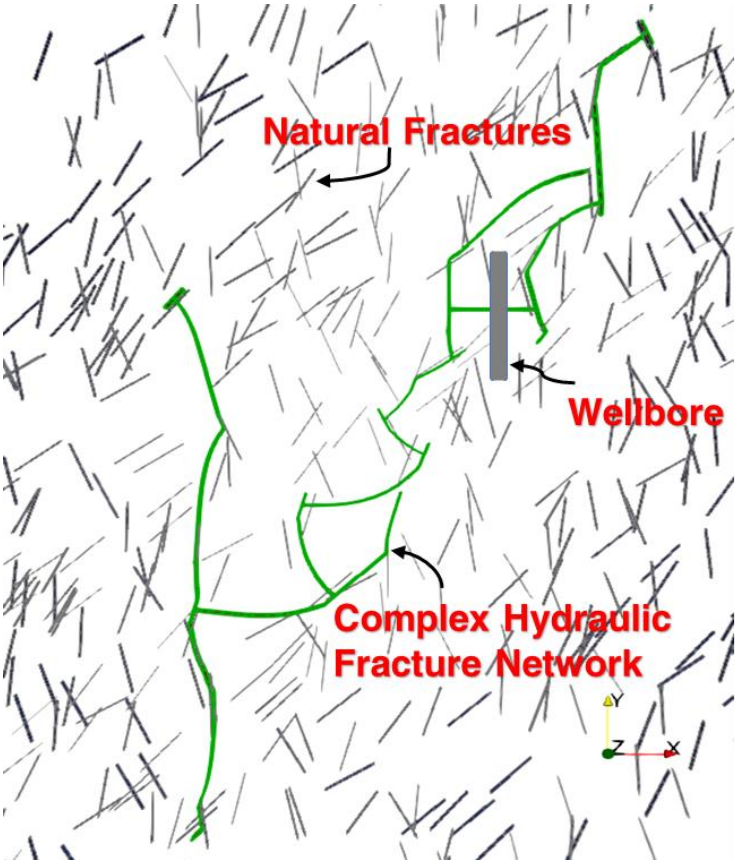

Figure 2.1: Complex fracture network generated due to hydraulic fracture propagation in a naturally fractured reservoir (result from a Multi-Frac-NF simulation).

2.2.1 Automated mesh generation for a given complex fracture network

Generating a high-quality mesh is an essential preprocessing step for any complex geometry simulation. In this section, we present a methodology to generate the

unstructured finite volume mesh for the fracture and reservoir domain for any given complex fracture network.

In Multi-Frac-NF, hydraulic fractures are represented as surface elements. However, in the OpenFOAM solver, a volume mesh is required for flow simulation. We developed an algorithm to convert Multi-Frac-NF surface elements mesh into a volume mesh which is compatible for OpenFOAM simulation. In the next two sections, Multi-Frac-NF and OpenFOAM mesh format are presented.

2.2.1.1 Multi-Frac-NF mesh format

Multi-Frac-NF uses the finite difference method for fluid flow simulation in the hydraulic fracture network. Fluid flow mesh is composed of several surface elements. For a planar fracture, each element in the mesh can have a maximum of four neighbors. When a propagating fracture intersects a natural fracture, a new surface mesh is created and is connected to the propagating fracture mesh (Shrivastava, 2019). In this case, the intersecting fracture surface element has two additional neighbors to account for the fluid exchange between different surface meshes of hydraulic fracture and natural fracture. An example of such complex fracture surface mesh from Multi-Frac-NF is shown in Figure 2.2. The mesh information for this kind of surface mesh can be stored in a text file specifying the following properties for each surface element:

- Coordinate of the center of the surface element
- Dimension in the horizontal and vertical direction
- Orientation
- Neighbor information (element IDs of neighbors and additional neighbors)

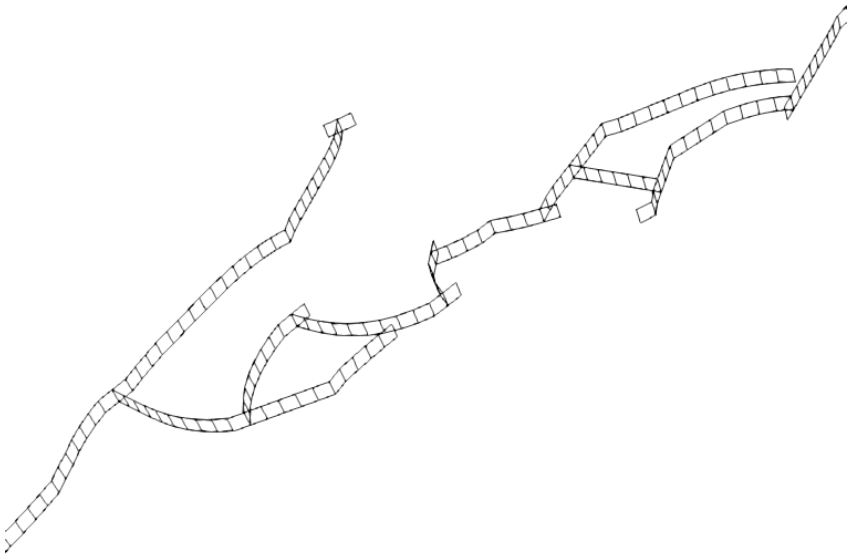

Figure 2.2: An example of a complex fracture surface mesh where multiple meshes are connected.

2.2.1.2 OpenFOAM mesh format

In OpenFOAM, a mesh is composed of 3-D arbitrary polyhedral cells bounded by arbitrary polygon faces. This general structure volume mesh in OpenFOAM is known as PolyMesh. OpenFOAM C++ classes handle a mesh by specifying the mesh properties in following five files in the PolyMesh directory:

1. Points
2. Faces
3. Owner
4. Neighbour
5. Boundary

The points file contains the list of vectors describing the coordinates of cell vertices. Cell vertices are indexed in the sequence as they appear in the list. Faces file contains the

list of faces. A face is defined as an ordered list of points indices from the points file. The ordering of point indices in a face follows the traversed path around the circumference of the face. The face normal vector is defined by the right-hand rule as shown in Figure 2.3.

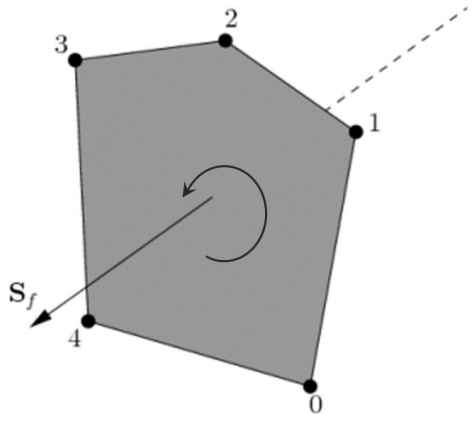

Figure 2.3: Face definition in OpenFOAM as a list of point indices. The face area normal vector (S_f) follows the right-hand rule (Open CFD, 2013).

Faces are divided into two types internal faces and boundary faces. Internal faces are those faces which connect two cells, and boundary faces belong to only one cell as they correspond to the boundary of the simulation domain. Connectivity of cells across a face is defined by describing an owner and a neighbor cell. For an internal face, the owner cell is the cell with the lowest index, and the neighbor cell index is higher than the owner cell. In the case of boundary faces, the connected cell is the owner cell, and the neighbor is not defined. The owner file contains a list of owner cell indices for each face. The neighbour file contains a list of neighbor cell indices of each internal face. The boundary file contains the list of boundary patches for the simulation domain. Hydraulic fracture discontinuity is also defined as a boundary patch in our geomechanical reservoir simulator.

2.2.1.3 OpenFOAM fracture mesh generation from Multi-Frac-NF simulation

We have developed a script in MATLAB to create a finite volume mesh for the complex fracture network generated in Multi-Frac-NF.

Each surface element in Multi-Frac-NF is converted to a hexahedral volume cell (Figure 2.4). A hexahedral volume cell has eight points, and these points are assigned a local point index, as shown by the numbers in Figure 2.4. These points can also lie on other adjacent volume cells, so a global point list is created in our MATLAB code. We loop over all surface elements and check whether a new point needs to be added or that point already exists in the previous cells. Once a new point is added, a global point index is assigned to that point. If that point already exists in the previous cells, then that point is not added to the global list, and the existing global point is mapped to the local point index of the current cell. Similarly, local to global point mapping is done for internal and boundary faces. While writing the OpenFOAM mesh files, global point indices are used to define the point, face, and cell lists.

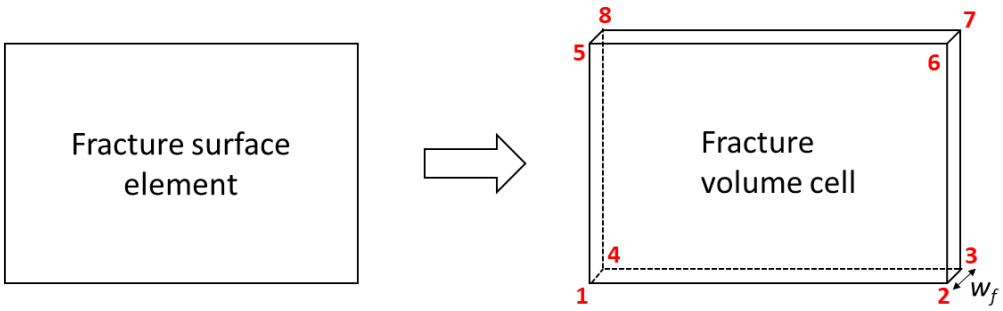

Figure 2.4: Fracture surface elements from Multi-Frac-NF are converted to volume cells by extruding the surface in the fracture width direction. Red-colored numbers denote the local point index.

In a planar fracture, each surface element can have a maximum of four neighbors (two in the height direction and two in the length direction). In the case of fracture branching due to natural fracture intersection, two additional neighbor elements are added in Multi-Frac-NF. However, in an OpenFOAM finite volume mesh, fluid flow between two cells can happen through faces only. Therefore, additional junction cells are added while creating the OpenFOAM finite volume mesh to account for fracture branching (Figure 2.5).

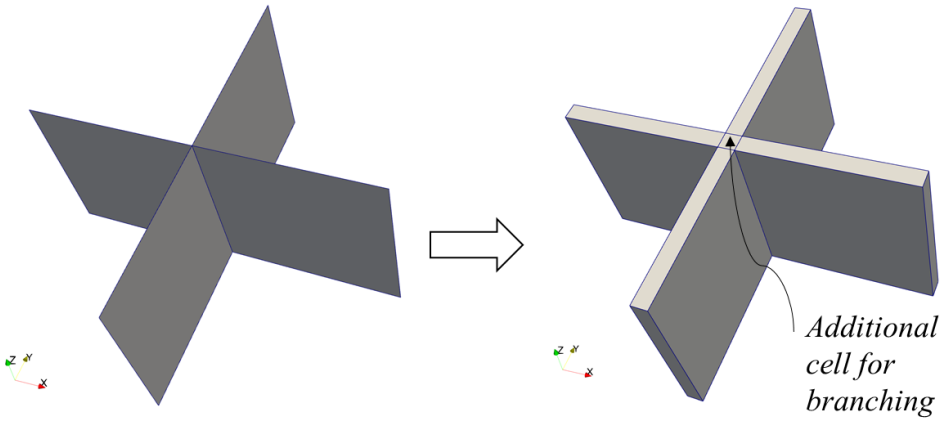

Figure 2.5: Additional volume cells are added in the OpenFOAM mesh to account for branching

After assembling all global points for all cells, the number of internal and boundary faces are identified using neighbor information from Multi-Frac-NF. The owner and neighbor cell for internal faces are identified based on the connected cell indices. Boundary faces are grouped into the boundary patches and are defined as either fracture faces or fracture tips. The developed MATLAB script writes all the necessary mesh files (points, faces, owner, neighbor, and boundary), satisfying the OpenFOAM finite volume mesh criteria. An example of such a fracture network volume mesh is shown in Figure 2.6. This

finite volume mesh is used for solving the fluid flow equation in the fracture domain. Fracture faces boundary patch is used to calculate the flux (leak-off or injection into the reservoir) across the reservoir and fracture. A reservoir mesh conforming to the fracture network is required to calculate the flux and the force balance on the fracture faces.

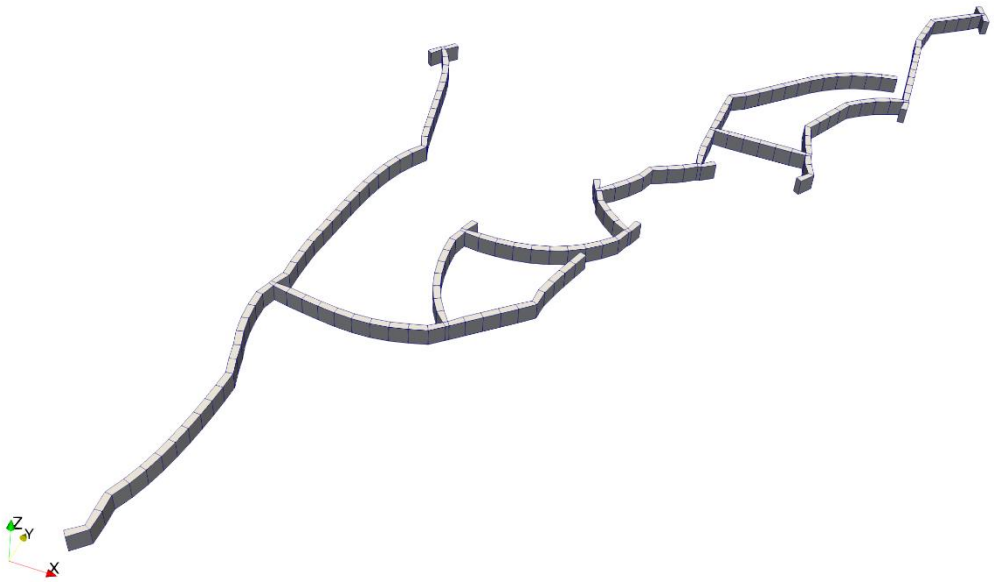

Figure 2.6: Finite volume mesh for a given complex fracture network. Mesh is magnified in the width direction for better visualization.

2.2.1.4 OpenFOAM reservoir mesh generation from Multi-Frac-NF simulation

We have used an open-source platform SALOME for creating a reservoir mesh which is conforming to the complex fracture network geometry. SALOME supports CAD (computer-aided design) modeling which is very useful for complex shapes. All geometry and meshing functionalities in SALOME can be accessed through the integrated programming console in Python. We have developed a script in Python to automatically

generate the reservoir mesh for any given complex fracture network geometry. The developed script has three modules geometry, meshing, and converting the mesh to OpenFOAM format. Our meshing script has the following three options for the input fracture geometry:

1. Multi-Frac-NF simulation
2. Populate natural fractures stochastically for a given natural fracture length and orientation distribution
3. Outline of the shape from standard CAD files or an image

A cuboid is created for the reservoir domain based on the given reservoir dimensions. The reservoir domain is cut using the fracture network geometry to create the discontinuity to define the fracture faces.

SALOME has a set of meshing algorithms, which can be used for meshing geometrical object entities (1D, 2D, 3D sub-shapes). The meshing process is started by creating a sub-mesh for the fracture network. We use a wire discretization algorithm to split the fracture edges into a number of mesh segments using a 1D hypothesis based on the specified input grid size for the fracture domain. Fracture faces are meshed using the NETGEN 2D algorithm which splits faces into either triangular (Delaunay triangulation) or quadrangular mesh elements. Reservoir 3D mesh is created using the fracture sub-mesh based on the NETGEN 3D algorithm. Reservoir mesh may contain hexahedral, prisms, or tetrahedral type of cells. An example of a created reservoir mesh is shown in Figure 2.7. Our meshing script converts the SALOME mesh to the OpenFOAM mesh format by writing the points, faces, owner, neighbour, and boundary files.

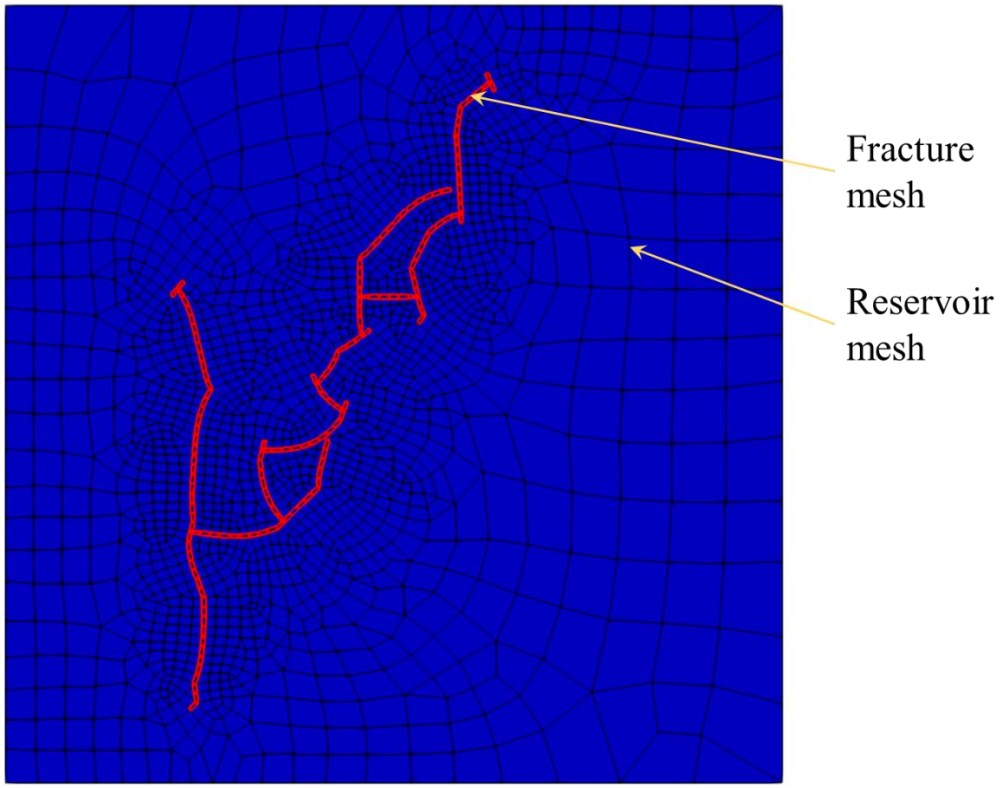

Figure 2.7: An example of reservoir mesh conforming to the given fracture network (top view). Red-colored mesh corresponds to the fracture mesh. (Fracture mesh is magnified in the width direction for better visualization.)

2.2.2 Fracture domain flow simulation using finite volume

The generated fracture mesh and reservoir mesh is used for solving the geomechanics coupled fluid flow in both fracture and reservoir domains. Fracture mesh is created such that each fracture cell contains crack faces (discontinuities corresponding to the fracture) from the reservoir mesh. Figure 2.8 illustrates the relative arrangement of fracture and reservoir mesh by showing the zoomed-in view of both the meshes. Based on these schematics, the fluid flow and geomechanical coupling between the reservoir and

fracture domain are explained in Figure 2.9. All possible flow combinations (reservoir cell to reservoir cell, reservoir cell to fracture cell, and fracture cell to fracture cell) have been accounted for. Fracture pressure is applied as traction on the crack faces while solving for geomechanical equilibrium.

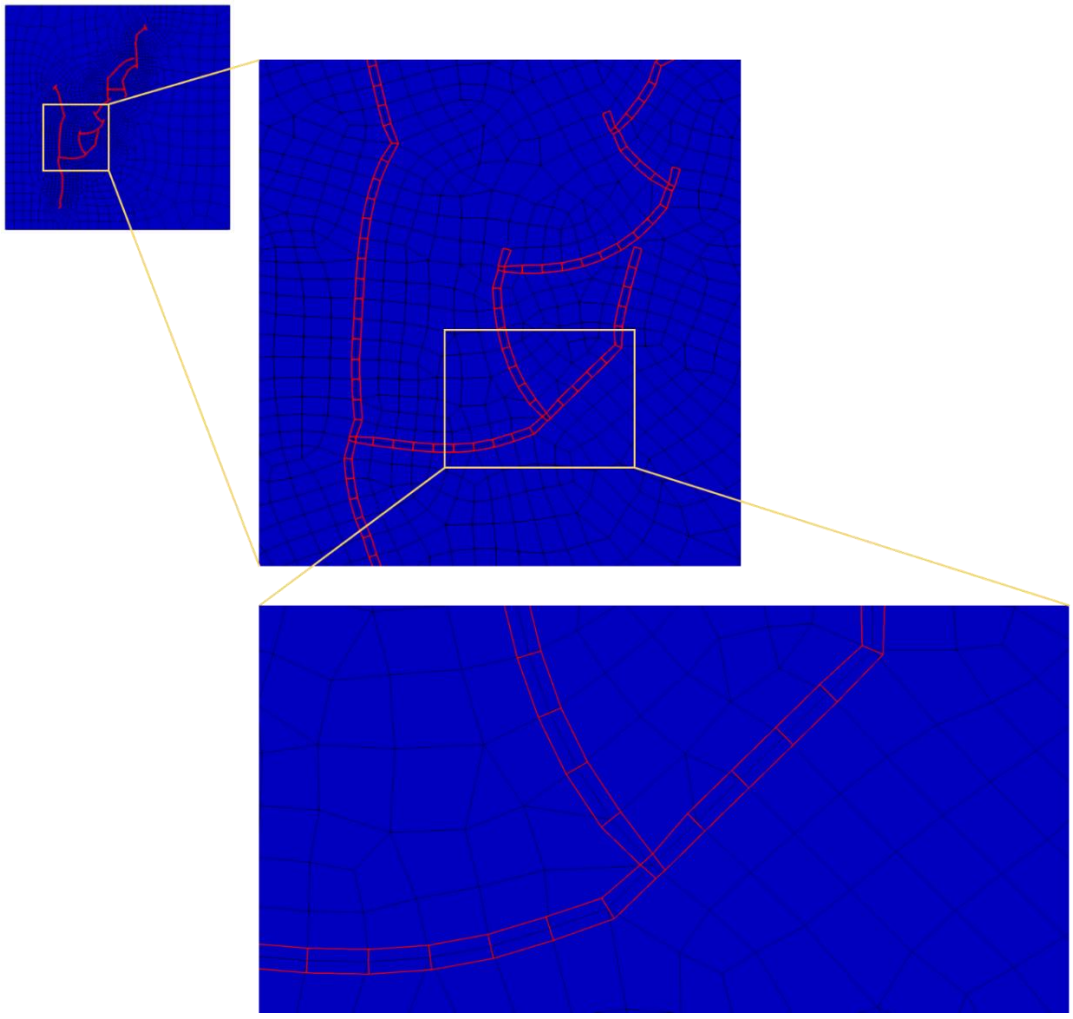

Figure 2.8: Relative arrangement of fracture and reservoir cells (top view). Each fracture cell contains a face from the reservoir mesh, as shown in the zoomed-in sub-figures. (Fracture mesh is magnified in the width direction for better visualization.)

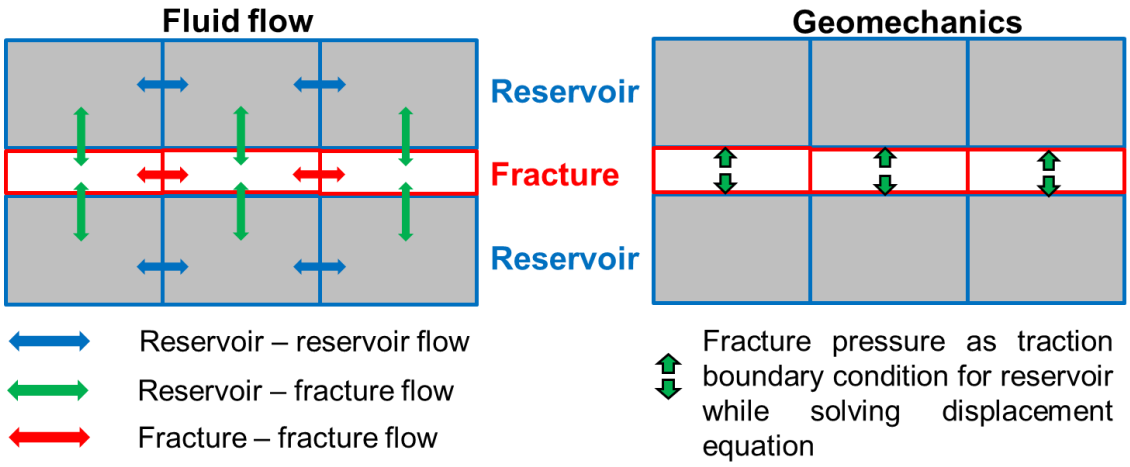

Figure 2.9: Fluid flow and geomechanics coupling between reservoir and fracture domains.

Equation (2.1) represents the fluid flow in the reservoir (matrix) domain. This equation was derived using the conservation of mass and Darcy's law.

$$\phi_m c_t \frac{\partial p^m}{\partial t} - \nabla.\left(\overline{\overline{k_m}}\,\lambda_j \nabla p^m\right) - \alpha \nabla.\left(\frac{\partial U}{\partial t}\right) = q_{fracture-matrix} \qquad (2.1)$$

where ϕ_m is the reservoir porosity, c_t is the total compressibility, p^m is the fluid pressure in the reservoir, $\overline{\overline{k_m}}$ is the reservoir permeability tensor, λ_j is the relative fluid mobility (relative permeability/viscosity) for phase j, α is the Biot's coefficient, U is the geomechanical displacement vector field, and $q_{fracture-matrix}$ is the leak-off/injection from fracture to matrix (reservoir) domain.

The first term on the left-hand side in equation (2.1) is the accumulation term. The second term on the left-hand side corresponds to the flux between reservoir cells. The third term on the left-hand side includes the poroelastic coupling term which relates the change in the pore volume due to geomechanical displacement.

Equation (2.2) describes the fluid flow inside the fracture domain. Fluid flow in the fracture domain is modeled as the flow between parallel plates. This equation is derived from the Reynolds lubrication equation which accounts for the mass conservation and momentum conservation.

$$c_f \frac{\partial p^f}{\partial t} + \frac{1}{w_f}\frac{\partial w_f}{\partial t} - \nabla.\left(\frac{w_f^2}{12\,\mu}\nabla p^f\right) = q_{well} + q_{matrix-fracture} \qquad (2.2)$$

where c_f is the fluid compressibility, p^f is the pressure in the fracture domain, w_f is the fracture width, μ is the relative fluid viscosity, q_{well} is the source/sink term corresponding to injection or production from a well, and $q_{matrix-fracture}$ is the leak-off/injection from the matrix (reservoir) to the fracture domain.

The second term on the left-hand side in equation (2.2) corresponds to pressure change in the fracture domain due to the change in fracture volume. The third term on the left-hand side corresponds to the flux between fracture cells.

These flow equations ((2.1) and (2.2)) have an equal and opposite matrix-fracture flow term which is calculated using equation (2.3).

$$q_{f-m} = T_{f-m}\,\lambda_j(p^f - p^m) \qquad (2.3)$$

where T_{f-m} is the transmissibility factor between the fracture-matrix segment (Hajibeygi et al., 2011; Xu et al., 2016). T_{f-m} depends on the fracture orientation and matrix permeability. T_{f-m} is calculated as per the following equation.

$$T_{f-m} = \frac{2 * A_f\left[\left(\bar{\bar{K}}.\vec{n}\right).\vec{n}\right]}{d_{f-m}} \qquad (2.4)$$

where A_f is the area of the fracture segment in the matrix cell, $\vec{n}$ is the normal vector to the fracture plane, and d_{f-m} is the average normal distance from fracture to the matrix. d_{f-m} is calculated using the following equation.

$$d_{f-m} = \frac{\int_V x_n dV}{V} \tag{2.5}$$

where x_n is the normal distance from the fracture to the matrix element, and V is the matrix cell volume. The d_{f-m} calculation requires numerical integration for a general matrix-fracture arrangement; however, in a fully conforming matrix-fracture mesh, analytical expressions exist and are given in Hajibeygi et al. (2011).

For geomechanical modeling, the displacement equation (2.6) was formulated in Bryant et al., (2015) using the condition of mechanical equilibrium and the linear elastic constitutive relations for the stress tensor and strain. Fracture pressure is applied as a traction boundary condition while solving the displacement equation.

$$\rho_r \frac{\partial^2 U}{\partial t^2} = (2\mu + \lambda)\nabla^2 U + \nabla.[\mu U^T + \lambda * tr(\nabla U)I - (\mu + \lambda)\nabla U + \sigma_0] - \alpha \nabla p^m \tag{2.6}$$

where ρ_r is the reservoir rock bulk density, λ and μ are the Lame's parameter.

The equations mentioned above (fluid flow in matrix and fracture domain and displacement equation) are solved in an iterative algorithm which is described in Figure 2.10. The displacement equation is coupled with a fracture closure model which will be described in the next section.

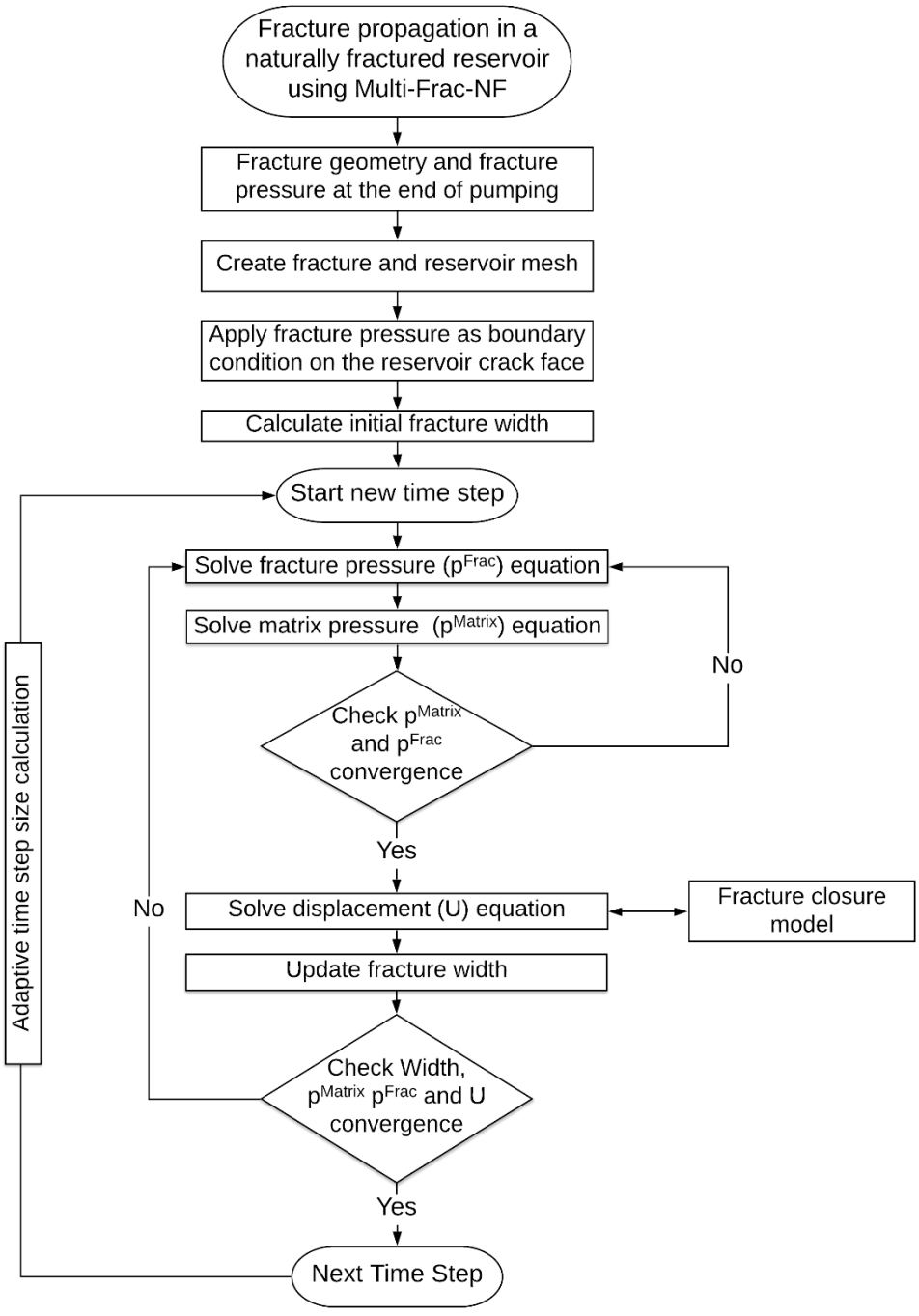

No table of figures entries found.

Figure 2.10: Block diagram showing the algorithm for coupled geomechanical reservoir simulation model for complex fracture networks.

2.2.3 Fracture closure modeling

During the hydraulic fracturing stimulation, high pressure in the fracture helps in keeping the fracture open against the in-situ stresses. However, pressure in the fracture drops below the in-situ stresses during shut-in (due to leak-off) or production (due to the applied lower well bottom-hole pressure). As the net pressure (difference of fracture pressure and in-situ stress) decreases, fracture faces move towards each other. If the fracture surface is perfectly smooth, then at zero net pressure entire fracture surface will come in contact. However, in reality, the created fracture surface is not perfectly smooth. Brittle fracture properties, heterogeneity, and microstructures can affect the damage process of the rock and can induce rough crack faces (Morel et al., 2000).

During production, the net pressure inside the fracture becomes negative. This negative net pressure results in a negative fracture width calculation based on the geomechanical displacement equation. However, in reality, the created fractures never attain a zero/negative width. They maintain a positive width due to surface roughness/asperities and proppants injected during hydraulic fracturing (Fredd et al., 2000). As shown in Figure 2.11, non-matching asperities and proppant help in maintaining a positive average fracture width. To model this type of fracture closure behavior, an additional contact stress is applied on the fracture surface to capture the effect of asperities (Wang et al., 2017). We use the Barton-Bandis normal contact stiffness relationship (Bandis et al., 1983) to model fracture closure.

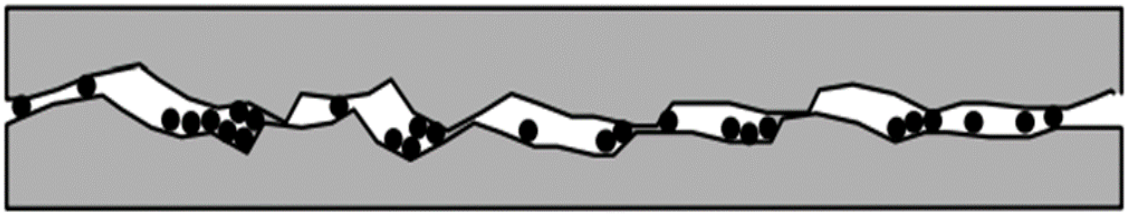

Figure 2.11: Displaced fracture faces with proppant and asperities. (Fredd et al., 2000)

Bandis et al., (1983) derived a relationship between the normal contact stress acting on a closing fracture surface and the amount of closure by conducting several experiments of rock joints deformation under normal loading. The magnitude of fracture closure can be related to offset width, stiffness, and fracture width. Seth et al., (2018) simplified the contact relationship from Bandis et al., (1983) which is shown in equation (2.7).

$$\sigma_n = \frac{\left(w_{offset} - w\right)}{a - b\left(w_{offset} - w\right)} \tag{2.7}$$

where σ_n is the normal contact stress acting on the fracture surface, w is the current width of the closing fracture, w_{offset} is the fracture width at which asperities in the closing fracture come in contact, a and b are the coefficients which depend on the initial normal stiffness and offset width as follows:

$$a = \frac{1}{K_{ni}} \qquad\qquad b = \frac{1}{K_{ni} w_{offset}} \tag{2.8}$$

where K_{ni} is the initial normal stiffness which is computed using the joint roughness coefficient, joint compressive strength, and joint aperture. In the fracture closure model, as described in Seth et al., (2018), equation (2.7) is used as the non-linear relationship between

normal contact stress acting on the fracture surface and the closing fracture width. It can be clearly observed that contact stress is zero when the closing fracture width is equal to the offset width, and the contact stress increases to a very high value when closing fracture width reduces to a very small value. When fracture width is more than the width offset, fracture asperities are not in contact, and contact stress is not defined. Contact stress, in addition to the fracture pressure, helps in keeping the fracture open when fracture width becomes less than the offset width due to the negative net pressure in the fracture.

Additionally, to include the effect of proppant on fracture closure, a modified normal contact stiffness relationship (Wang and Sharma, 2018) for propped fractures is implemented in our model. Equation (2.9) represents the relationship between contact stress due to the proppant pack. $\sigma_{ref,p}$ represents the effective normal stress at which fracture aperture is reduced by 90%. $w_{0,p}$ is the propped fracture width when contact stress is zero and can be calculated based on the proppant concentration.

$$\sigma_n = \frac{\sigma_{ref,p}}{9}\left(\frac{w_{0,p}}{w_f} - 1\right) \qquad \text{for } w_f \leq w_{0,p} \tag{2.9}$$

In addition to the propped fractures, the hydraulic fracturing process also creates a large number of fractures that are too small to accommodate conventional sized proppants. These fractures can be referred to as induced-unpropped (IU) fractures (Sharma and Manchanda, 2015). Evidence of the existence of these IU fractures is observed in microseismic data, flowback analysis, and tracer data. The closure behavior of these IU fractures is different from the propped fractures. These IU fractures can have a significant contribution to hydrocarbon production if the conductivity of these IU fractures is maintained. It is, therefore, important to capture the closure behavior of the IU fractures in

the production simulations. Wu et al. (2017) conducted experiments to analyze the impact of stress on fracture conductivity of IU fractures for rocks with different mineralogy. Figure 2.12 (taken from Wu et al., 2017) shows the unpropped fracture conductivity vs. closure stress for rocks with different clay content. The conductivity vs. stress curves can be fitted to the following empirical exponential relationship.

$$\frac{k}{k_0} = e^{-\gamma(\Delta\sigma_n)} \tag{2.10}$$

where k_0 is the reference fracture permeability, $\Delta\sigma_n$ is the change in closure stress, and γ is the permeability modulus. In experiments conducted by Wu et al., (2017), we observed that γ ranges from 1x10^{-7} to 3.2x10^{-7} Pa^{-1} depending on rock mineralogy (Figure 2.12). We also observe that the unpropped fracture conductivity is higher for rocks that have less clay. We use the permeability modulus (γ) as a proxy for clay content to account for the effect of mineralogy while modeling unpropped fracture closure.

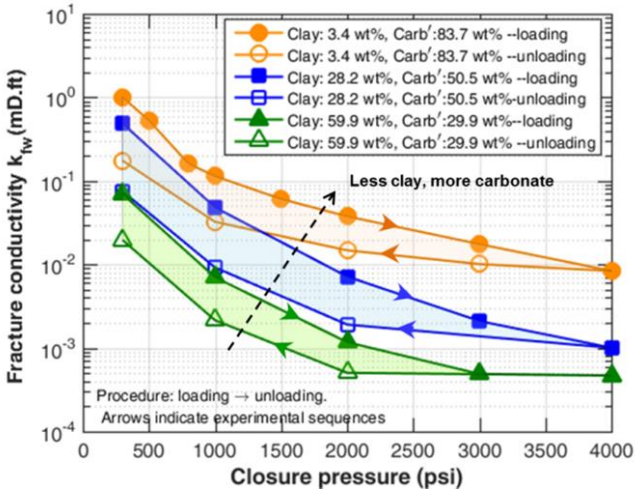

Figure 2.12: Unpropped fracture conductivity vs. closure stress for different mineralogy (Wu et al., 2017).

2.2.4 Tracer transport modeling using finite area/finite volume

Chemical tracer tests have been utilized to understand fracture and reservoir inflow characteristics (Asadi et al., 2002; Du and Guan, 2005; Mulkern et al., 2010; Spencer et al., 2013). During the fracturing operation, water or oil-soluble chemical tracers are injected into the formation along with the fracturing fluids. Each hydraulic fracturing stage can be tagged with a different tracer. These tracers can be recovered from the fractured well and another monitor well during flowback. Insight about the fracture connectivity and flow pattern of the reservoir can be obtained from the tracer response curves.

Existing tracer flowback analysis methods have used static fractures and ignored fracture closure during flowback. A static fracture assumption will lead to an erroneous tracer concentration in the fracture and reservoir because it cannot capture the tracer leak-off during fracture propagation correctly. Models that assume no fracture closure cannot capture the tracer retention in the reservoir and fractures resulting in very low tracer recovery as observed in several field studies (Spencer et al., 2013). To overcome these limitations, we have implemented the tracer transport model in the OpenFOAM geomechanical reservoir simulator developed by Zheng et al., (2019).

2.2.4.1 Mathematical Formulation

In the case of tracer transport modeling, two fundamental assumptions are used, tracers do not occupy any volume, and they do not affect the physical properties of the phases (Agca et al., 1990). The continuity equation for a tracer component *k* in terms of volume of component *k* per unit pore volume (Lake, 1996) is shown in equation (2.11).

$$\frac{\partial}{\partial t}\left(\varphi \sum_{l=1}^{n_p} \rho_k S_l C_{kl}\right) + \vec{\nabla}.\left[\sum_{l=1}^{n_p} \rho_k C_{kl} \vec{u}_l\right] - \vec{\nabla}.\left[\sum_{l=1}^{n_p} \rho_k \varphi S_l D_{kl}.\vec{\nabla} C_{kl}\right] = R_k \qquad (2.11)$$

where l denotes a phase (water, oil or gas), n_p is the total number of phases, ρ_k is the density of pure component k. D_{kl} is the dispersion tensor including molecular diffusion and mechanical dispersion. The source/sink term R_k corresponds to injection or production from the wells. The phase flux velocity can be calculated from Darcy's law as shown in equation (2.12).

$$\vec{u}_l = -\frac{K_{rl}\overline{\overline{K}}}{\mu_l}\vec{\nabla} P_l \qquad (2.12)$$

where K_{rl} is the relative permeability, $\overline{\overline{K}}$ is the permeability tensor, μ_l is the phase viscosity.

Tracers typically follow the phase they are going to trace. However, there are some partitioning tracers which can partition and flow with different phases. A water-oil partitioning tracer moves back and forth between the water and oil phases. The partitioning tracers move with the water phase velocity when they are in the water phase, and when they are in the oil phase, they move with the oil phase velocity (Jin et al., 1995). Let T be a partitioning tracer which partitions between oil and water phase as per the distribution or partition coefficient (K_T) then concentration of the tracer in the oil and water phase will depend on K_T as per equation (2.13).

$$\mathrm{K}_T = \frac{C_{To}}{C_{Tw}} \qquad (2.13)$$

where C_{To} and C_{Tw} are concentrations of tracer T in the oil and water phase respectively. K_T is the distribution or partition coefficient of the tracer T. The partition coefficient is a

thermodynamic property having dependence on temperature, salinity, and concentration, and can be measured in the laboratory (Zemel, 1995).

By combining equation (2.11) and (2.12) and assuming two-phase (oil and water) flow, the tracer transport equation can be written as:

$$\frac{\partial}{\partial t}[\phi\ (S_w C_{Tw} + S_o C_{To})] - \nabla^2\left[\overline{\overline{K}}(\lambda_w C_{Tw} + \lambda_o C_{To})\ p\right] - \nabla^2[\phi(S_w D_{Tw} C_{Tw} + S_o D_{To} C_{To})] = R_k \tag{2.14}$$

where S_w and S_o are water and oil saturation respectively, λ_w and λ_o are water and oil phase mobility, D_{Tw} and D_{To} are dispersion coefficient for the tracer T in water and oil phase respectively.

Replacing C_{To} in equation (2.14) from equation (2.13), we get the following equation:

$$\frac{\partial}{\partial t}[\phi(S_w + S_o K_T) C_{Tw}] - \nabla^2\left[\overline{\overline{K}}(\lambda_w + \lambda_o K_T) C_{Tw}\ p\right] - \nabla^2[\phi(S_w D_{Tw} + S_o D_{To} K_T) C_{Tw}] = R_k \tag{2.15}$$

Equation (2.15) with appropriate modification is used for modeling tracer transport in the reservoir and the fracture domain.

2.2.4.2 Tracer transport model in the reservoir domain

Equation (2.15) is used to solve for the tracer transport in the reservoir domain. This equation includes the effect of both convective and diffusive tracer transport. The finite-volume method is used for discretizing the tracer transport equation in the reservoir (matrix) domain. Equation (2.15) for the matrix domain in an integral form can be written as following:

$$\int_{\Omega} \phi(S_w^m + S_o^m K_T) \frac{\partial C_{Tw}^m}{\partial t}\, d\Omega - \int_{\Omega} \nabla.\left(\bar{\bar{K}}(\lambda_w^m + \lambda_o^m K_T) C_{Tw}^m \nabla p_m\right) d\Omega - \int_{\Omega} \nabla.\left(\phi(S_w^m D_{Tw} + S_o^m D_{To} K_T) \nabla C_{Tw}^m\right) d\Omega = Q_{TL}^{fm} \tag{2.16}$$

where m subscript/superscript represents the properties in the matrix domain, Ω is the control volume, C_{Tw}^m is the tracer T concentration in the water phase in the matrix domain, Q_{TL}^{fm} is the tracer-leak off volume rate from fracture to the matrix. This tracer leak-off term also appears in the fracture domain equation with an opposite sign. Tracer leak-off coupling between matrix and fracture domain will be discussed in section 2.2.4.4.

After applying the finite volume discretization for the cell "*i*" on equation (2.16), we get the following equation:

$$\begin{aligned} &\frac{\phi(S_w^m + S_o^m K_T)\Omega}{\Delta t}\left(C_{Tw_i}^{m\ k+1} - C_{Tw_i}^{m\ k}\right) \\ &\quad - \sum_{j=1}^{N_e} \bar{\bar{K}}\,(\lambda_w^u + \lambda_o^u K_T)\Gamma_{jNj} \frac{\left(p_{mi}^{k+1} - p_{miNj}^{k}\right)}{\delta_{iNj}} C_{Tw}^{mu} \\ &\quad - \sum_{j=1}^{N_e} \phi\,(S_w^m D_{Tw} + S_o^m D_{To} K_T)\Gamma_{jNj} \frac{\left(C_{Tw_i}^{m\ k+1} - C_{Tw_{iNj}}^{m\ k+1}\right)}{\delta_{iNj}} \\ &\quad = Q_{TL}^{fm} \end{aligned} \tag{2.17}$$

where Γ_{jNj} is the face area between the owner and neighbor cells. *j* refers to the neighbor cells of cell *i*. where superscript "*u*" represents the properties obtained by upwinding. Upwinding is required for stabilizing the numerical solution in the IMPEC (Implicit pressure explicit concentration) formulation used in our model. Upwinding helps in numerically simulating the direction of propagation of information in the flow field.

2.2.4.3 Tracer transport model in the fracture domain

As mentioned in Section 2.2.2, flow in the fracture is modeled as the flow between two variable-width parallel plates. Based on a similar formulation, equation (2.15) is modified to include the effect of volume change (due to fracture opening/closure) on the tracer transport. Equation (2.18) describes the tracer transport equation in the fracture domain.

$$\begin{aligned}\frac{\partial}{\partial t}\left[w_f\left(S_w^f + S_o^f K_T\right)C_{Tw}^f\right] - \nabla^2\left[\frac{w_f^3}{12}\left(\lambda_w^f + \lambda_o^f K_T\right) C_{Tw}^f\, p^f\right] \\ - \nabla^2\left[w_f\left(S_w^f D_{Tw} + S_o^f D_{To} K_T\right) C_{Tw}^f\right] \\ = q_w C_{Tw}^f + q_o K_T C_{Tw}^f + Q_{TL}^{mf}\end{aligned} \tag{2.18}$$

where superscript f represents the property in the fracture domain, w_f is the fracture width, C_{Tw}^f is the tracer T concentration in the water phase in the fracture domain, q_w and q_o are the water and oil production/injection rates respectively. Q_{TL}^{mf} is the tracer-leak off volume rate from the matrix to fracture.

The first-term on the left-hand side (LHS) of equation (2.18) corresponds to the change in the tracer concentration due to the tracer accumulation and also due to the fracture volume change. Convective tracer flow between fracture elements is captured by the second term on the LHS. The third term on the LHS captures the tracer transport due to the dispersion.

Equation (2.18) is discretized using the finite area method as described in Bryant, (2016). In the finite volume method, a three-dimensional region is discretized spatially into volumes (3D domains). Similarly, in the finite area method, a two-dimensional region is discretized spatially into surfaces (2D domains). Finite area domains are discretized by

arbitrary polygons and require surface data along a finite volume boundary for discretization. Equation (2.18) in an integral form can be written as following:

$$\begin{aligned}
&\int_S w_f\left(S_w^f + S_o^f K_T\right)\frac{\partial C_{Tw}^f}{\partial t}\,dS + \int_S \left(S_w^f + S_o^f K_T\right)C_{Tw}^f \frac{\partial w_f}{\partial t}\,dS \\
&\quad - \oint_{\partial S} n.\frac{w_f^3}{12}\left(\lambda_w^f + \lambda_o^f K_T\right)\nabla p_f\, C_{Tw}^f\, dL \\
&\quad - \oint_{\partial S} n.w_f\left(S_w^f D_{Tw} + S_o^f D_{To} K_T\right)\nabla C_{Tw}^f\, dL \\
&\quad = (q_w + q_o K_T)C_{Tw}^f + \int_S \frac{K_m}{\mu_f}(\lambda_w^u + \lambda_o^u K_T)\frac{p^m - p^f}{\delta_n} C_{Tw}^u
\end{aligned} \tag{2.19}$$

where superscript "*u*" represents the properties obtained by upwinding, and *S* is the control surface for the finite area discretization.

After applying the finite area discretization for face "*i*" on equation (2.19), we get the following equation:

$$\begin{aligned}
&\frac{w_f\left(S_w^f + S_o^f K_T\right)S}{\Delta t}\left(C_{Tw_i}^{f\ k+1} - C_{Tw_i}^{f\ k}\right) + \frac{\left(S_w^f + S_o^f K_T\right)C_{Tw}^f S}{\Delta t}\left(w_{fi}^{k+1} - w_{fi}^k\right) \\
&\quad - \sum_{j=1}^{N_e}\frac{(w_{fe}^k)^3 L_e}{12}\left(\lambda_w^f + \lambda_o^f K_T\right)\frac{\left(p_{fi}^{k+1} - p_{fiNj}^k\right)}{\delta_{iNj}} C_{Twe}^{fu} \\
&\quad - \sum_{j=1}^{N_e}\frac{w_{fe} L_e}{\delta_{iNj}}\left(S_w^f D_{Tw} + S_o^f D_{To} K_T\right)\left(C_{Tw_i}^{f\ k+1} - C_{Tw_{iNj}}^{f\ k+1}\right) \\
&\quad = (q_w^{k+1} + q_o^{k+1} K_T)C_{Tw}^{f\ k+1} \\
&\quad + \frac{K_m S}{\mu_f}(\lambda_w^u + \lambda_o^u K_T)\frac{p^{m^{k+1}} - p^{f^{k+1}}}{\delta_n} C_{Tw}^{fu}
\end{aligned} \tag{2.20}$$

where δ_n is the normal distance between the matrix cell center and the fracture face. "k" refers to the time-step. *j* refers to the neighbor faces of face *i*. w_{fe} is the edge width value which is the average of the width of the owner face and neighbor face.

2.2.4.4 Coupling of matrix and fracture domain tracer equations

The discretized tracer transport equations ((2.17) and (2.20)) for the reservoir and fracture domain are assembled in a single matrix to solve for the tracer transport.

Tracer flow across the matrix fracture interface depends upon the tracer concentration on the fracture faces and the tracer concentration in the crack boundary cells of the reservoir domain. The matrix-fracture tracer flux will, in turn, affect the tracer concentration in the fracture and reservoir domain. This will require multiple iterations to converge if matrix and fracture domain equations are solved sequentially. Iterative solution methodology may also lead to instability in the simulation. To avoid multiple iterations and instabilities, we solve the matrix and fracture domain tracer equations simultaneously. Reservoir and fracture tracer equation matrix coefficients are combined into a single matrix as shown in Figure 2.13.

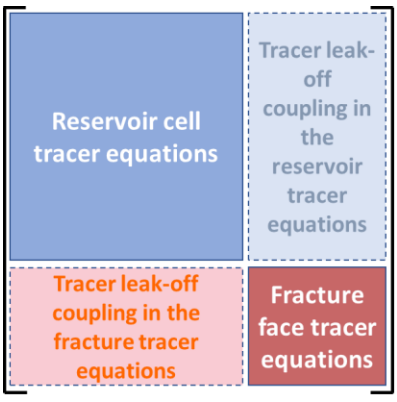

Figure 2.13: Matrix structure for the coupled reservoir and fracture domain tracer equations.

2.2.4.5 Solution algorithm

The tracer transport model is integrated with the geomechanical reservoir simulator developed by Zheng et al., (2019). The overall solution algorithm is shown in Figure 2.14. The tracer model is based on IMPEC (Implicit in pressure, explicit in concentration) implementation. At the start of a time-step, the fracture propagation loop is executed by solving coupled equations for displacement, pressure, fluid distribution, and wellbore (Zheng et al., 2019a). Then the saturation equation is solved. Coupled tracer equations are solved after obtaining the converged values of pressure, saturation, and fracture width. We use GMRES solver (Saad and Schultz, 1986) with an ILUT preconditioner (Saad, 1994) to solve the linear system of equations.

Due to the explicit nature of the coupling between the pressure and the tracer concentration, a smaller time step is required for stability as per the CFL criterion (Courant et al., 1928). In our model, we use an adaptive time-stepping scheme to avoid instability and perform the simulations in reasonable run-time. The adaptive time step algorithm will be discussed in Section 2.2.5.

2.2.4.6 Multiple tracer option

The tracer model developed here can be used to solve for any number of tracers. Based on the user-provided number of tracers, all tracer properties, concentration fields, and equations are populated and stored as a list of pointers. Once the coupled reservoir displacement, pressure, and saturation equations are solved, we loop over and solve tracer transport for all tracers.

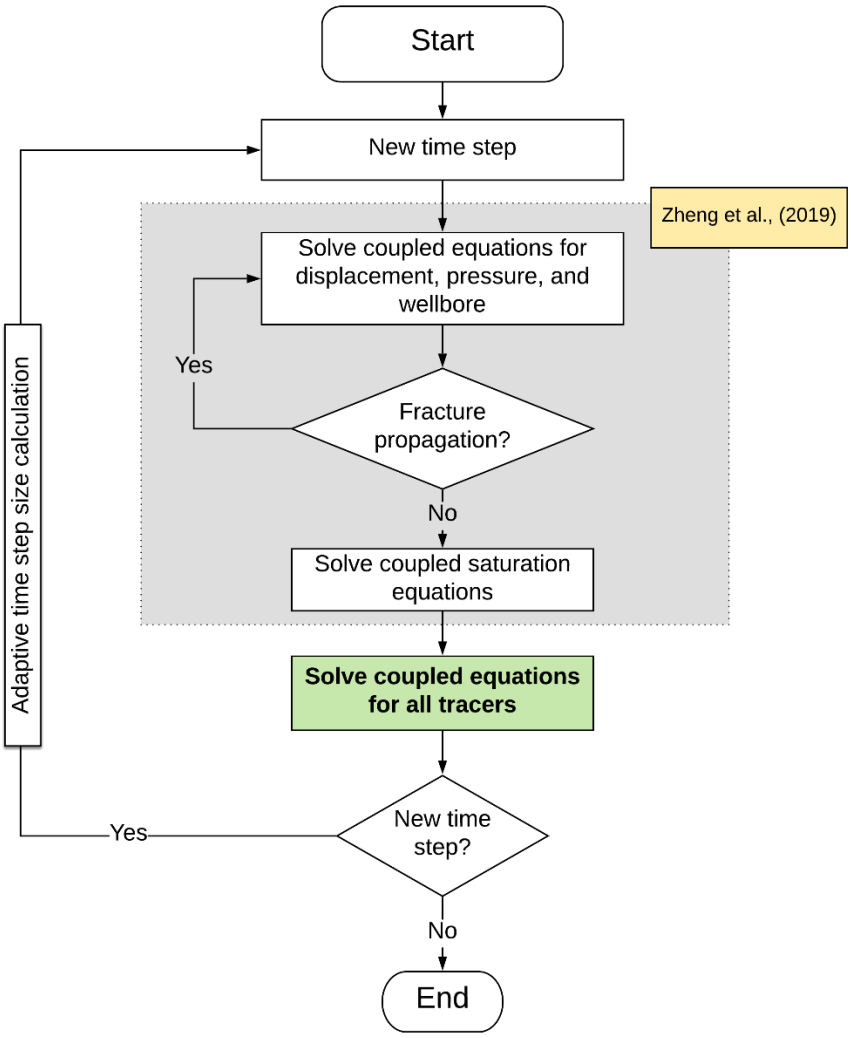

Figure 2.14: Block flow diagram for the tracer transport model integrated in the geomechanical reservoir simulator.

2.2.5 Adaptive time-stepping for production/flowback modeling

Typically, production and flowback simulation runs are conducted for a timescale of a few years. Simulation runtime can be very high when a fixed time-step scheme is used with a small time-step size. On the other hand, a larger time-step can lead to inaccuracies

in the simulation results. In the case of tracer flowback simulations, a smaller time-step is required for the stability (based on the Courant number criterion) due to the explicit coupling between pressure and tracer concentration. During the initial stages of the simulation, there may be sudden changes in the pressure due to the changes in the well operating conditions. Small time-steps are required for capturing these sudden changes accurately. However, during the later stages of the simulation, when the rate of change in the well operating conditions becomes smaller, a larger time-step can also yield in the same accuracy. Therefore, an adaptive time-stepping scheme is developed to adjust the time-step size during the simulation run based on the rate of change in the pressure, saturation, flow rate, and well operating conditions.

The adaptive time-stepping scheme is also coupled with an output time series provided as an input. This output time series is used to decide when to write the simulation results to the disk. At a fixed time-stepping scheme, simulation output write frequency can be increased to minimize the disk storage. However, in the case of an adaptive time-stepping scheme, the simulation output frequency can skip writing simulation results for several time-steps which are required while analyzing the simulation results. Providing an output time series will ensure that simulation results are written at all the times specified in the output time series. Important events in the simulation, such as well open/shut-in time, operating condition change time, and switching to producer from injector, can be defined in the output time series. After these events, a few small increment times can also be defined to ensure that small time-steps are taken after these sudden changes in the operating conditions. Coupling the output time series with the adaptive time-stepping scheme helps in stabilizing the simulation runs. Time step size based on the output time series (Δt_{op}) is calculated as following:

$$\Delta t_{op} = Next\ time\ in\ output\ time\ series - Current\ time \tag{2.21}$$

The time-step is calculated adaptively based on the Courant number, maximum change in the pressure, and saturation in the previous time-step. The Courant number is calculated based on the flux across all faces for a given cell as shown in equation (2.22).

$$C_{o_l} = \left(\frac{\sum_{k=0}^{N} \overrightarrow{u_l} \,.\, \overrightarrow{S_{fk}}}{2V_{cell}} \right) \Delta t \tag{2.22}$$

where C_{o_l} is the Courant number for phase l, the summation (k) is for all faces (N) of the given cell, $\overrightarrow{S_{fk}}$ is the face area vector of face k, $\overrightarrow{u_l}$ is the velocity vector of phase l at face k, Δt is the current time-step.

At the end of a time-step, change in the pressure and saturation is calculated for all fracture and reservoir cells. The maximum change for a property is compared against the specified tolerance value and a time-step update scaling factor ($\mathrm{sf}_{\Delta \mathrm{tp}}$) is calculated as following:

$$\mathrm{sf}_{\Delta \mathrm{tp}} = \frac{\max change}{tolerance} \tag{2.23}$$

The scaling factor is calculated for each property (pressure, saturation, and Courant number). The minimum of these scaling factors is used to calculate the next time-step size:

$$\Delta t_{next} = min\left[\Delta t_{op}\,, max\{\Delta \mathrm{t}_{min}\,, min\left(\Delta \mathrm{t}_{\mathrm{previous}} * \min(\mathrm{sf}_{\Delta \mathrm{tp}}), \Delta \mathrm{t}_{max}\right)\}\right] \tag{2.24}$$

where $\Delta \mathrm{t}_{min}$ and $\Delta \mathrm{t}_{max}$ are defined as a simulation input to avoid unreasonably small or large time-step.

2.2.6 Automated history matching

History matching is an important step in building a reservoir model that can be used for production forecasting, sensitivity analysis, and optimization. In a history matching process, reservoir and flow properties are adjusted to reproduce the historical production data or other measurements from the field. An objective function is defined as the difference between the historical/observed data and the simulated results. The history matched model is obtained by minimizing the objective function. An automated history matching approach can help in obtaining the history matched model faster as compared to a manual history match approach.

We implemented the history matching model using the simulated annealing algorithm developed by Zhang et al., (2019) and Shiriyev, (2018). A simulated annealing algorithm randomly generates the new set of model parameters based on a cooling function. The cooling function allows larger jumps in the model parameter during the early phase of the parameter search and smaller jumps at the end of the search. In this algorithm, the new model parameter search is derivative-free, which helps in finding the global minimum of the history matching objective function.

We have used this history matching algorithm to estimate the effective permeability of the stimulated reservoir volume (SRV) (see chapter 4). We history match the production rates from the complex fracture network simulation model to the production from an equivalent SRV simulation model production rates. We use the SRV extent and SRV permeability tensor as the history matching parameters. History matched case parameters are used to calculate the principal component and direction of SRV permeability tensor.

2.2.7 Coupling with Multi-Frac-NF for parent-child interactions

We developed a workflow to simulate parent-child well interactions by integrating the OpenFOAM model developed here with a hydraulic fracturing simulator Multi-Frac-NF (Shrivastava and Sharma, 2018a). The integrated simulation workflow for parent-child well interactions is shown in Figure 2.15.

Figure 2.15: Simulation workflow for parent-child well interaction.

Parent well fracturing is simulated in Multi-Frac-NF. The created hydraulic fracture information is used in the OpenFOAM reservoir simulation model to obtain the pressure and stress profile in the reservoir after parent well depletion. In our reservoir simulation model, there is a two-way coupling between the reservoir pressure and geomechanical displacement as per equation (2.6). The strain (ϵ) in the reservoir is calculated using the updated displacement field as per equation (2.25).

$$\epsilon = \frac{1}{2}\left[\nabla U + (\nabla U)^T\right] \tag{2.25}$$

where U is the displacement vector. Stress-strain constitutive relation (equation (2.26)) is used to calculate effective stress (σ) in the reservoir. Total stress (S) after depletion is calculated based on the effective stress, pore pressure, and Biot's coefficient as per equation (2.27).

$$\sigma = 2\mu\epsilon + \lambda * I * tr(\epsilon) + \sigma_0 \tag{2.26}$$

$$S = \sigma - \alpha pI \tag{2.27}$$

The parent well depletion-induced altered total stress (S) profile is exported to Multi-Frac-NF for the child well fracturing simulation. The created child well fractures and parent well fractures are used in the reservoir simulation model for production simulation.

2.3 MODEL VERIFICATION

This section presents verification cases to evaluate the accuracy of the developed model.

2.3.1 Verification for reservoir and fracture flow

The developed OpenFOAM model results were compared with a commercial reservoir simulator CMG. CMG is based on the finite-difference method with Cartesian grids, and it also provides the capabilities of local grid refinement. Hydraulic fractures are defined as high permeability grid blocks. Local grid refinement near the fracture region helps in capturing the pressure gradient accurately. We present two cases for verification. In the first case, we simulate production from an orthogonal fracture network, and in the second case, we compare the results for a non-orthogonal fracture.

2.3.1.1 Case-1: Complex fracture network consisting of orthogonal fractures

A schematic for the top view of the complex fracture network consisting of orthogonal fractures is shown in Figure 2.16. The reservoir and fluid properties for this case are shown in Table 2.2. We assumed single-phase flow and the fracture width was kept constant. Hydraulic fracture width and permeability for the CMG simulation was

calculated based on equivalent fracture conductivity for the given fracture width (0.1 mm in OpenFOAM simulations).

A comparison of the production rate and cumulative production is shown in Figure 2.17 and Figure 2.18 respectively. We observed an excellent match between the OpenFOAM model results and the CMG simulation results. Figure 2.19 and Figure 2.20 show a comparison for the pressure profile in the reservoir after 150 days and 1000 days of production. From these figures, we can see that the results from the OpenFOAM model developed here are very consistent with the CMG results.

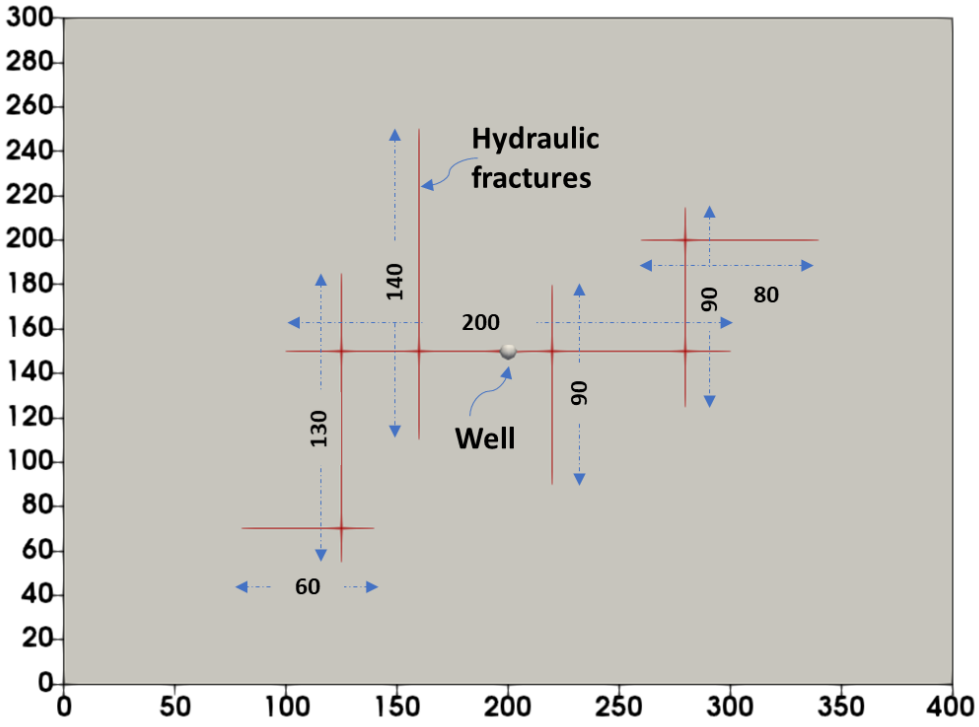

Figure 2.16: Schematic for the verification case for a orthogonal complex fracture network. Reservoir and fracture dimensions are shown in meters.

Table 2.2: Properties used for the orthogonal complex fracture network verification case.

Parameters	Value
Initial reservoir pressure	40000 kPa
Production well bottom-hole pressure	10000 kPa
Reservoir permeability	500 nD
Reservoir porosity	0.1
Reservoir fluid compressibility	4.54E-7 kPa^{-1}
Reservoir fluid viscosity	1 cP
Hydraulic fracture width	0.1 mm

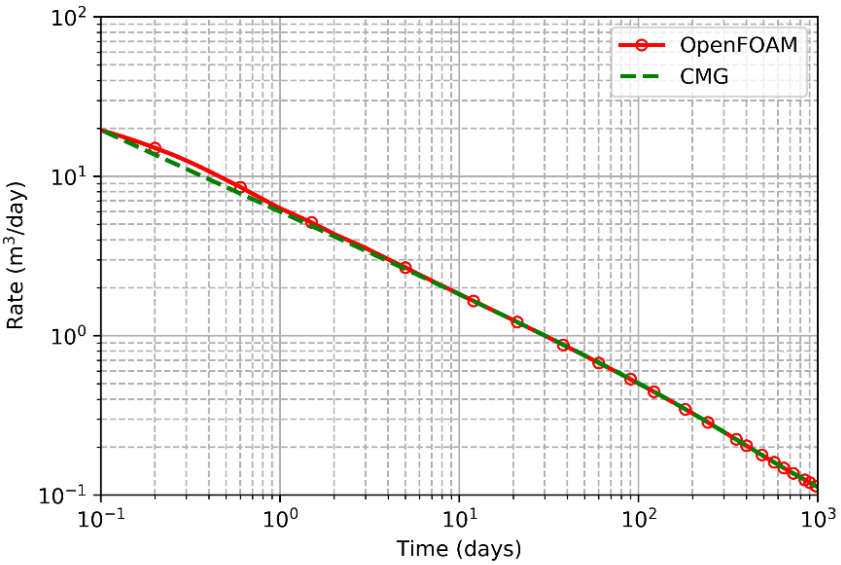

Figure 2.17: Comparison of the OpenFOAM model results with the CMG simulation for the production rate from the orthogonal complex fracture network.

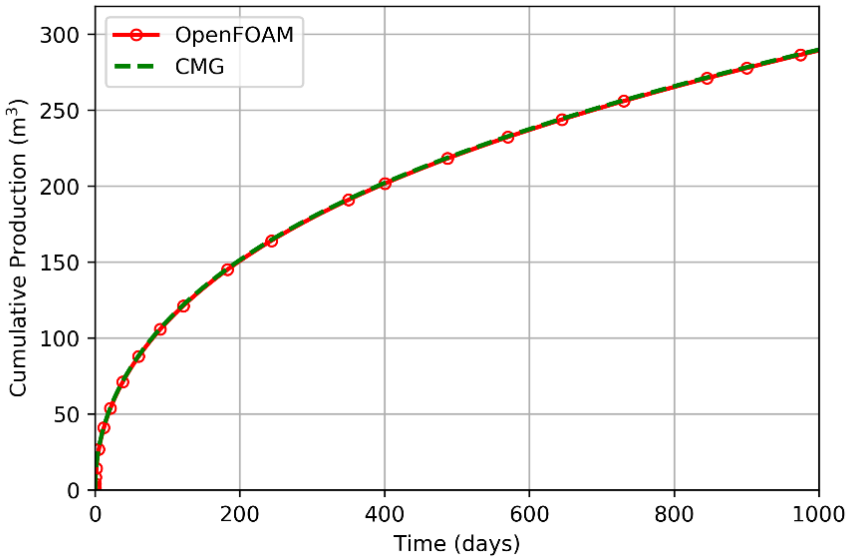

Figure 2.18: Comparison of our OpenFOAM model results with the CMG simulation for the cumulative production from the orthogonal complex fracture network.

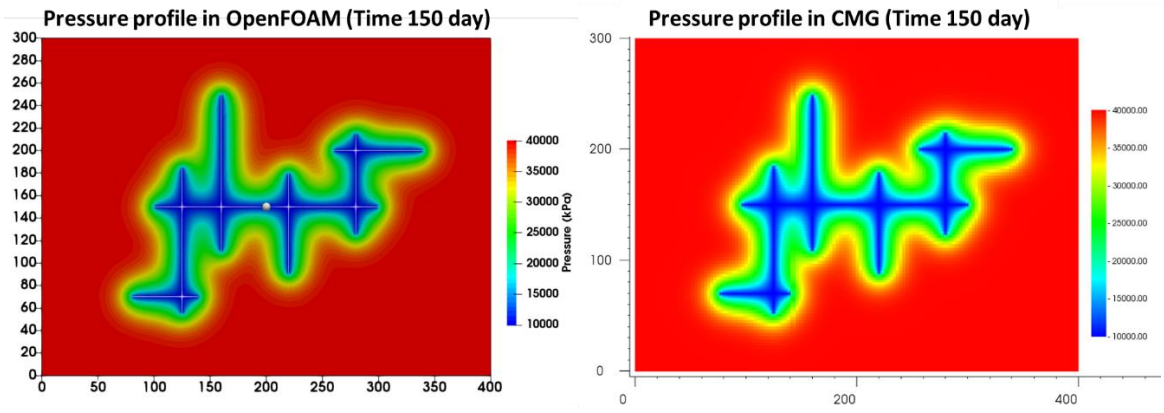

Figure 2.19: Comparison of the developed OpenFOAM model results with the CMG simulation for the pressure profile in the reservoir after 150 days of production.

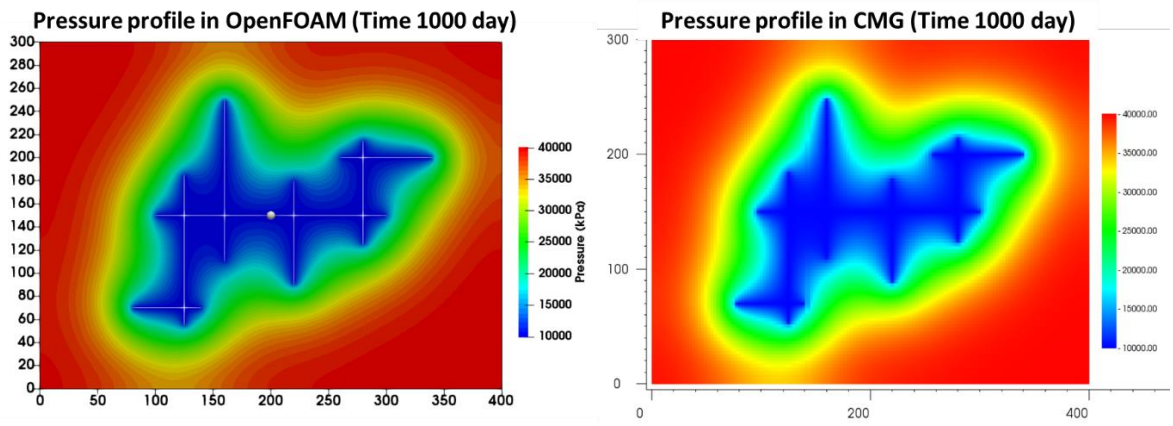

Figure 2.20: Comparison of our OpenFOAM model results with the CMG simulation results for the pressure profile in the reservoir after 1000 days of production.

2.3.1.2 Case-2: Non-orthogonal fracture network

A schematic of the top view of the non-orthogonal fracture case is shown in Figure 2.21. A hydraulic fracture is oriented at an angle of 45^0 from the wellbore direction. This type of fracture propagation can occur if the wellbore is not aligned in the direction of minimum stress. Modeling a non-orthogonal fracture with local grid refinement in a structured Cartesian grid system is very difficult. In CMG, this type of fracture geometry can be defined using a zigzag pattern of high permeability grid blocks as shown in Figure 2.22. A Cartesian grid (500 x 500) with a uniform small grid size equal to the fracture grid size is used throughout the simulation domain. In the case of OpenFOAM, non-orthogonal fracture geometry is defined using an unstructured grid (Figure 2.23). In the case of unstructured gridding, only the region close to the hydraulic fracture is refined. This helps in reducing the number of cells for simulating non-orthogonal fractures. The reservoir and fluid properties for this case are shown in Table 2.3.

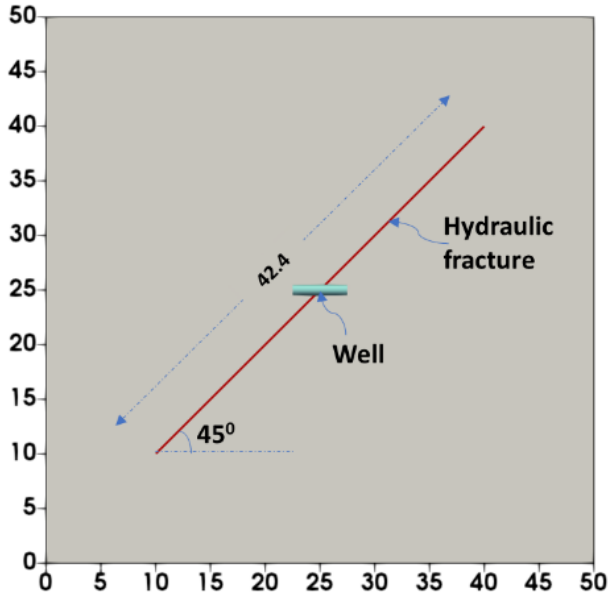

Figure 2.21: Schematic for the non-orthogonal fracture case. A hydraulic fracture is oriented at an angle of 45^0 from the wellbore direction.

Table 2.3: Properties used for the non-orthogonal fracture verification case

Parameters	**Value**
Initial reservoir pressure	40000 kPa
Production well bottom-hole pressure	10000 kPa
Reservoir permeability	100 nD
Reservoir porosity	0.1
Reservoir fluid compressibility	1E-6 kPa^{-1}
Reservoir fluid viscosity	1 cP
Hydraulic fracture width	0.1 mm

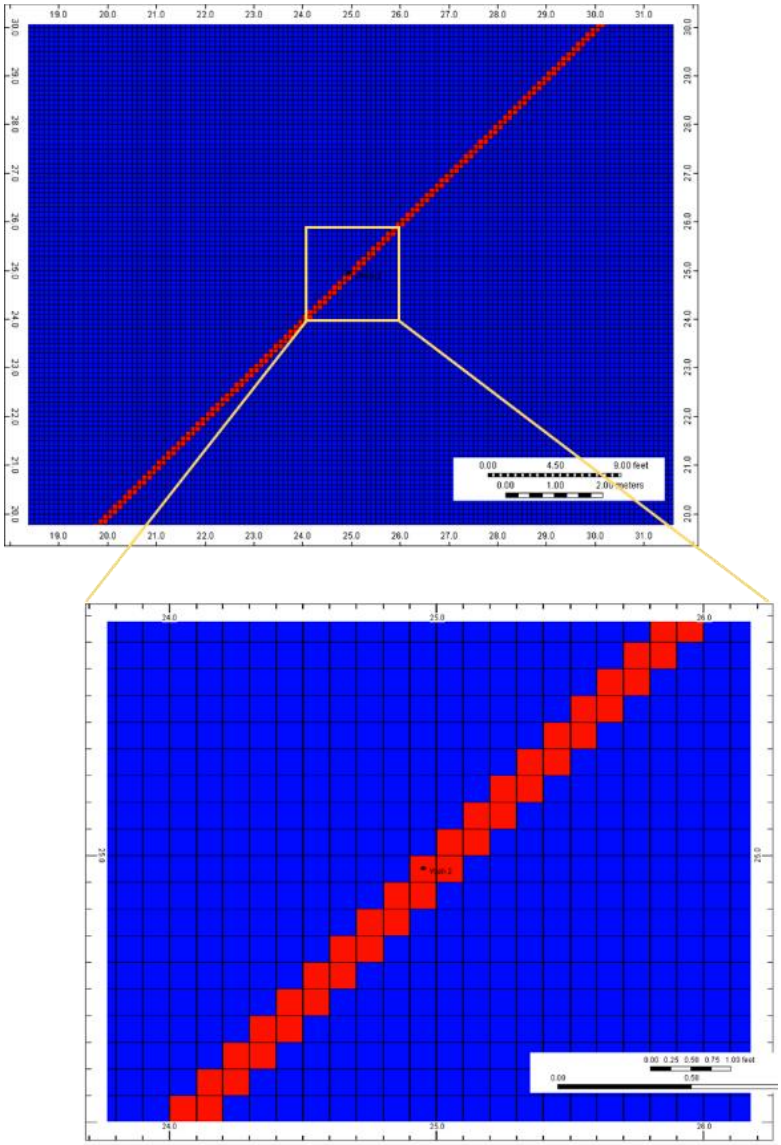

Figure 2.22: Non-orthogonal fracture in a Cartesian grid is modeled as a zigzag pattern. Red colored grids are the high permeability fracture gridblocks. (Total number of cells = 250,000)

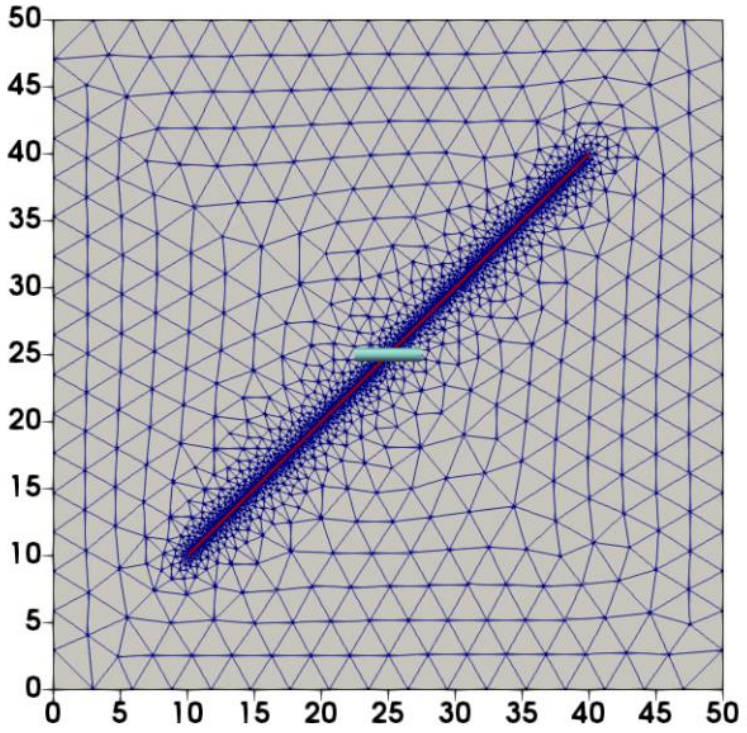

Figure 2.23: Non-orthogonal fracture modeled using unstructured gridding. (Total number of cells = 5,298)

Figure 2.24 and Figure 2.25 show a comparison of the developed OpenFOAM model results with the CMG simulation results for production from a non-orthogonal hydraulic fracture. We observe that our model results match very well with a commercial reservoir simulator CMG. However, the number of grid blocks needed to model the non-orthogonal fracture is much smaller when an unstructured grid is used.

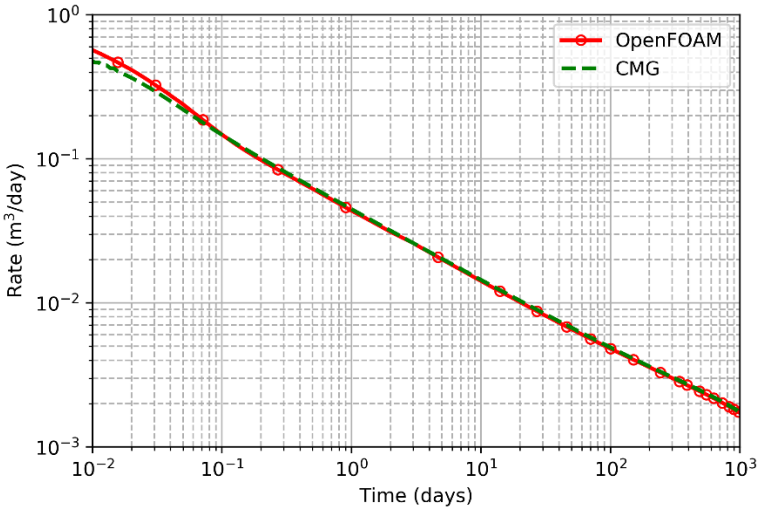

Figure 2.24: Comparison of our OpenFOAM model results with CMG simulation results for the production rate from a non-orthogonal fracture.

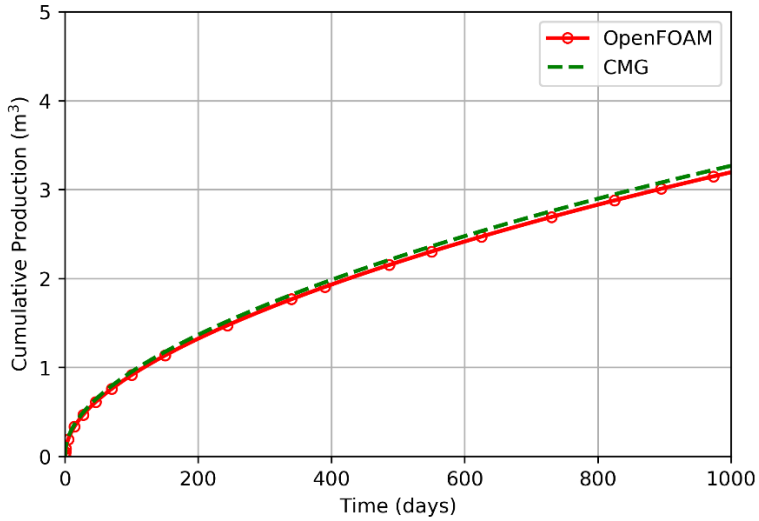

Figure 2.25: Comparison of our OpenFOAM model results with CMG simulation results for the cumulative production from a non-orthogonal fracture.

2.3.2 Verification for tracer transport model

For verification with an analytical solution, we simulated a case of an ideal non-partitioning tracer flow in a slot at a constant velocity (Figure 2.26). The initial and boundary conditions are shown in equations ((2.28), (2.29), and (2.30)).

$$C(x,0) = C_i \tag{2.28}$$

$$C(0,t) = C_{inj} \tag{2.29}$$

$$C(\infty,t) = C_i \tag{2.30}$$

where C_i is the initial tracer concentration, and C_{inj} is the injected tracer concentration.

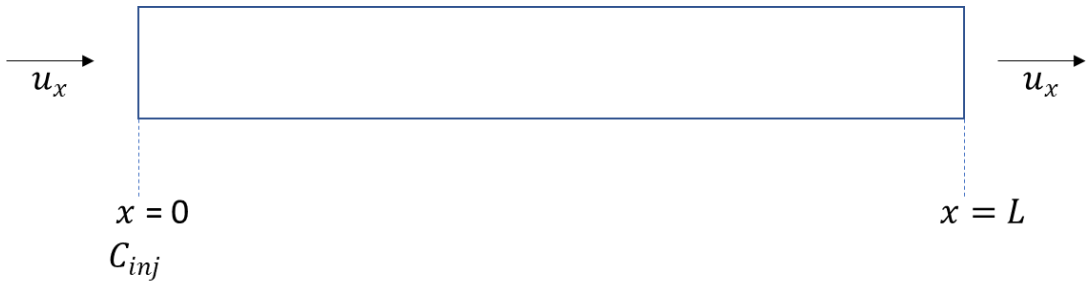

Figure 2.26: Schematic for the tracer transport verification case.

For an ideal non-partitioning tracer in single-phase flow, tracer transport equation (2.11) can be simplified as:

$$\varphi \frac{\partial C_w}{\partial t} + \vec{\nabla}.(\vec{u}_w) - \varphi D_w \nabla^2 (D_w C_w) = Q \tag{2.31}$$

For a one-dimensional flow, equation (2.31) can be modified as the convection dispersion equation as shown in equation (2.32).

$$\frac{\partial C}{\partial t} + u_x \frac{\partial C}{\partial x} - D_L \frac{\partial^2 C}{\partial x^2} = 0 \tag{2.32}$$

where u_x is the interstitial velocity (u_w/ϕ), D_L is the dispersion coefficient. This equation can be converted to a dimensionless form as shown in

$$\frac{\partial C}{\partial t_D} = \frac{1}{N_{Pe}} \frac{\partial^2 C_D}{\partial x_D^2} - \frac{\partial C_D}{\partial x_D} \tag{2.33}$$

Where

$$x_D = \frac{x}{L} \tag{2.34}$$

$$t_D = \frac{u_x t}{L} = \frac{qt}{A\phi L} \tag{2.35}$$

$$C_D = \frac{C(x,t) - C_i}{C_{inj} - C_i} \tag{2.36}$$

$$N_{Pe} = \frac{u_x L}{D_L} \tag{2.37}$$

While simulating the one-dimensional tracer transport with a constant concentration injection well at $x_D = 0$, the concentration at the well is not constant due to the immediate dispersion at the injection cell. The initial and boundary conditions as shown in equations (2.28), (2.29), and (2.30) can be modified as shown in following equations.

$$C_D(x_D, 0) = 0 \tag{2.38}$$

$$C_D(0, t_D) - \frac{1}{N_{Pe}} \frac{\partial C_D}{\partial x_D} = 1 \tag{2.39}$$

$$C_D(\infty, t_D) = 0 \tag{2.40}$$

(Brenner, 1962) provided the analytical solution for equation (2.33) with given initial and boundary conditions (equations (2.38), (2.39), and (2.40)):

$$
\begin{aligned}
C_D(x_D, t_D) = \quad & \frac{1}{2} erfc\left[\sqrt{\frac{N_{Pe}}{4t_D}}(x_D - t_D)\right] + \sqrt{\frac{N_{Pe} t_D}{\pi}} exp\left[\frac{-N_{Pe}}{4t_D}(x_D - t_D)^2\right] \\
& - \frac{1 + N_{Pe}(x_D + t_D)}{2} \exp(N_{Pe} x_D)\, erfc\left[\sqrt{\frac{N_{Pe}}{4t_D}}(x_D + t_D)\right] \\
& + 2\sqrt{\frac{N_{Pe} t_D}{\pi}}\left[1 + \frac{N_{Pe}(2 - x_D + t_D)}{4}\right] exp\left[N_{Pe} - \frac{N_{Pe}(2 - x_D + t_D)^2}{4t_D}\right] \\
& - \frac{1}{2} N_{Pe}\left[2(2 - x_D + t_D) + t_D + \frac{N_{Pe}(2 - x_D + t_D)^2}{2}\right] \exp\,(N_{Pe}) erfc\left[\sqrt{\frac{N_{Pe}}{4t_D}}(2 - x_D + t_D)\right]
\end{aligned}
\tag{2.41}
$$

We compared our tracer model results with the analytical solution provided in equation (2.41). Inputs for the verification case are shown in Table 2.4. Figure 2.27 shows the plot of dimensionless concentration (C_D) versus dimensionless distance (x_D) for the developed model (numerical) and the analytical solution. We obtained an excellent match of our numerical model results with the analytical model.

Table 2.4: Properties used for the tracer transport verification case

Parameters	**Value**
Injected tracer concentration (C_{inj})	0.01
Initial tracer concentration (C_i)	0
Flow rate (q)	5e-6 m^3/sec
Length (L)	40 m
Dispersion coefficient (D_L)	1e-2 m^2/sec
Peclet number (N_{Pe})	20

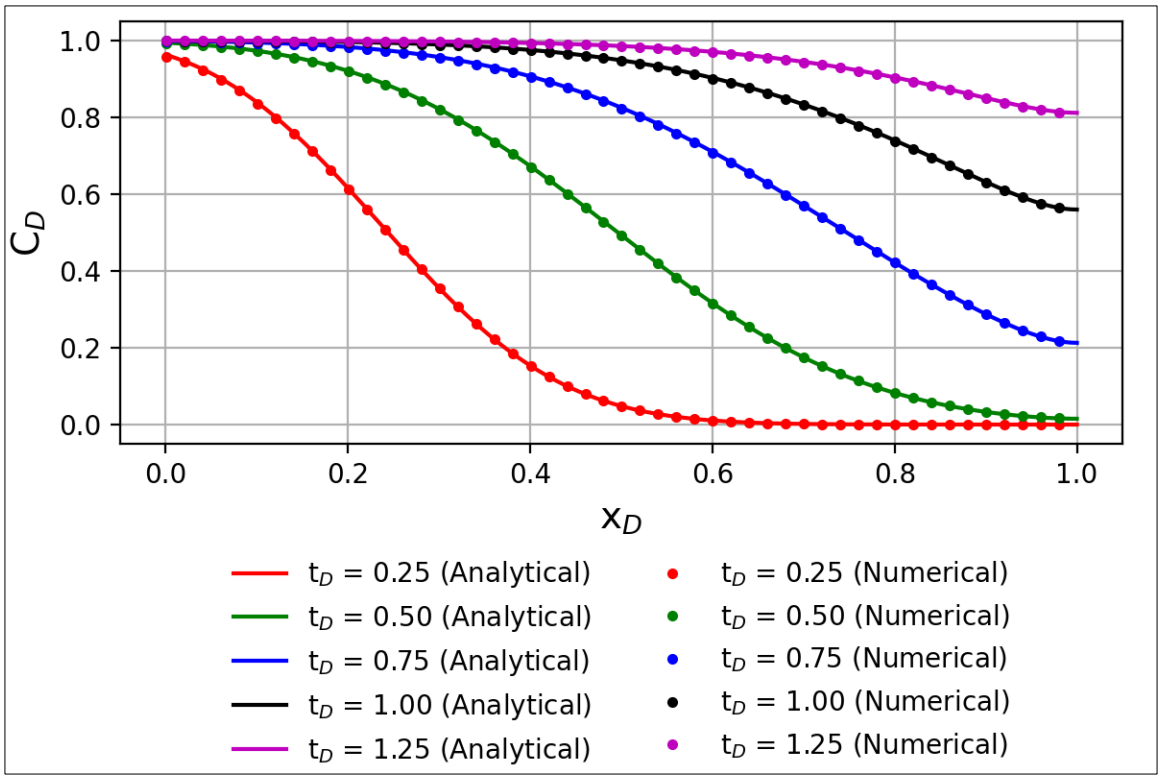

Figure 2.27: Comparison of our numerical model results with the analytical solution for a convection dispersion equation.

2.4 Conclusions

In this chapter, we developed a model to simulate production from complex fracture networks. An automated meshing methodology was used to create the finite-volume mesh for any arbitrarily shaped fracture network and the reservoir. Our reservoir – fracture network model can account for fracture closure effects during production.

We also developed a tracer transport model that can simulate tracer injection and flowback coupled with fracture propagation and closure. Tracer transport governing equations in the fracture and reservoir domain were presented. We presented the finite volume and finite-area discretization for the tracer transport equation in the reservoir and

fracture domains. A single coupled equation for each tracer is solved after converging on the pressure and displacements. The tracer transport model developed here can help in analyzing the fracture-wellbore connectivity during flowback. These results will be presented in Chapter 6.

An adaptive time-stepping scheme which is coupled with an output time series, was developed to conduct large time scale simulations efficiently. An automated history matching model using a simulated annealing algorithm developed by Zhang et al., (2019) and Shiriyev, (2018) was implemented. The history matching model can be used to estimate the effective permeability of the stimulated reservoir volume (results presented in Chapter 4).

We also presented a workflow to simulate parent-child well interactions by integrating a hydraulic fracturing simulator (Shrivastava and Sharma, 2018a) with the reservoir simulation model. The application of this model will be presented in Chapter 5.

We verified and validated our OpenFOAM model results by comparing it with a commercial reservoir simulator and an analytical solution. We obtained excellent matches for production and tracer transport simulations.

Chapter 3: Optimizing Drawdown Strategies in Wells Producing from Complex Fracture Networks

In the previous chapter, we presented a geomechanics coupled reservoir simulator to simulate production from complex fracture networks. In this chapter, we present an application of the developed model to analyze the impact of fracture closure on production from wells producing from reservoirs with complex fracture networks. During drawdown, the fracture network experiences large changes in the stresses which can affect the fracture conductivity, fracture connectivity to the wellbore, and hence the production rate. This chapter also presents a workflow to find an optimum drawdown strategy in which the fractures can remain conductive while maintaining a high enough drawdown to maximize production.

3.1 INTRODUCTION

In unconventional reservoirs, hydraulic fracturing stimulation is performed to maximize the surface area for the production of hydrocarbons. The productivity of an unconventional well primarily depends on the reservoir rock properties, completion techniques, and production practices. Typically, the focus of a field development plan is on landing the well in sweet spots and optimizing fracturing treatments to maximize fracture surface area. However, production practices such as drawdown pressure management can also affect well productivity. A significant decline in the productivity of

This chapter is adapted from papers SPE-194119 (Kumar, A., Seth, P., Shrivastava, K. and Sharma, M.M., 2018. "Optimizing drawdown strategies in wells producing from complex fracture networks." In SPE International Hydraulic Fracturing Technology Conference and Exhibition. Society of Petroleum Engineers) and ARMA-18-695 (Seth, P., Kumar, A., Manchanda, R., Shrivastava, K. and Sharma, M.M., 2018. "Hydraulic Fracture Closure in a Poroelastic Medium and its Implications on Productivity." In 52nd US Rock Mechanics/Geomechanics Symposium. American Rock Mechanics Association). In both papers, Kumar developed the geomechanical reservoir simulation model for complex fracture networks, designed and performed the research, and documented the results.

unconventional reservoirs due to unmanaged drawdown pressure is observed in several field studies (Okouma Mangha et al., 2011; Rojas et al., 2018). Unconventional reservoirs are often overpressured, and a decrease in the well bottomhole pressure leads to a substantial increase in the effective stress acting on the fracture and the proppant pack. The increased effective stress can decrease fracture conductivity due to fracture closure, proppant crushing, and proppant embedment (Barree and Mukherjee, 1995; Robinson et al., 1988).

The presence of natural fractures in these overpressured, ultra-low permeability reservoirs can lead to the formation of complex fracture networks (Fisher et al., 2002; Shrivastava and Sharma, 2018a; Weng et al., 2011). The productivity of an unconventional reservoir depends on the connectivity of these complex fractures with the producing wellbore.

Closure of fracture segments in a complex fracture network can cause a major portion of a complex fracture network, which would have otherwise contributed to production, to disconnect from the wellbore. The phenomenon of fracture closure can be confirmed by the very low tracer recovery consistently observed during tracer flowback tests (Kumar and Sharma, 2018) and the loss in well connectivity during an interference test (Kumar et al., 2018). Fracture closure depends upon the in-situ reservoir stresses, pore pressure, fracture network complexity, proppant distribution as well as the drawdown strategy implemented for production.

The drawdown strategy has a significant influence on the dynamic behavior of fracture closure and near-wellbore damage. Typically, drawdown pressure is controlled by choke opening during production. In a faster choke opening strategy, flowing well bottomhole pressure is reduced quickly, and it can be referred to as an aggressive

drawdown management strategy. In a conservative drawdown strategy, strategy choke opening is gradual, and higher well bottomhole pressure is maintained for a longer time.

A conservative drawdown strategy has several benefits in terms of minimizing fracture damage and maintaining a high-enough fracture conductivity for a longer duration of time. It can also help in protecting the surface equipment by reducing sand production (Karantinos et al., 2016). A slow opening of the choke can negatively impact the NPV (Net Present Value) due to the low initial production rate. On the other hand, an aggressive drawdown strategy with relatively high initial production rates will result in higher NPV and reduce the temporary surface equipment costs (faster clean up) (Wilson et al., 2016). However, as a consequence of high initial production rates and rapid fracture closure, the fracture network connected to the producing wellbore may get damaged, resulting in lower cumulative production in the longer term. Therefore, it is essential to optimize the drawdown strategy in complex fracture networks to obtain a high initial production rate without damaging the fracture network connectivity to the wellbore.

In this chapter, we analyze the impact of drawdown strategy on the production from a well producing from a reservoir with a complex fracture network. Our geomechanical reservoir simulation model captures the behavior of fracture closure using a Barton-Bandis type normal contact stiffness relationship (Bandis et al., 1983) as explained in chapter 2. The impact of rock mineralogy on unpropped fracture conductivity is also accounted for by modeling stress-dependent permeability from experimental results (Wu et al., 2017). We analyze the short-term and long-term impacts of drawdown dependent fracture closure on cumulative production. Finally, a net present value (NPV) maximization approach is used to determine an optimum drawdown strategy.

3.2 IMPACT OF FRACTURE CLOSURE ON PRODUCTIVITY

We explain the phenomenon of fracture closure with the help of a simple simulation case. We simulate the production from a vertical hydraulic fracture in 3-D, which has partly opened along a weak horizontal bedding plane (Figure 3.1). Two modeling scenarios have been considered. In the first scenario, the hydraulic fracture has a constant width throughout production. However, in the second scenario, the hydraulic fracture width depends upon the stress variations around the fracture, which can cause the fracture to close. The objective of this case study is to compare cumulative production between the two scenarios, and thereby, make quantitative inferences on how much fracture closure impacts productivity. The reservoir and fluid properties used for these simulations are summarized in Table 3.1.

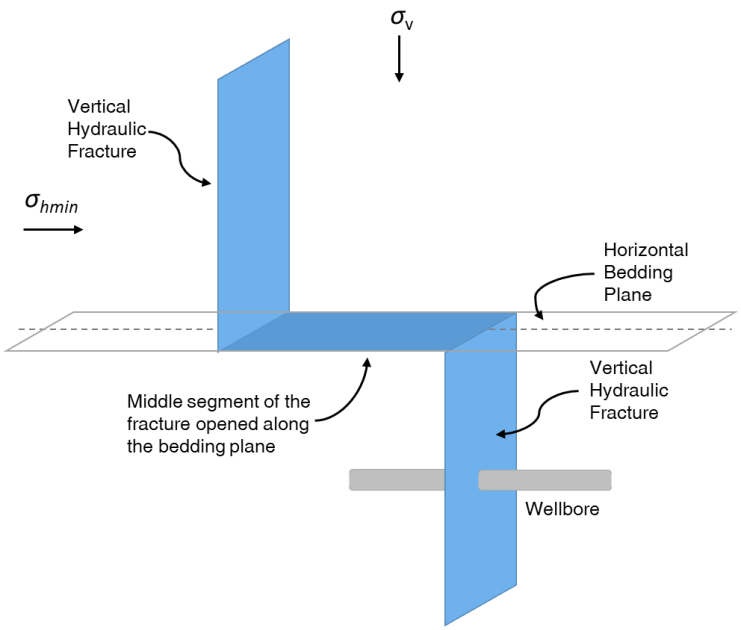

Figure 3.1: Simulation setup for a vertical fracture partly opened along a weak horizontal bedding plane.

Table 3.1: Reservoir and fluid properties used for simulating production from a vertical hydraulic fracture with and without fracture closure.

Property	**Value**
Porosity	0.09
Permeability	300 nD
Initial Reservoir Pressure	7200 psi
Young's Modulus	2.9E+06 psi
Poisson's Ratio	0.25
Viscosity	1 cP
Fluid Compressibility	3.45E-06 psi^{-1}
Vertical overburden stress (S_{Hmax})	12000 psi
Minimum Horizontal Stress (S_{hmin})	11500 psi

During production, the bottom-hole pressure is applied as a Dirichlet boundary condition at the wellbore. For the scenario where we consider fracture closure, as the pressure inside the fracture-well system decreases, the local normal compressive stress acting on the fracture faces increases. This leads to a reduction in the fracture width and fracture conductivity. As seen in Figure 3.2, the segment of the hydraulic fracture that opens against the vertical overburden stress (σ_v), which is in the maximum principal stress direction, has a smaller initial width and closes much faster compared to the segments that open against the minimum horizontal stress (σ_{hmin}). As a result, a large portion of the hydraulic fracture that would otherwise contribute to production loses connectivity from the wellbore. This disconnected part of the hydraulic fracture has a lower contribution to production.

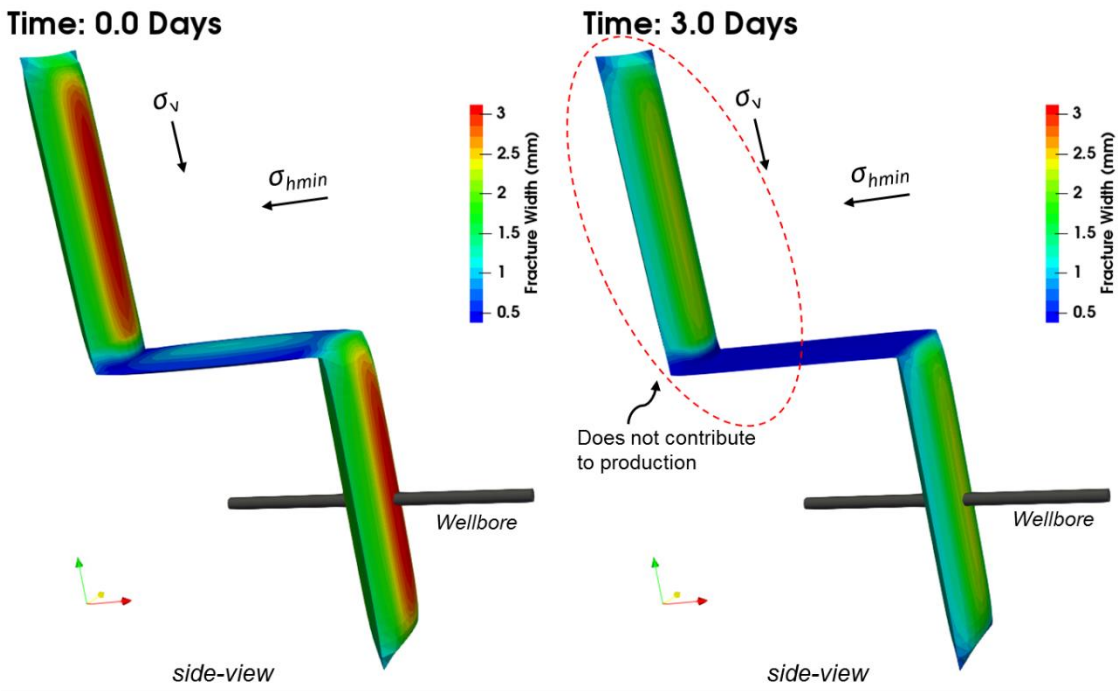

Figure 3.2: Hydraulic fracture width profile in 3-D. The middle segment of the hydraulic fracture that opens against the vertical stress closes much sooner, and cuts-off production from the top segment of the fracture.

The effect of the fracture closure on production can be visualized in Figure 3.3, where we see very different pressure profiles for the two cases. In the case where we do not model fracture closure (Figure 3.3A), we see that all fracture segments contribute to production throughout the production period. However, if fracture closure is considered (Figure 3.3B), we observe that only the part of the fracture that is open and connected to the well contributes towards production.

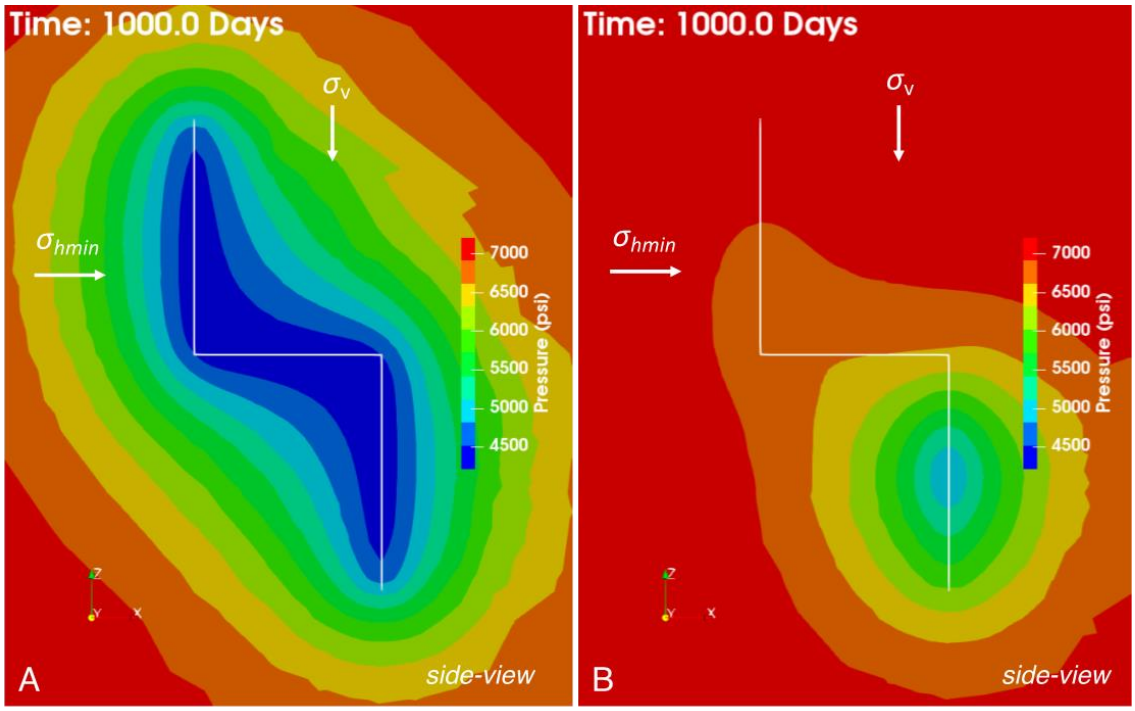

Figure 3.3: Contrasting reservoir pressure profile during production for case A (no closure) and case B (with fracture closure).

Thus fracture closure creates a significant impact on the resulting cumulative production, with actual production being 75% of what would have been otherwise expected if fracture closure was not considered (Figure 3.4). It can, therefore, be inferred from this case study that it is important to model fracture closure to generate accurate production forecasts.

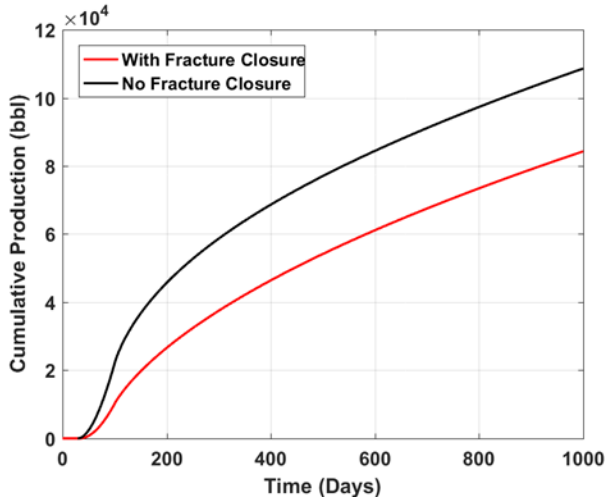

Figure 3.4: The cumulative production is significantly impacted by fracture closure, with production reduced to nearly 75% of what is otherwise expected in the absence of fracture closure.

Next, we simulate production from a 2-D complex fracture network. The complex fracture network is generated by accounting for the interactions between hydraulic fractures and natural fractures during fracture propagation. Multi-Frac-NF, a displacement-discontinuity method (DDM) based hydraulic fracture propagation simulator (Shrivastava and Sharma, 2018a) was used to generate the complex fracture network geometry shown in Figure 3.5. We again consider two scenarios – 1) The hydraulic fracture network has a constant width throughout production, and 2) Hydraulic fracture network width depends upon the stress variations around the fracture, which can cause the fracture to close. The reservoir and fluid properties used in this simulation have been summarized in Table 3.2.

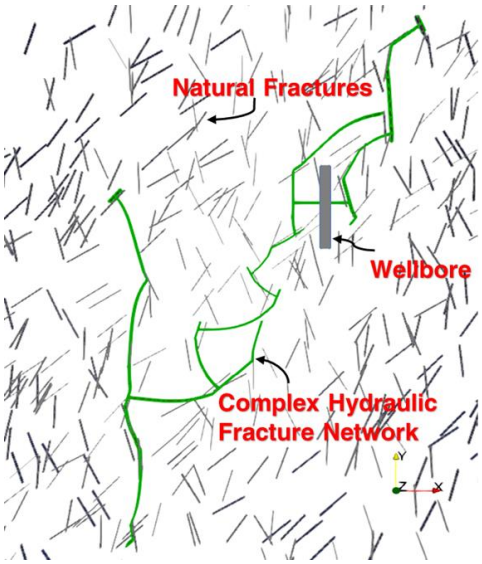

Figure 3.5: A 2-D complex fracture network created by the interactions of a propagating hydraulic fracture with multiple natural fractures.

Table 3.2: Reservoir and fluid properties used for simulating production from a 2-D complex fracture network with and without fracture closure.

Property (Unit)	**Value**
Porosity	0.1
Permeability	100 nD
Initial Reservoir Pressure	2000 psi
Young's Modulus	2.9E+06 psi
Poisson's Ratio	0.25
Viscosity	1 cP
Fluid Compressibility	3.45E-06 psi^{-1}

Simulation results (Figure 3.6) indicate that the segments of the complex fracture network that open against the maximum horizontal stress (σ_{hmax}), have a smaller initial width and close faster compared to the segments that open against the minimum horizontal stress (σ_{hmin}). Early closure of the segments, which open against σ_{hmax}, causes all the remaining segments that are connected to the producing well through that segment to be cut-off from the producing network. As a consequence, a large portion of the complex fracture network that would otherwise contribute to production is rendered useless (Figure 3.7). This results in a significant decrease in the area available for flow from the matrix into the fracture. The actual production, therefore, turns out to be significantly less than expected.

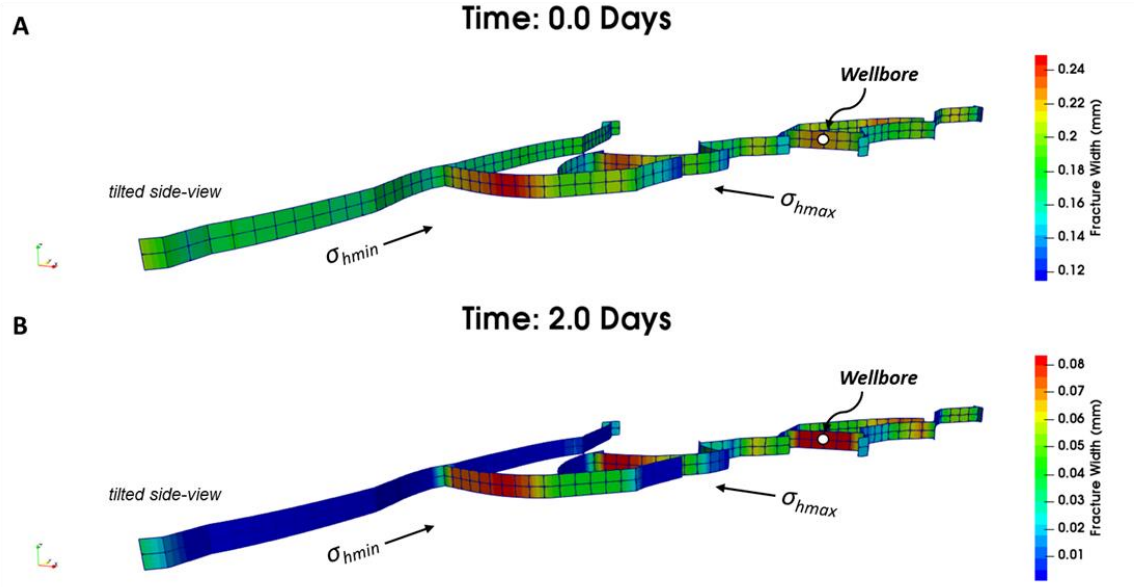

Figure 3.6: (A) Hydraulic fracture width profile at the start of the simulation, and (B) after two days. Segments of the fracture that open against the larger σ_{hmax} have a smaller initial width and close much earlier than the segments that open against σ_{hmin}.

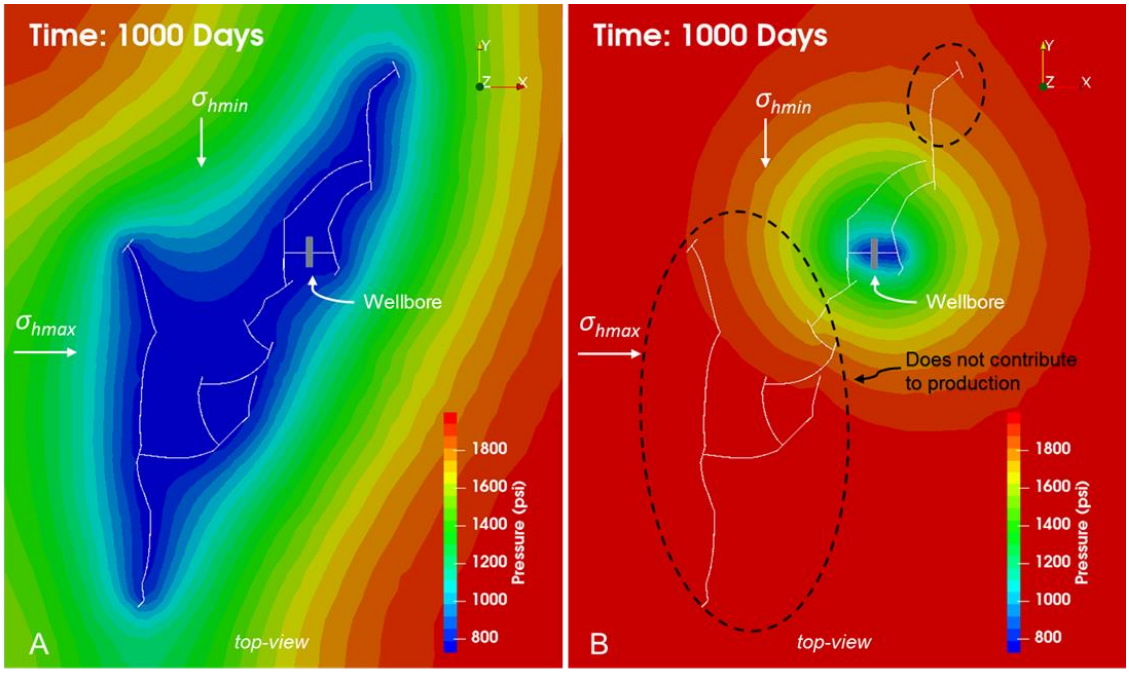

Figure 3.7: Reservoir pressure profile after 1000 days of production from a complex fracture network. Case A – No fracture closure and Case B – with fracture closure.

This study shows that the impact of fracture closure on production becomes even more pronounced in the case of complex fracture networks, with the actual production being nearly one-fourth of what is otherwise expected if fracture closure is ignored (Figure 3.8).

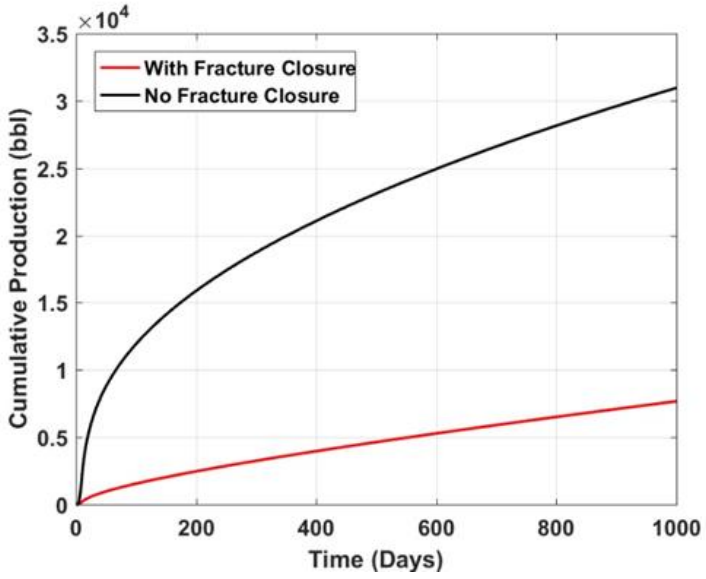

Figure 3.8: The impact of fracture closure is far more pronounced in the case of a complex fracture network, with production reduced to nearly 25% of what is otherwise expected in the absence of fracture closure.

3.3 IMPACT OF DRAWDOWN STRATEGY ON FRACTURE CLOSURE AND PRODUCTIVITY

In the previous section, we observed that the fracture closure can disconnect a significant fraction of the created fracture surface area from the wellbore. The drawdown pressure strategy directly affects the dynamic behavior of fracture closure. Three different drawdown management scenarios (Figure 3.9) were simulated. Well bottomhole pressure was ramped down linearly from the initial reservoir pressure (7200 psi) to a final constant pressure of 4200 psi in 10, 50, and 100 days.

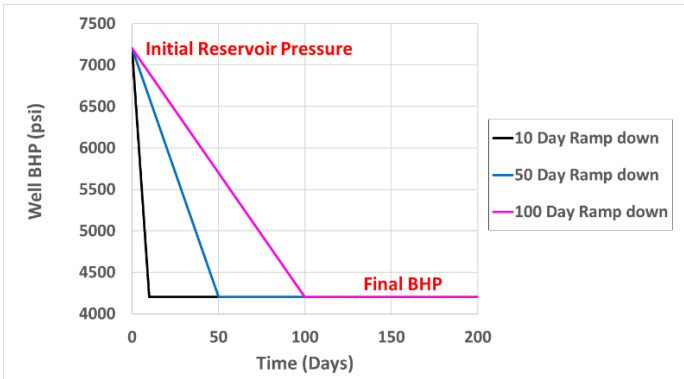

Figure 3.9: Three drawdown management strategy cases are investigated. 10-day BHP ramp down represents an aggressive strategy, and 100-day ramp down represents a conservative strategy.

The reservoir pore pressure profile after 1000 days of production is shown in Figure 3.10. In the case of an aggressive drawdown strategy (10 days BHP ramp down), the fracture segment in the upper layer has a lower contribution to the production as compared to the conservative drawdown cases. If we compare the case of 50-day ramp down with the 100-day ramp down, we observe that reservoir drainage efficiency is better in the case of the 50-day ramp down. In the case of 50-day drawdown management strategy, the drawdown pressure is high enough for production at a higher rate while maintaining fracture conductivity. However, in the case of a 100-day ramp down, the lower drawdown results in lower production rates even for a higher fracture conductivity. Based on this simple case study, we observe that we have two competing phenomena which can affect the productivity of a well. A decrease in bottomhole pressure leads to an increase in production rate, but at the same time, it can lead to an increase in effective stress on fracture resulting in a loss of fracture conductivity.

$$Production\ Rate\ \propto (P_{res} - P_{wf})$$

$$Fracture\ Closure\ \propto closure\ stress \propto (S_n - P_{wf})$$

If the choke is opened too quickly (aggressive drawdown strategy), the interconnected fracture network is likely to be disconnected early (fractures loose conductivity as fracture pressure declines). If the choke is opened too slowly (conservative drawdown strategy), not enough fluids will be produced before the fractures close (because of the small drawdown). The optimum drawdown strategy is one in which the fractures are allowed to remain conductive while maintaining a high enough drawdown to produce at a high rate. Production rate from a hydraulically fractured well depends on the connectivity of the fracture network with the wellbore. From this case study we observed that drawdown dependent closure of a fracture segment can lead to a decrease in the connectivity of the fracture system to the wellbore. This behavior is more pronounced in the case of complex fracture networks and is discussed in the next case study.

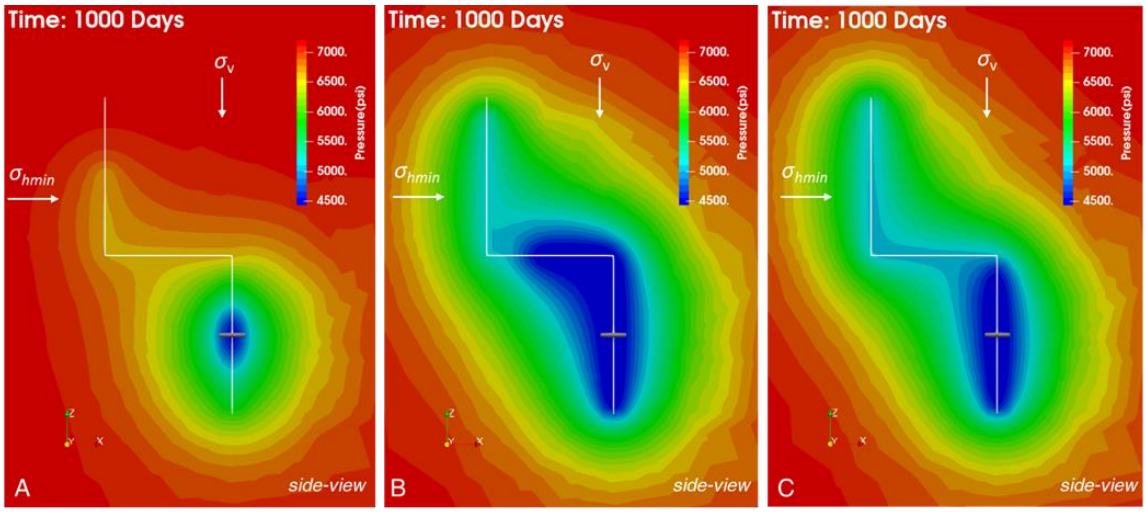

Figure 3.10: Reservoir drainage for three different drawdown management scenarios. (Case A:12 psi/hr, case B: 2.4 psi/hr, case C: 1.2 psi/hr).

3.4 IMPACT OF ROCK MINERALOGY ON THE OPTIMUM DRAWDOWN IN COMPLEX FRACTURES

We used a DDM based fracturing simulator (Shrivastava and Sharma, 2018a) to model fracture propagation from a fracturing stage having five clusters. In the presence of natural fractures, a complex fracture network is generated and is shown in Figure 3.11. For fracture closure modeling, we used the empirical exponential relationship (equation (3.1)) of stress-dependent fracture conductivity obtained from the experiments conducted by Wu et al. (2017). This fracture closure modeling approach is explained in detail in chapter-2 (section 2.2.3).

$$\frac{k}{k_0} = e^{-\gamma(\Delta\sigma_n)} \tag{3.1}$$

In experiments conducted by Wu et al., (2017), we observe that permeability modulus (γ) ranges from $1x10^{-7}$ to $3.2x10^{-7}$ Pa^{-1} depending on rock mineralogy. We also observed that the unpropped fracture conductivity decreases with increase in clay content of the rock. Permeability modulus (γ) is used as a proxy for clay content to analyze the impact of rock mineralogy while modeling unpropped fracture closure.

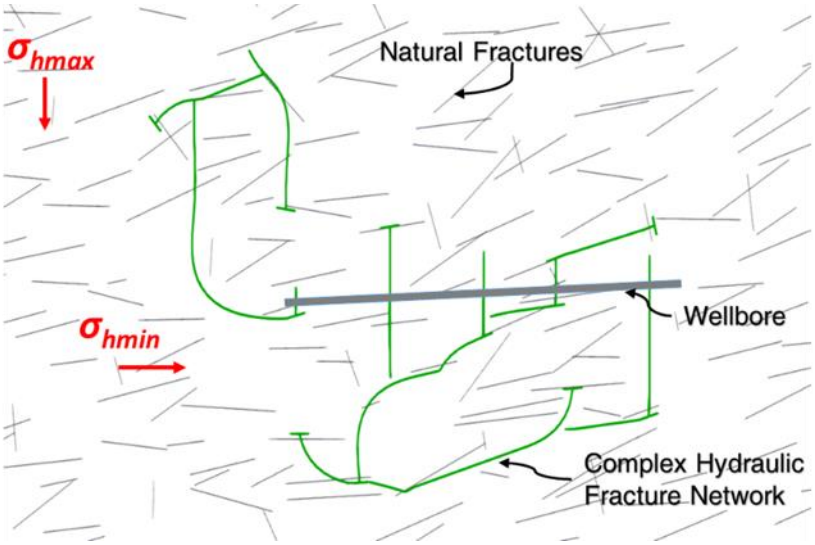

Figure 3.11: A stage scale complex fracture network generated due to the interaction of hydraulic fracture with natural fractures.

The generated fracture network geometry is used as an input for our geomechanical reservoir model for production simulations. Three different cases of permeability modulus (γ) were simulated to capture the sensitivity of closure stress on fracture conductivity and production. Simulation results (Figure 3.12) indicate that at higher values of γ, fracture conductivity is more sensitive to closure stress, and this leads to faster fracture closure. This loss in fracture conductivity is reflected in the reservoir drainage profile as shown in Figure 3.13. We observe that, with increasing fracture closure, the fractures away from the wellbore have a smaller contribution to the overall production.

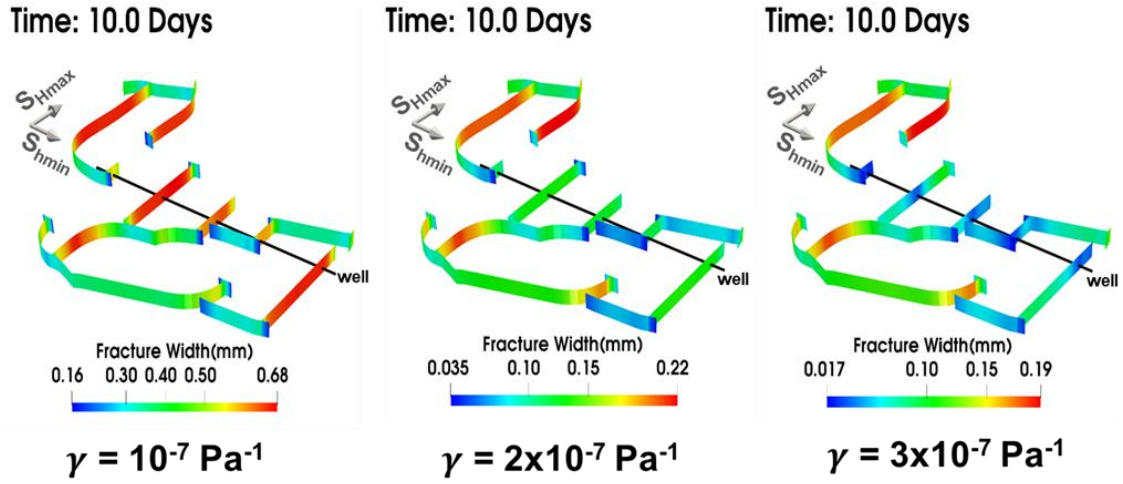

Figure 3.12: Fracture width profile after 10 days of production. Higher permeability modulus (γ) shows a significant loss in fracture conductivity.

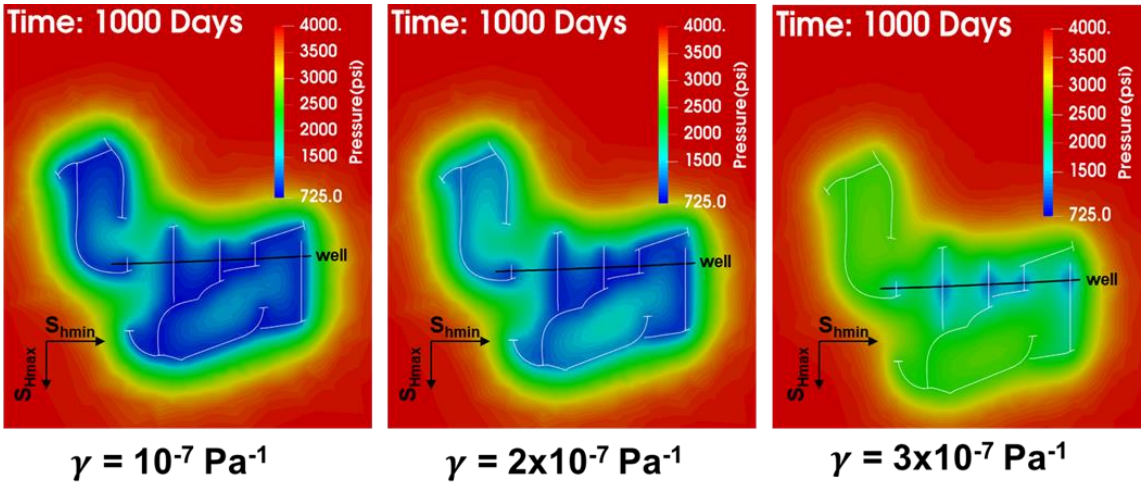

Figure 3.13: Reservoir drainage after 1000 days of production. For a lower permeability modulus (γ), the loss in fracture conductivity is lower which results in more uniform drainage around the fractures. At higher γ, fractures away from the wellbore contribute less to production due to fracture closure.

Next, we analyzed the impact of drawdown management strategy on production from this stage scale complex fracture network. Four different drawdown management strategies as shown in Figure 3.14 were investigated.

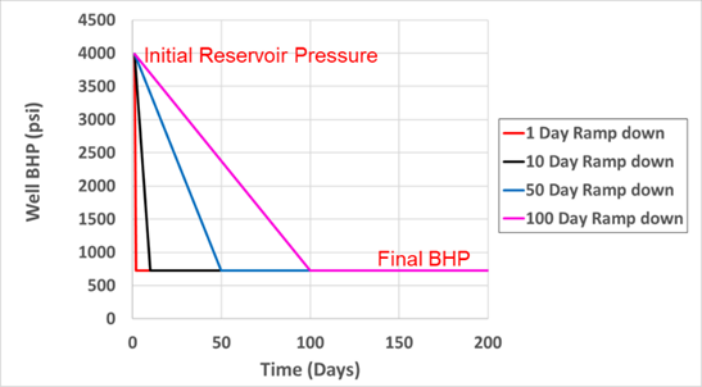

Figure 3.14: Different drawdown management strategies used in the simulation study. 1-day BHP ramp down represents an aggressive strategy, 100-day ramp down represents a conservative strategy.

The impact of drawdown management on productivity was analyzed for two different values of γ. Figure 3.15 shows the production rate and cumulative production for different drawdown management strategies when fracture conductivity has a high sensitivity towards stress (γ = 3x10^{-7} Pa^{-1}). From the rate vs. time plot, we observe that the rate initially increases due to a decreasing well bottomhole pressure and reaches a peak value. However, after the peak value, the rate starts declining even when the bottomhole pressure is decreasing. This decrease in well productivity can be explained by the loss in fracture connectivity due to fracture closure. Based on the cumulative production comparison, we observe that the conservative drawdown strategy is better when the fracture conductivity is more sensitive to stress.

A similar drawdown management sensitivity analysis was conducted when the fracture conductivity is less sensitive to stress (γ =10^{-7} Pa^{-1}), and the results are shown in Figure 3.16. At lower γ, loss in fracture conductivity is lower, so the rate decrease during decreasing well BHP is not observed in this case. Based on the cumulative production comparison, we observe that the aggressive drawdown strategy is better when the fracture conductivity is less sensitive to stress. As mentioned earlier, lower clay content rocks have lower γ and higher unpropped fracture conductivity. Due to a higher unpropped fracture conductivity of lower clay-content shales, an aggressive drawdown strategy may result in higher cumulative production.

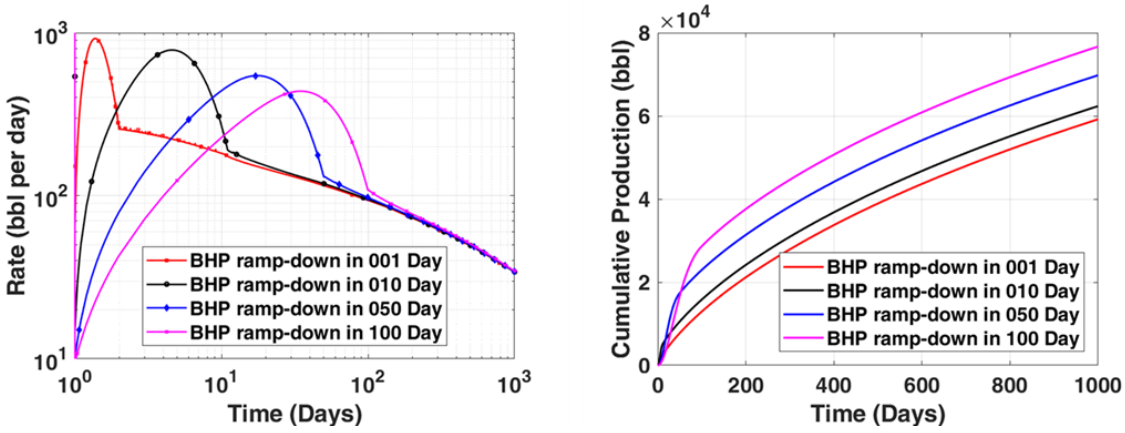

Figure 3.15: Impact of drawdown management on production when fracture conductivity has a high sensitivity to stress (γ = 3x10^{-7} Pa^{-1}, high clay content).

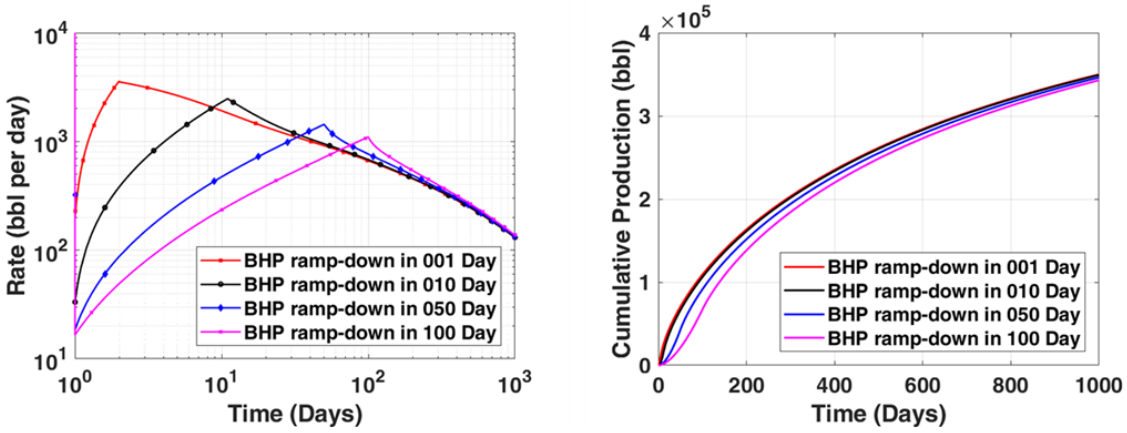

Figure 3.16: Impact of drawdown management on production when fracture conductivity has a low sensitivity to stress (γ = 10^{-7} Pa^{-1}, low clay content).

3.5 NPV MAXIMIZATION BASED OPTIMUM DRAWDOWN IN A 3-D COMPLEX FRACTURE NETWORK

Interaction of a hydraulic fracture with a natural fracture in 3-D is different than in 2-D due to stress relaxation and stress shadow effects (Shrivastava et al., 2018a). For a growing hydraulic fracture, higher stresses generated near the intersection of the hydraulic fracture and a natural fracture results in lower fracture width near the intersection region (Shrivastava and Sharma, 2018b). This lower width region can restrict the flow in the fracture network during production. A complex fracture network is generated by propagating a hydraulic fracture in the presence of natural fractures (Figure 3.17). The generated 3-D complex fracture geometry is used in the geomechanical reservoir simulator for productivity analysis. Figure 3.18 shows the reservoir drainage profile after 1000 days of production.

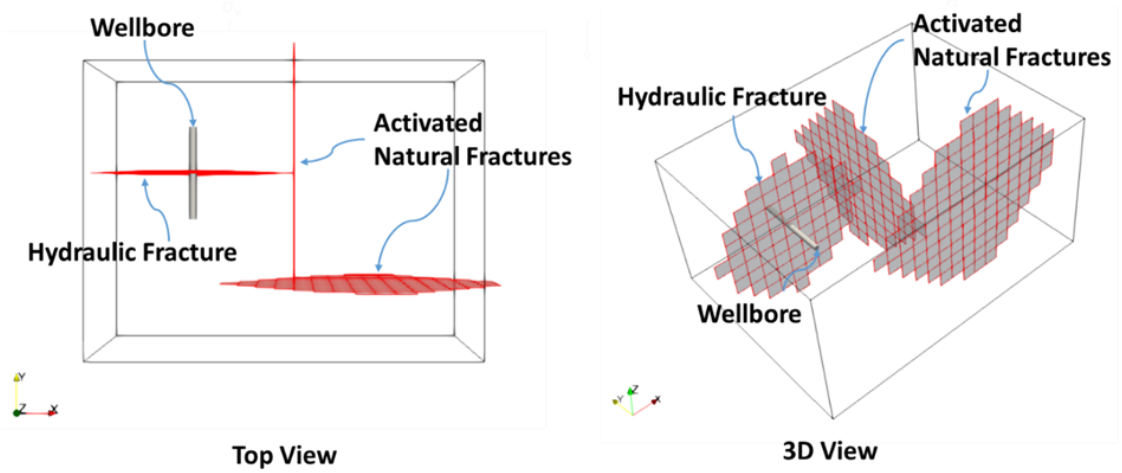

Figure 3.17: A three-dimensional complex fracture generated due to the interaction of hydraulic fracture with natural fractures.

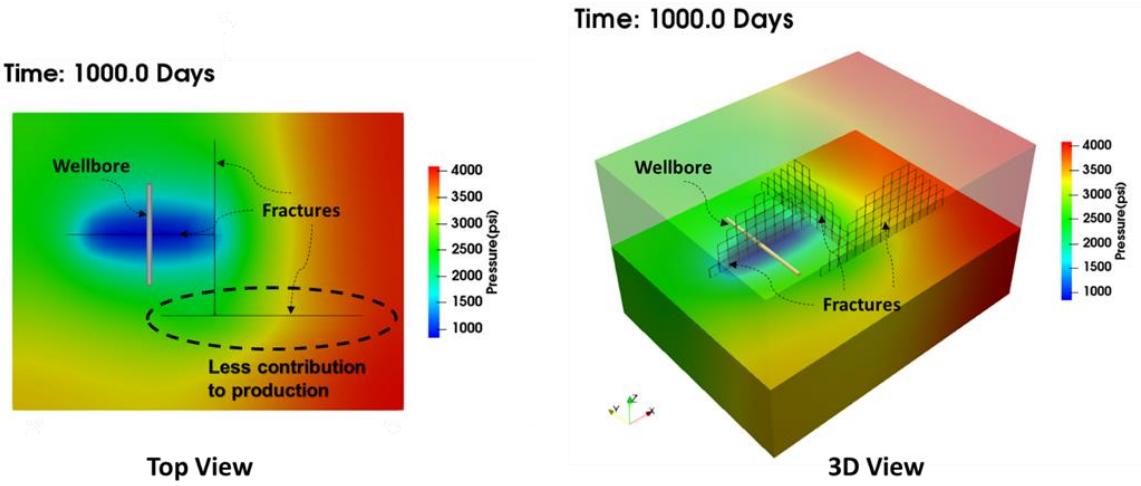

Figure 3.18: Reservoir drainage after 1000 days of production. Low fracture width near the intersection point leads to lower production contribution from the regions near activated natural fractures.

The lower fracture width near the intersection region acts as a bottleneck to production, and we observe a lower contribution to production from regions near activated

natural fractures. A conservative drawdown strategy can help in maintaining the conductivity of the intersection region for a longer time, but this leads to a lower initial production rate. Five different drawdown scenarios were simulated to find an optimum BHP decline rate based on NPV maximization.

Figure 3.19 shows the impact of the BHP-decline rate on production. We observe that an aggressive drawdown (5.4 psi/hr) results in a higher initial production rate but has a lower EUR due to loss of fracture connectivity to the wellbore. A conservative drawdown strategy (0.27 psi/hr) results in a higher EUR but has a lower initial production rate. These observations suggest the possibility of an optimum BHP decline rate based on NPV maximization. We calculated the NPV using production rates (Figure 3.19), typical well cost (3.5 MMUSD), oil price (60 USD/bbl), and discount rate (10 %). Based on the NPV vs. BHP decline rate plot (Figure 3.20), an optimum drawdown rate was obtained (0.91 psi/hr). This case study clearly highlights the impact of drawdown rate on production from a 3-D complex fracture network and the need for optimizing drawdown strategies in complex fracture networks to maximize NPV. It should be pointed out that the need to optimize drawdown is a concern irrespective of the details of the complex fracture network.

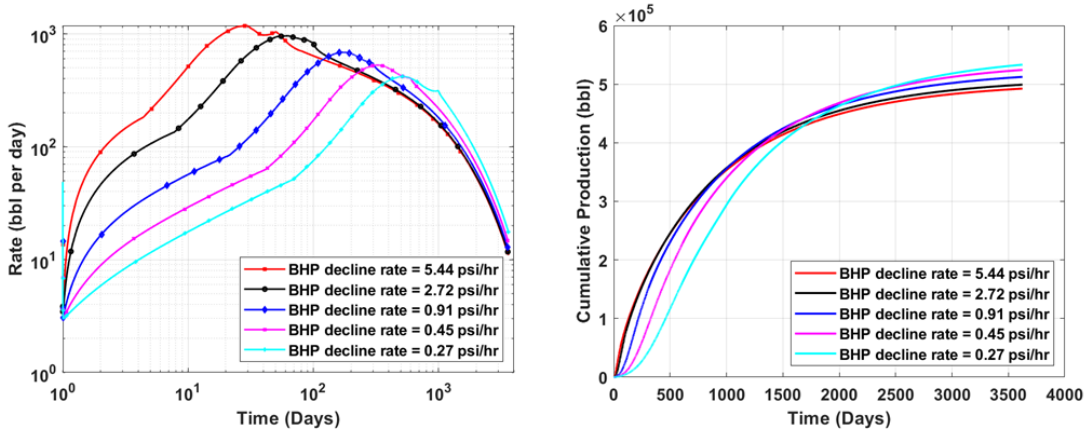

Figure 3.19: Impact of drawdown strategy on production rate and cumulative production.

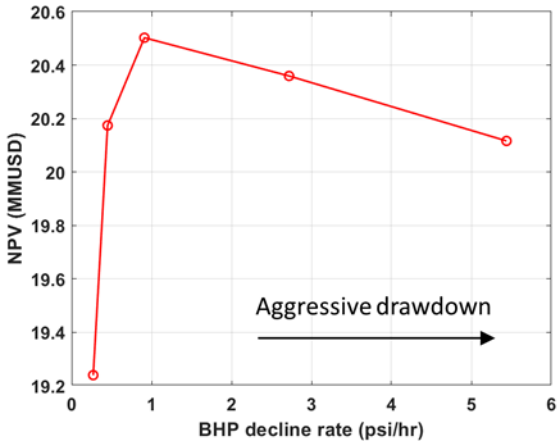

Figure 3.20: NPV vs. BHP decline rate suggests an optimum drawdown strategy

3.6 CONCLUSIONS

Production practices such as drawdown pressure management can affect the economics of unconventional reservoirs. In this chapter, we analyzed the impact of drawdown pressure management on fracture connectivity in complex fracture networks and well productivity. A fully coupled geomechanical reservoir simulator (described in chapter 2) was used to simulate production from complex fracture networks. The following conclusions can be drawn from this chapter:

- Fracture closure can disconnect a large fraction of fracture surface area from the wellbore. Fracture closure modeling is important while analyzing production performance for wells with complex fracture networks.

- An aggressive drawdown strategy leads to higher cumulative production when fracture conductivity is less sensitive to stress (rocks with smaller clay content).
- A conservative drawdown strategy leads to higher cumulative production when the fracture conductivity is more sensitive to stress (rocks with higher clay content).
- The smaller width region at the intersection of fractures (smaller width caused by stress shadow) acts as a bottleneck for the flow in the fracture network during production. Improper drawdown practices can lead to an early closure of these fracture connections which can affect well productivity.
- The competing phenomena of higher initial production rate and faster fracture closure during production suggest an optimum drawdown strategy based on NPV maximization.

Chapter 4: Effective Permeability Estimation for Complex Fracture Networks

Production from naturally and hydraulically fractured reservoirs depends on the geometry of the created fracture network. It is computationally expensive to model the mechanics and flow of each individual fracture in a large domain with thousands of fractures. In addition, due to limited geologic characterization, it is not possible to specify the location of all these fractures. In this chapter, we present a workflow to convert a discrete fracture network (DFN) into an effective permeability tensor that can be used to simulate flow in such complicated fracture networks.

We propose a workflow which includes the coupled effect of geomechanics and reservoir flow on the estimation of the effective permeability tensor for the stimulated reservoir volume (SRV). The workflow presented in this chapter provides a novel method to generate the reactivated natural fracture network around propagating hydraulic fractures and then capture the behavior of complex fracture networks in simplified reservoir simulation models using an effective permeability tensor for the SRV.

4.1 INTRODUCTION

Stress perturbations caused by hydraulic fracture propagation can lead to shear failure of natural fractures far away from the hydraulic fractures (Agrawal et al., 2019). These shear slippage events are registered as microseismic events. In the case of highly fractured reservoirs such as the Barnett, a very complex pattern of microseismic events is

---

This chapter is adapted from paper URTeC-2019-1083 (Kumar, A., Shrivastava, K., Manchanda R., and Sharma, M.M., 2019. "An Efficient Method for Modeling Discrete Fracture Networks in Geomechanical Reservoir." In Unconventional Resources Technology Conference). In this paper, Kumar developed the workflow for effective permeability estimation, designed and performed the simulations, and documented the results.

observed (Fisher et al., 2002; Cipolla and Wallace, 2014). To capture the impact of this complex stimulation behavior on production and well performance in a simplified model, the concept of "Stimulated Reservoir Volume" (SRV) was introduced by Warpinski et al., (2005). This SRV concept enabled traditional reservoir simulation models to use SRV as a proxy for complex fracture networks to mimic the actual production behavior observed in the field (Mayerhofer et al., 2010). However, often the SRV parameters are used as calibration parameters in history matching and are disassociated from the fracture modeling. This type of workflow can mimic the early production trends but can lead to erroneous predictions of well performance (Cipolla and Wallace, 2014). In this chapter, we present a novel workflow which considers the impact of fracture propagation on natural fracture failure that results in the creation of the SRV.

4.2 WORKFLOW FOR EFFECTIVE PERMEABILITY ESTIMATION

In this proposed workflow we calculate the effective permeability of the SRV in three main steps as shown in Figure 4.1. First, we model hydraulic fracture propagation in a naturally fractured reservoir. In the second step, the created fracture network is used in a reservoir simulation model to calculate production rates. These rates are matched in the third step by simulating the production in an effective model containing SRV. In the next section we provide a description of the models used in each step.

4.2.1 Model Description

We used a fully coupled three-dimensional hydraulic fracturing simulator (Multi-Frac-NF) (Shrivastava and Sharma, 2018) based on the displacement discontinuity method (DDM) to model fracture propagation in a naturally fractured reservoir. In this model, a hydraulic fracture is defined as an explicit discontinuity in an infinite linear elastic medium

having three displacement discontinuities in x, y, and z-direction. The relationship between displacement discontinuities and the net pressure is modeled as per 3D-DDM formulation (Crouch et al., 1983 and Shou et al., 1993). Fracture propagation direction is calculated using stress intensity factors (Sheibani and Olson, 2013) and maximum circumferential stress criterion (Erdogan and Sih, 1963).

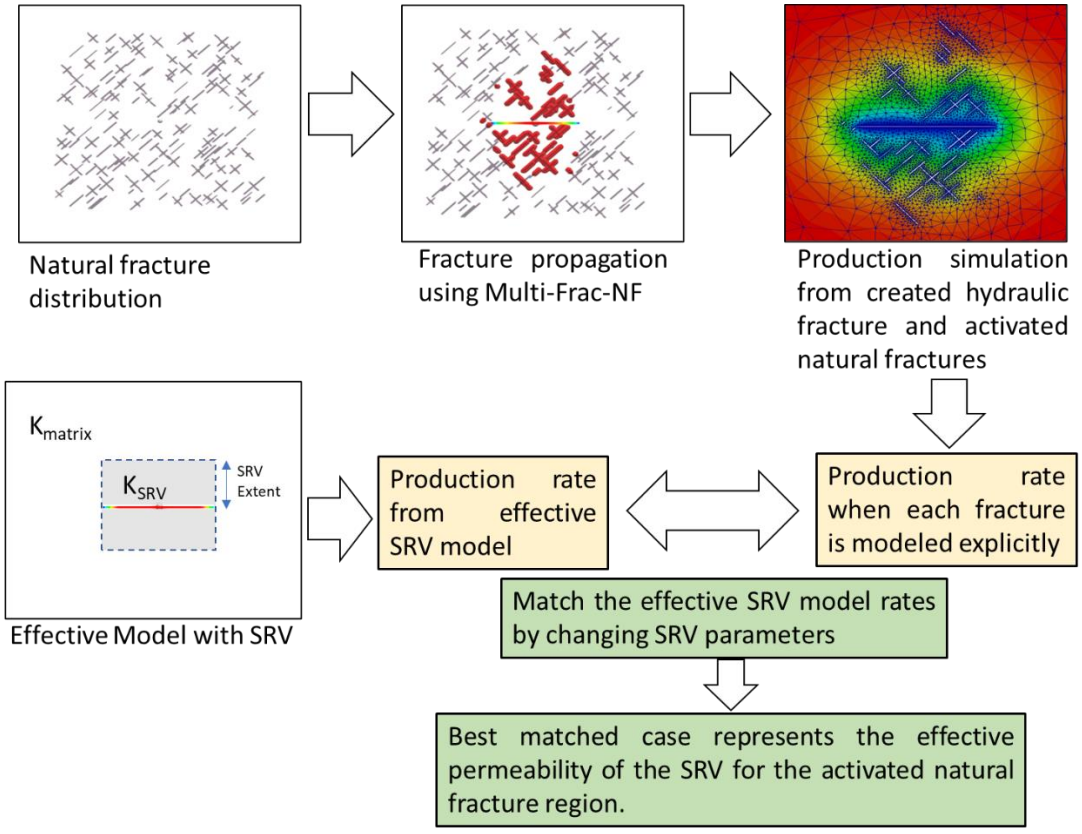

Figure 4.1: Proposed methodology to calculate effective permeability of the SRV.

A propagating hydraulic fracture can intersect a natural fracture. In the case of intersection, the stresses at the critical distance from the fracture are calculated based on Wu and Olson (2014). Mohr-Coulomb criterion is used to predict the failure of a natural

fracture. A failed natural fracture element is treated as a DDM element while solving geomechanics.

Disconnected natural fractures which are far away from the propagating hydraulic fracture can also slip due to stress perturbations during fracturing (Shrivastava et al., 2018a; Agrawal et al., 2019). These types of shear slippage are recorded as microseismic events. These failed natural fractures can be classified as induced unpropped (IU) fractures (Sharma and Manchanda, 2015). Flowback analysis and tracer data also show the evidence of the existence of these IU fractures (Manchanda et al., 2014). To model such fractures, shear stress and normal stress are calculated at each natural fracture plane to predict shear failure as per the Mohr-Coulomb criterion. The information of the locations and conductivity of the connected hydraulic fracture network and the disconnected failed natural fractures is input into to our geomechanics coupled reservoir simulation model to simulate production.

In our reservoir simulation model, geomechanics coupled fluid flow is solved in both the reservoir and the fracture domain. An unstructured reservoir mesh is created around the fracture network obtained from the Multi-Frac-NF fracturing simulation. Fracture mesh is created by identifying the fracture faces in the reservoir mesh. Reservoir flow is solved using the finite-volume method, and flow in the fracture is solved using the finite-area method. Our geomechanics coupled reservoir simulation model is described in detail in chapter 2.

To calculate the effective permeability of the SRV, we match the production rates from the rigorous fracture network simulation model to the production from an equivalent SRV simulation model production rates. We use the simulated annealing algorithms coupled with a genetic algorithm from Zhang et al., (2019) and Shiriyev (2018) to match

the production rates. A simulated annealing algorithm randomly generates the new set of model parameters, and the new model parameter search is derivative-free, which helps in finding the global minimum of the production matching objective function. We use SRV extent and SRV permeability tensor (K_{xx}, K_{yy}, K_{xy}) as the calibration parameters while matching the production. Best matched case parameters are used to calculate the principal component and direction of SRV permeability tensor.

Effective permeability of the SRV can change with the change in in-situ stress changes due to production. Permeability modulus (γ) can define the impact of stress on effective permeability of the SRV as explained in equation (2.10). Permeability modulus (γ) can be used as an additional calibration parameter during effective permeability calculation workflow to estimate stress dependent SRV parameters.

4.3 APPLICATION OF THE WORKFLOW

We used the workflow we have developed to analyze the impact of natural fracture azimuth on the effective SRV extent and the SRV permeability tensor. We also analyzed the impact of the propagating fracture height on the extent of shear failure.

4.3.1 Case description

Hydraulic fracturing simulation cases were set up in a naturally fractured reservoir. Figure 4.2 shows the perspective view and top view of the simulation setup.

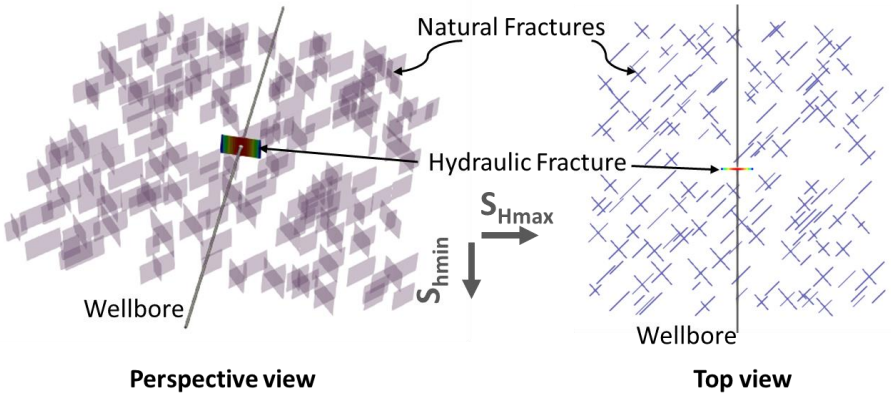

Figure 4.2: Simulation setup for hydraulic fracture propagation in a naturally fractured reservoir

Natural fractures were populated stochastically, and a normal distribution of natural fracture length was used. For simplification, we did not include any natural fracture intersecting with the propagating hydraulic fracture to avoid the formation of a complex fracture network. A planar hydraulic fracture is propagated, and shear failure of each natural fracture was checked at all time steps. Important simulation parameters are shown in Table 4.1.

Table 4.1: Reservoir and stimulation parameters for fracturing and production simulations.

Property	**Value**	**Units**
S_{hmin}	5000	psi
S_{Hmax}	5250	psi
Reservoir Pressure	4300	psi
Reservoir Permeability	500	nD

Injection Rate	5	bbl/min
Total Injection Time	60	Minutes
Production Pressure	1000	psi

4.3.2 Impact of natural fracture orientation on SRV

To understand the impact of natural fracture orientation on the SRV creation, we simulated six fracture propagation scenarios by varying the natural fracture azimuth from 15 degrees to 90 degrees (measured counterclockwise from the S_{Hmax} direction). The location and length of the natural fractures were kept the same for all the cases, and only orientation was varied. Figure 4.3 and Figure 4.4 show the top view and perspective view of the simulation results at the end of the fracturing treatment. Red dots in the figure show the shear failure events. We observed no shear failure when natural fractures are oriented at a low angle from the propagating fracture (15^0 and 30^0). An increase in shear failure is observed when natural fracture azimuth increased from 45^0 to 60^0.

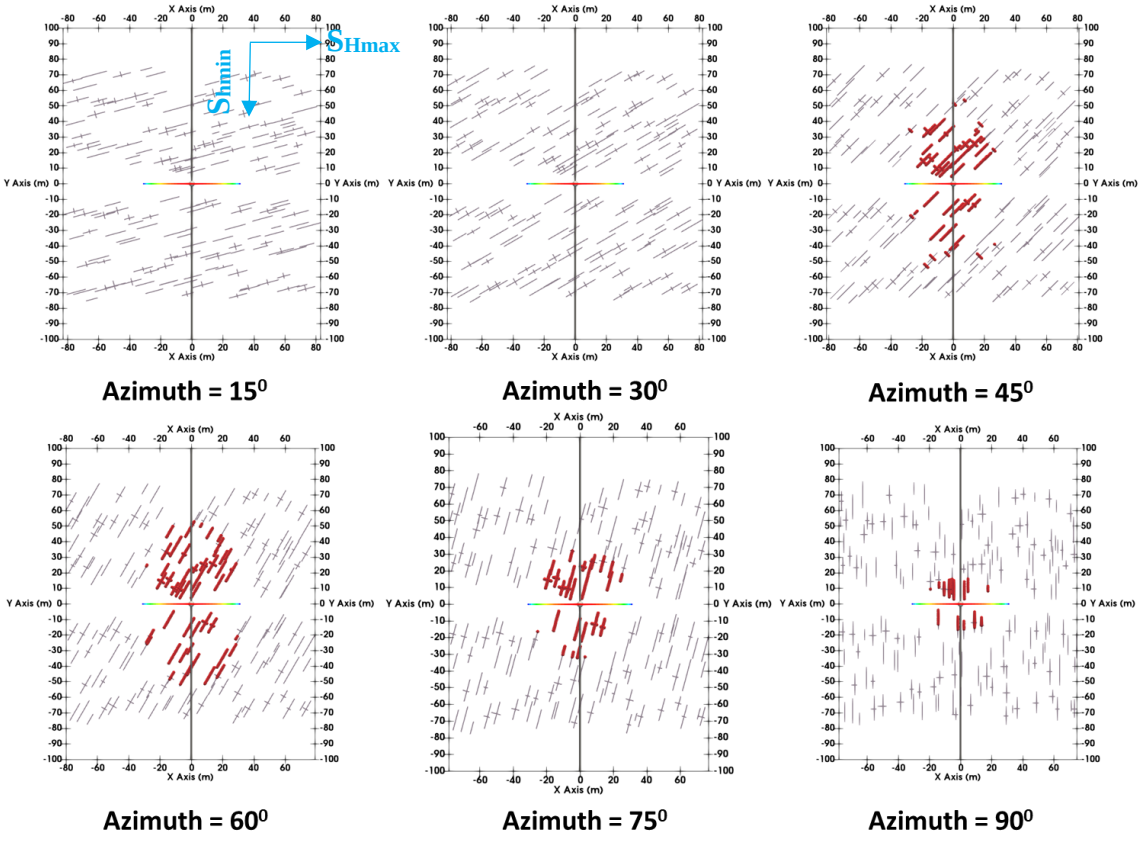

Figure 4.3: Effect of natural fracture azimuth (measured counterclockwise from the S_{Hmax} direction) on the extent of shear failure (top view). The hydraulic fracture was propagated from the origin, and red dots show the failed natural fracture elements.

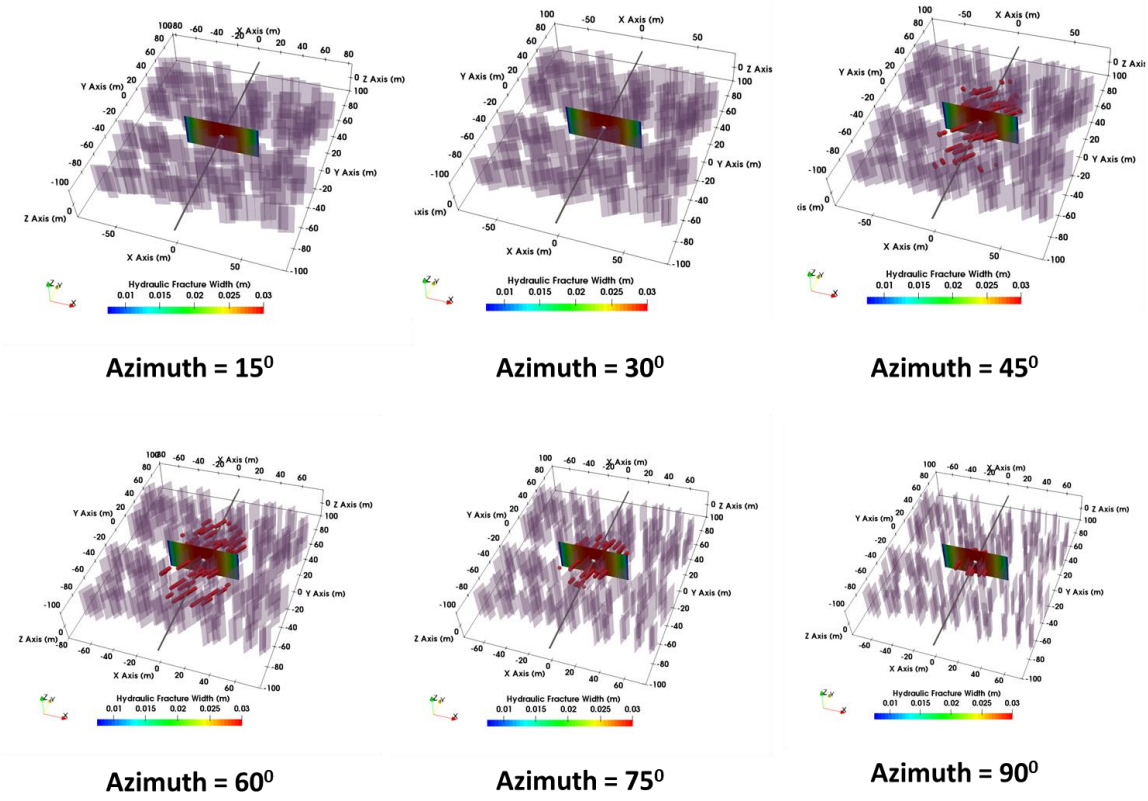

Figure 4.4: Effect of natural fracture orientation on the extent of shear failure (perspective view). The hydraulic fracture was propagated from the origin, and red dots show the failed natural fracture elements.

The hydraulic fracture geometry and the failed natural fracture information from the fracture modeling simulations are used to create reservoir mesh (Figure 4.5) for production simulations. In this approach, we model each fracture explicitly as in a "discrete fracture network (DFN)" model. DFN reservoir mesh is used in our finite-volume and finite-area based reservoir simulation model for the production analysis.

Figure 4.6 shows the reservoir pressure profile after 800 days of production for different natural fracture orientation. We observe the increase in the drainage area due to increase in the extent of SRV. Figure 4.7 shows the comparison of the production rate and

cumulative production for different natural fracture orientation cases. The initial production rate is same for all the cases because SRV is disconnected from the main hydraulic fracture. Once the depletion pressure front reaches the activated natural fractures, the rate decline slope is reduced due to the production contribution from the SRV. We observe an increase in the rate decline slope once the whole SRV region is depleted. The highest cumulative production is observed in the case of 60^0 natural fracture orientation due to the large extent of the SRV. It is important to note that this natural fracture azimuth of maximum SRV extent is highly dependent on the in-situ stress contrast, stress shadow induced by propagating fracture, friction angle of natural fractures, and elastic properties of the rock.

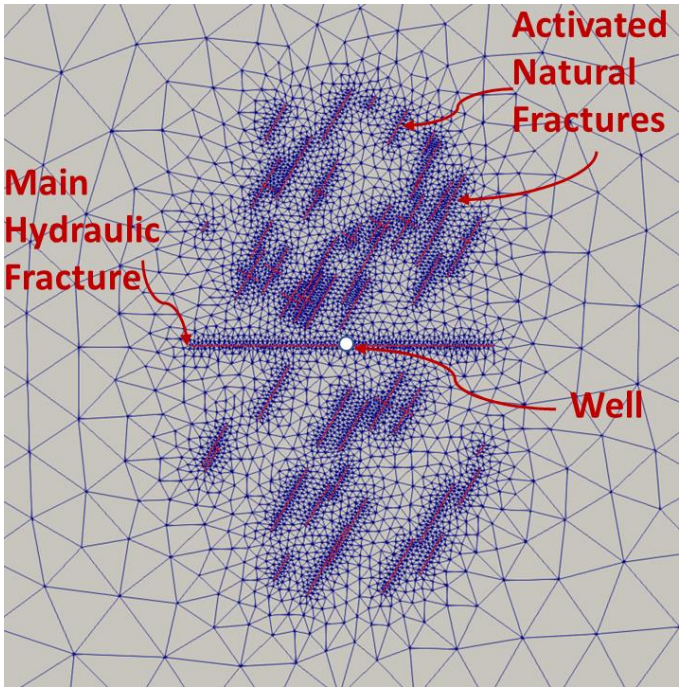

Figure 4.5: DFN simulation set up for production analysis. Reservoir mesh is created around the fracture network obtained from fracturing simulation results.

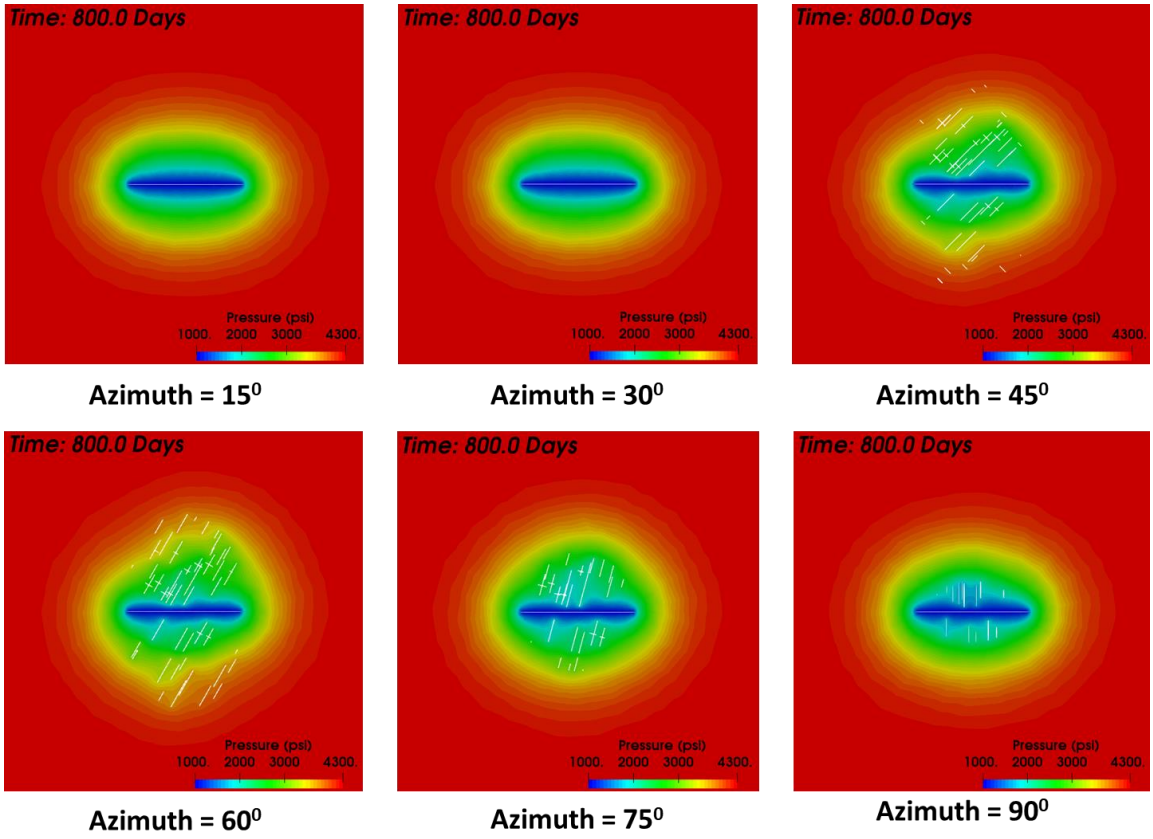

Figure 4.6: Pressure profile in the reservoir after 800 days of production (Top view). Activated natural fractures are shown as white lines. Maximum drainage area is observed in the case of 60^0 natural fracture orientation due to the largest extent of SRV.

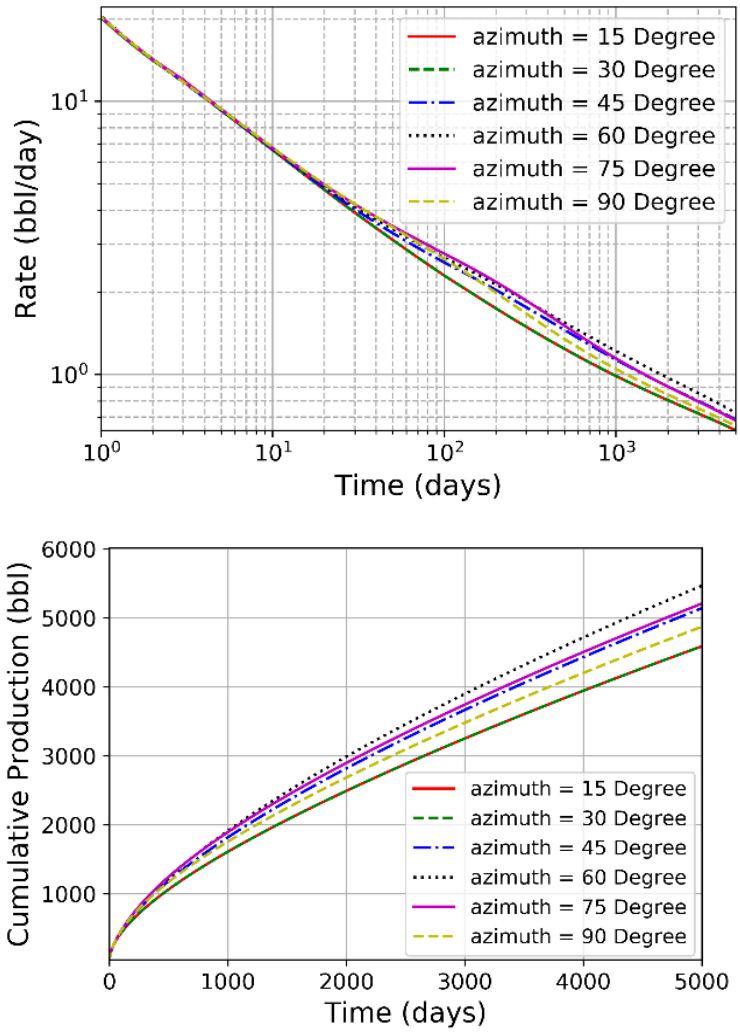

Figure 4.7: Effect of azimuth on production rates and cumulative production.

After analyzing the production form full DFN simulations, we calculated the effective permeability of the SRV. A complicated DFN model can be simplified as an effective model containing an SRV around the main hydraulic fracture as shown in Figure 4.8.

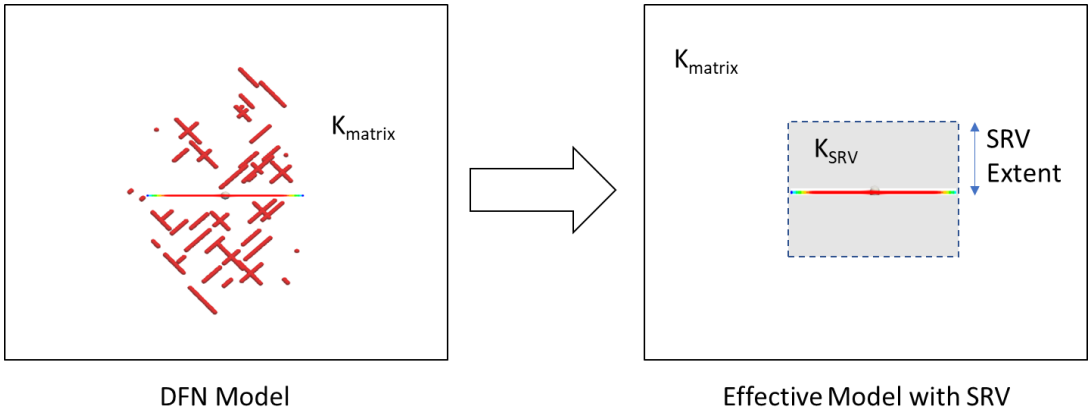

Figure 4.8: Complicated DFN model is simplified to an effective model having an SRV around the main hydraulic fracture.

SRV extent bounds were obtained from the shear failure map in fracturing simulation results. In real field situations, microseismic data could be used to bound the SRV extent for the production matching simulations. SRV extent and SRV permeability (K_{xx}, K_{yy}, K_{xy}) were used as calibration parameters to obtain similar production rates as it was observed in the DFN model production simulations. Figure 4.9 shows the production rate and cumulative comparison for the DFN model and the best-matched case. Best matched SRV permeability components (K_{xx}, K_{yy}, K_{xy}) were used to calculate the principal direction and value of the permeability in the principal direction as shown below.

$$\begin{bmatrix} K_{xx} & K_{xy} \\ K_{xy} & K_{yy} \end{bmatrix} \Leftrightarrow \begin{bmatrix} k_1 & 0 \\ 0 & k_2 \end{bmatrix}$$

Table 4.2 summarizes the estimated SRV parameters for all azimuth cases. Figure 4.10 shows the calculated SRV extent and SRV permeability tensor for different natural fracture orientation.

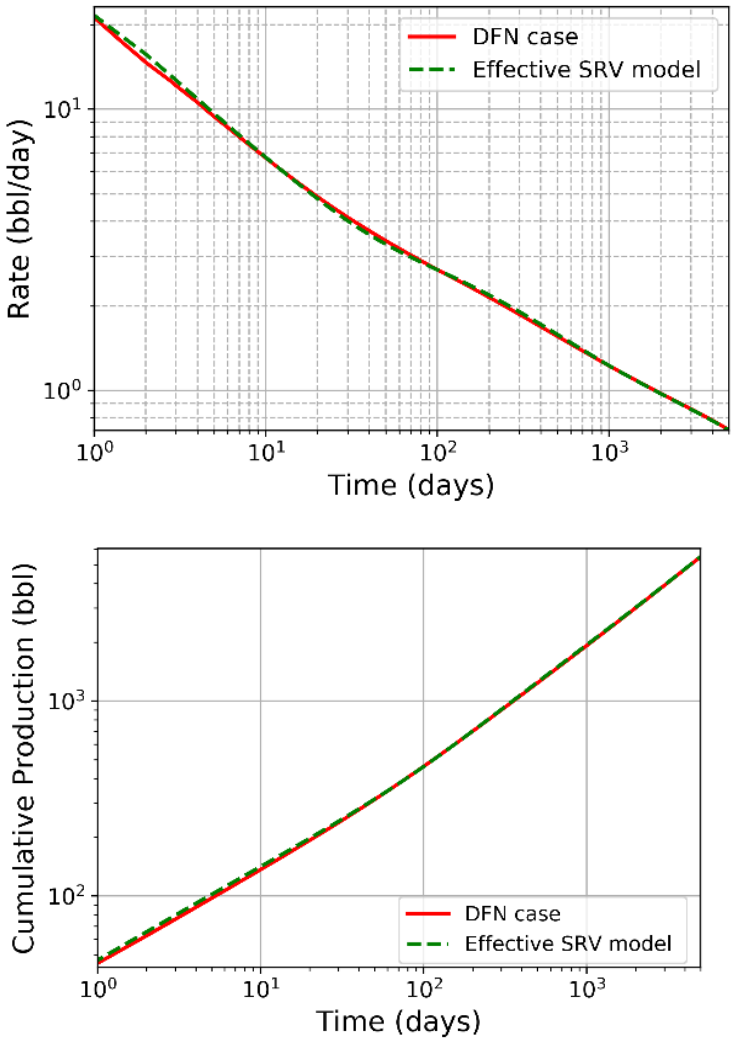

Figure 4.9: Production rate and cumulative production for the best matched case (Natural fracture azimuth = 60^0)

Table 4.2: Estimated SRV parameters for different natural fracture orientation

Natural fracture azimuth	**SRV extent (m)**	**K_{xx} (nD)**	**K_{yy} (nD)**	**K_{xy} (nD)**
15^0	0	500	500	0
30^0	0	500	500	0

45^0	31	4466	1666	2375
60^0	42	6543	2584	3642
75^0	14	3050	2127	2225
90^0	4	2924	1972	2159

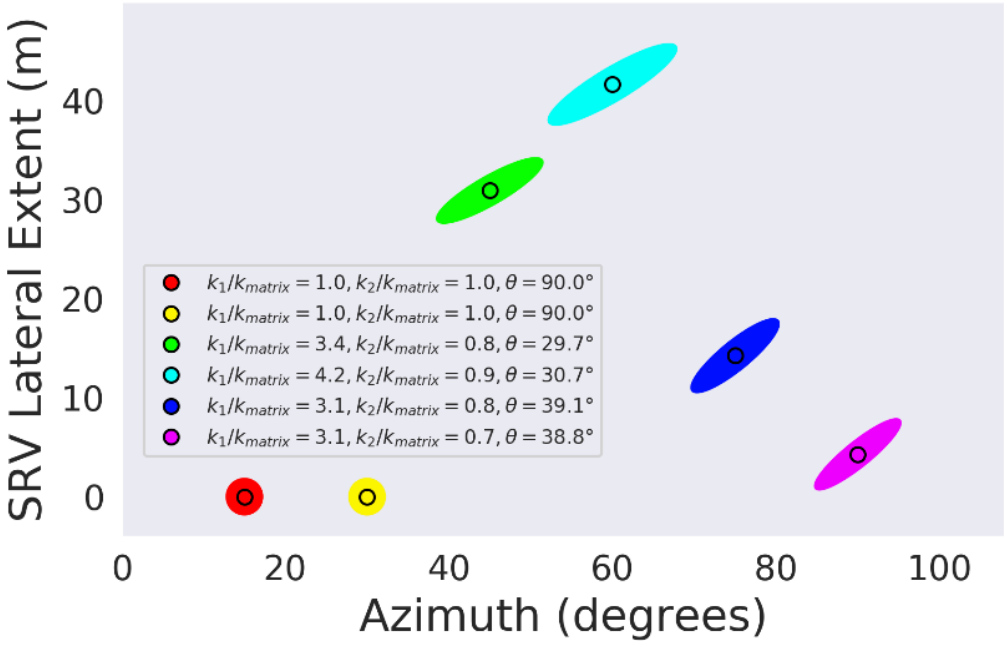

Figure 4.10: SRV lateral extent and effective permeability of SRV for different natural fracture orientation. θ is the principal direction of the permeability tensor. k_1 and k_2 are the principal direction permeability.

4.3.3 Impact of fracture height on SRV

We also analyzed the effect of fracture height on the SRV creation. Stress shadow created by a propagating fracture is proportional to the fracture height (Barree, 2015). We conducted four fracture propagation simulations by varying fracture height from 10 to 40 meters by changing the location of the stress barrier layers. The total volume of fluid

injected per unit fracture height was the same in all cases so that fracture length at the end of stimulation are similar. Figure 4.11 shows the top view of the simulation results at the end of the fracturing treatment. Red dots in the figure show the shear failure events. We observed that shear failure of natural fracture increases with an increase in fracture height. With an increase in fracture height, stress shadow increases and spreads further away from the main propagating fracture, and this leads to the SRV extent increase.

To calculate the effective permeability of the SRV, we followed a similar workflow as explained in the previous case of natural fracture azimuth sensitivity. Fracturing simulation results were exported to the reservoir simulation model for production simulations. Production matching was done to estimate the SRV extent and SRV permeability tensor and is shown in Figure 4.12.

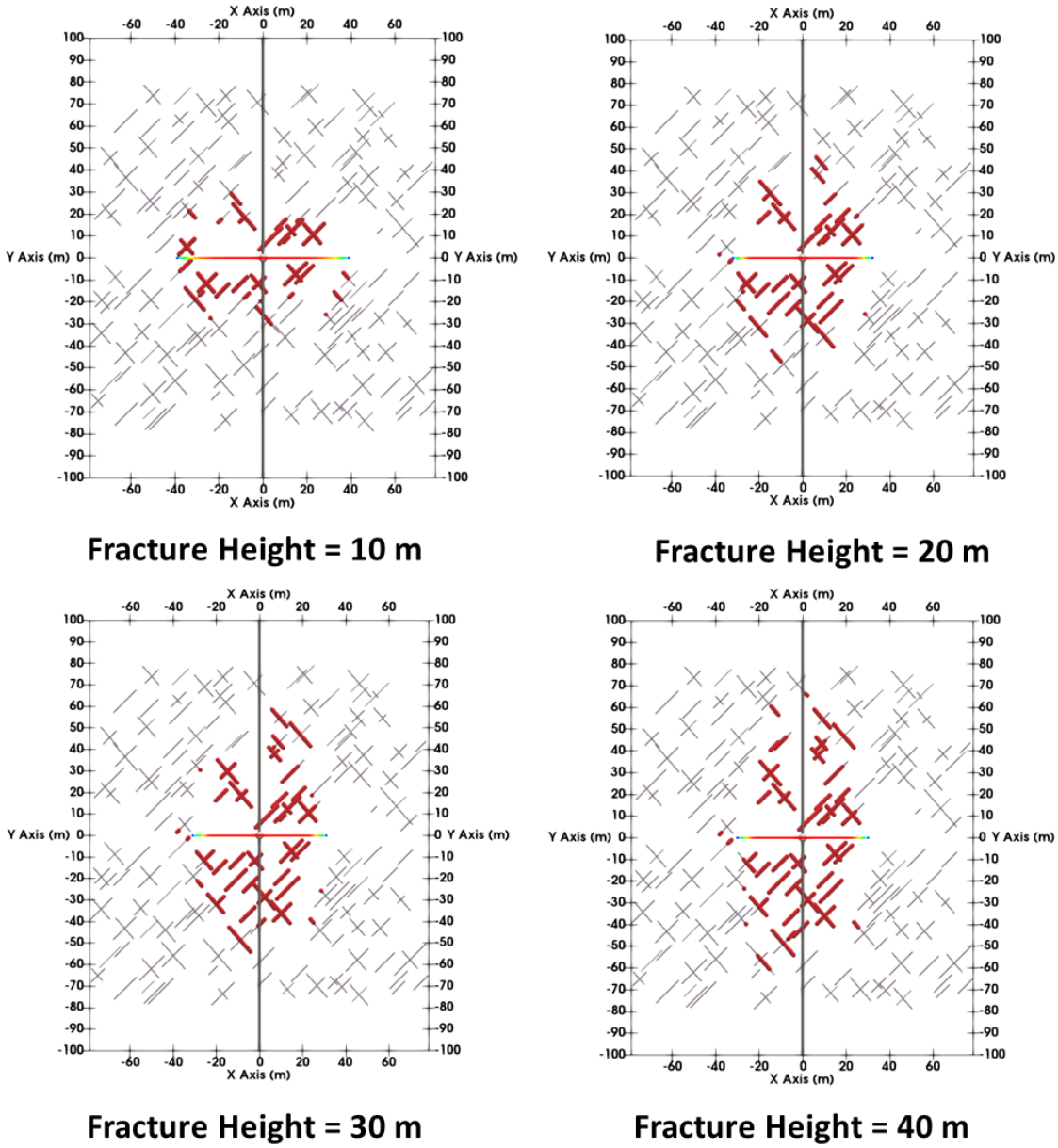

Figure 4.11: Effect of fracture height on the extent of shear failure (top view). The hydraulic fracture was propagated from the origin, and red dots show the failed natural fracture elements.

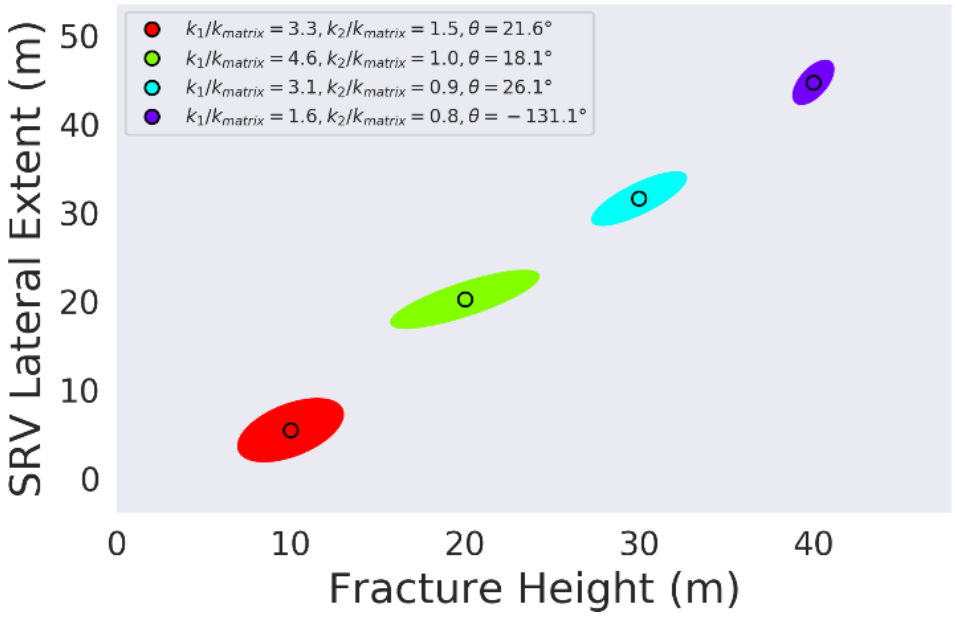

Figure 4.12: SRV lateral extent and effective permeability of SRV for different fracture height. θ is the principal direction of the permeability tensor. k_1 and k_2 are the principal components of the permeability tensor.

4.4 CONCLUSIONS

In this chapter, a workflow was presented to estimate the properties of the SRV created when hydraulic fractures propagate in naturally fractured reservoirs. The proposed workflow captures the effect of coupled geomechanics and reservoir flow. The important conclusions drawn from this chapter are as follows:

- When natural fractures are oriented at a low angle from the maximum horizontal stress direction, negligible shear failure of natural fractures is observed. Maximum shear slippage of natural fractures was observed at a 60^0 natural fracture azimuth. This angle of maximum shear slippage depends on the in-situ stress contrast and stress shadow induced by the propagating fracture.

- We analyzed the impact of disconnected failed natural fractures on the well productivity. We observed that the increase in the extent of shear failure leads to higher production contribution from the activated natural fractures. The production rate decline is smaller when production from these disconnected natural fractures starts. We observed an increase in the production rate decline once the whole region of activated natural fractures is depleted.
- An increase in fracture height leads to an increase in shear failure of natural fractures. Stress shadow induced by the propagating fracture increases with an increase in fracture height. This implies that the spatial extent of the SRV increases with an increase in the propagating fracture height.
- The extent of the SRV and the SRV permeability tensor was calculated to obtain an "effective" or surrogate model by matching the production of the effective model to the production from the rigorous DFN model. This calculated effective permeability of the SRV can be used in upscaled traditional reservoir simulation models.

Chapter 5: Effect of Parent Well Production on Child Well Stimulation and Productivity

Unconventional field development requires substantial capital costs. In the United States, land leases may expire after two to three years if they are not held-by-production (HBP). Operators typically start developing the field by drilling the minimum number of wells to hold the lease. These initially drilled wells are referred to as "parent wells (primary wells)". After holding the lease, operators may start full development of the field by drilling infill wells. These infill wells, if they are near the primary wells, are referred to as "child wells". As unconventional basins are maturing, more child wells are being drilled to meet increasing production targets. Miller et al. (2016) and Lindsay et al. (2018) have shown that over time, as basins are developed in the U.S., a greater number of child wells are being drilled as compared to the number of parent wells drilled.

Reduced production from child wells has been observed due to prior depletion around the parent well. In this chapter, a systematic simulation study is conducted to understand the effects of parent well depletion on child well fracture growth and overall production.

5.1 Introduction

Parent wells are stimulated in virgin reservoir pressure and stress conditions. Also, the spacing between parent wells is high enough such that drainage of one parent well does

This chapter is adapted from paper SPE-199700 (Kumar, A., Shrivastava, K., Elliott, B., and Sharma, M.M., 2020, "Effect of Parent Well Production on Child Well Stimulation and Productivity". In SPE Hydraulic Fracturing Technology Conference and Exhibition. Society of Petroleum Engineers.) In this paper, Kumar developed the workflow for the parent-child well interaction study, designed and performed the simulations, and documented the results.

not affect the stimulation of another parent well. Infill/child wells are drilled close to parent wells after a few years of production from parent wells. Reduced reservoir pressure due to parent well depletion alters the stresses in the reservoir (Roussel et al., 2013; Manchanda et al., 2017; Guo et al., 2018; Agrawal and Sharma, 2018). The reduced total stress region around the parent well fractures affects child well fracturing. A propagating child well fracture may grow asymmetrically and interact with fractures of an already producing parent well. In many cases, propagating child well fracture may intersect the parent well. This phenomenon is referred to as a "Frac Hit" (Jacobs, 2017). Evidence of such fracture interaction has been observed in several field diagnostics tests such as tracer tests (Wood et al., 2018; Kumar et al., 2018a), and pressure interference tests (Seth et al., 2018b; Seth et al., 2019).

The impact of parent-child well interaction on production can be positive or negative. Instances of both have been reported in the literature (Miller et al., 2016; King et al., 2017; Xu et al., 2019). Miller et al. (2016) analyzed the impact of parent-child interaction for different plays. They observed that in the Bakken and Haynesville, parent well production is likely to be positively affected when child wells are fractured. In the Woodford and Niobrara, child well fracturing shows a detrimental effect on the production from parent wells for most cases. They also showed that typically, child well production rates are lower than the parent wells across all formations. Xu et al. (2019) compared the production performance and effect of completion design (proppant loading, well spacing) in parent and child wells by different benches for the Permian Basin. They observed that the child wells drilled in recent years have in general more proppant and fluid loading with longer lateral length. This can be a limitation while making a recommendation based on the analysis of parent-child field data. They also observed that with an increase in well

spacing, the performance of a child well improves. Whitfield et al. (2018) analyzed the impact of infill well fractures on the parent well production as shown in Figure 5.1. They observed that the average reduction in the parent well production due to an infill well stimulation is around 40%.

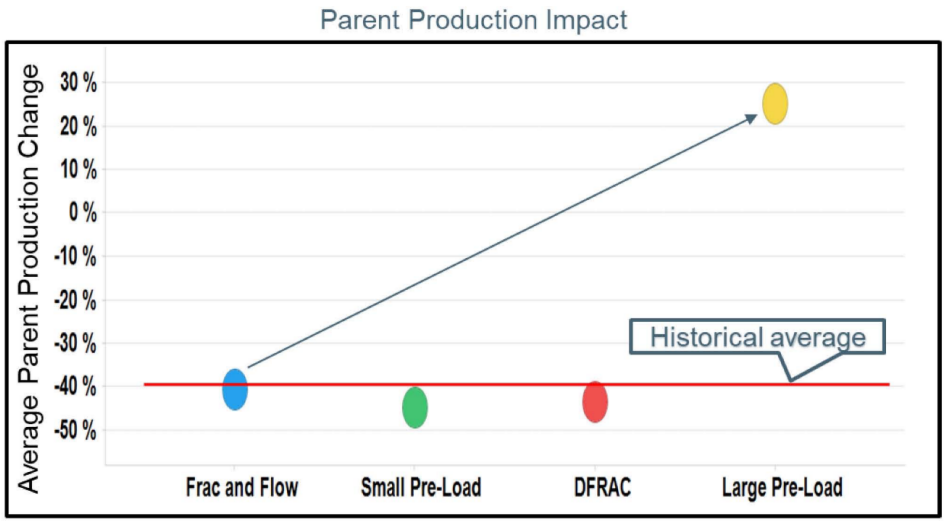

Figure 5.1: Impact of infill well drilling on parent well production (taken from Whitfield et al., 2018).

Well spacing, the extent of parent well depletion, and reservoir flow properties are the important parameters that affect the magnitude of the change in the stress and the propagation of hydraulic fractures from the child well. In this chapter, we investigate the impact of these parameters on the child well fracture growth and on overall production from parent and child well.

5.2 MODEL DESCRIPTION AND WORKFLOW

We developed a workflow to simulate parent-child well interactions by integrating a hydraulic fracturing simulator (Multi-Frac-NF) and the geomechanics coupled reservoir simulator as described in chapter 2.

Integrated simulation workflow for parent-child well interactions is developed as shown in Figure 5.2. Parent well fracturing is simulated in Multi-Frac-NF. Created hydraulic fracture information is used in the reservoir simulation model to obtain the pressure and stress profile in the reservoir after the parent well depletion.

Figure 5.2: Simulation workflow for parent-child well interaction study.

5.3 IMPACT OF RESERVOIR FLOW PROPERTIES AND INFILL TIMING ON CHILD WELL FRACTURE GROWTH

We analyzed the impact of reservoir flow properties (porosity, permeability, fluid viscosity, and total compressibility) and infill timing (parent well production duration before child well stimulation) on the child well fracture growth. The impact of child well production on parent well production is also analyzed. Important simulation parameters that are fixed for all cases are shown in Table 5.1. In our model, symmetric pressure depletion profile with respect to the fracture location in the reservoir (see Figure 5.3) is used for child fracture propagation. Hence, we do not expect/observe fracture turning for

single fracture scenarios. For the simulations, the fracturing fluid injection rate was scaled down as per grid size (5 m) in the fracture height direction, assuming the injection rate of 94 bbl/min for 5 clusters. The volume of fracturing fluid injected in all the cases is the same for both parent and child wells.

The reduced total stress region near the depleted parent well leads to asymmetric fracture propagation from the child well. We define fracture asymmetry as the ratio of the "difference between the fracture length towards the depleted region and the non-depleted region" to the "total fracture length" (Figure 5.3 and equation (2.13)). Asymmetry is zero when fracture length is equal on both sides of the child well. Asymmetry increases when child well fractures have preferential growth towards the depleted parent well.

Table 5.1: Important simulation parameters

Property	**Value**	**Units**
Initial S_{hmin}	5000	Psi
Initial S_{Hmax}	5354	Psi
Initial Reservoir Pressure	4300	Psi
Injection Rate	1.9	bbl/min/cluster/grid size
Total Injection Time	60	Minutes
Production Pressure (BHP)	1000	Psi

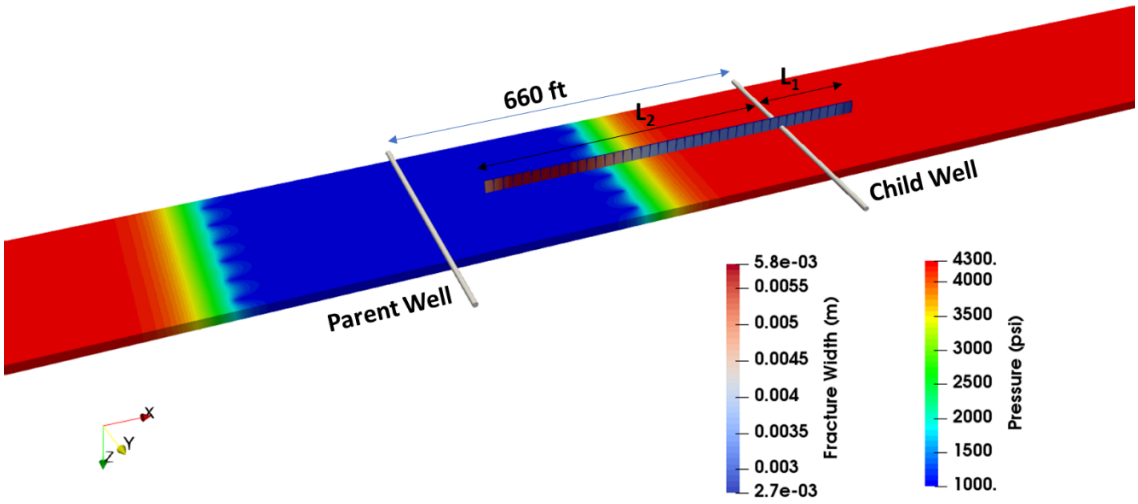

Figure 5.3: Asymmetric fracture propagation in child well due to depletion in parent well. Child well fracture is scaled vertically for visualization.

$$Asymmetry = \frac{(L_2 - L_1)}{(L_2 + L_1)} \tag{5.1}$$

We analyzed the impact of infill timing on the child well fracturing. Infill timing can be considered a proxy for the extent of depletion before child well fracturing. In our simulations, the parent well was produced at a constant bottom hole pressure of 1000 psi. Figure 5.4 shows the effect of infill timing on the child well fracture growth. With an increase in infill timing (parent well production duration before child well stimulation), the depletion pressure front moves more towards the child well. Hence, the child fracture encounters the depleted region earlier during its growth, and therefore the child well fracture asymmetry increases. Infill timing was varied from 0 to 36 months, and Figure 5.5 shows the impact of the infill timing on the child well fracture growth with the help of a bar chart. Bar lengths represent the ratio of the fracture length to the well spacing. The orange color shows the fracture growth towards the parent well, and the blue color shows

the fracture growth away from the parent well. We observed that when the infill timing is zero (the child well is fractured in virgin uniform reservoir pressure and stress conditions), symmetric fracture propagation is observed. As the extent of depletion is increased (increased infill timing), the child well fracture asymmetry increases. In Figure 5.5, we observe that asymmetry remains constant for infill timing 12 to 20 months (higher infill timing). This is due to the grid size effects in our simulation. We selected a grid size of 5 meters to run hundreds of field-scale simulations with tractable run-time. The results for higher asymmetry cases are close because of the low resolution in the fracture dimension due to the grid size.

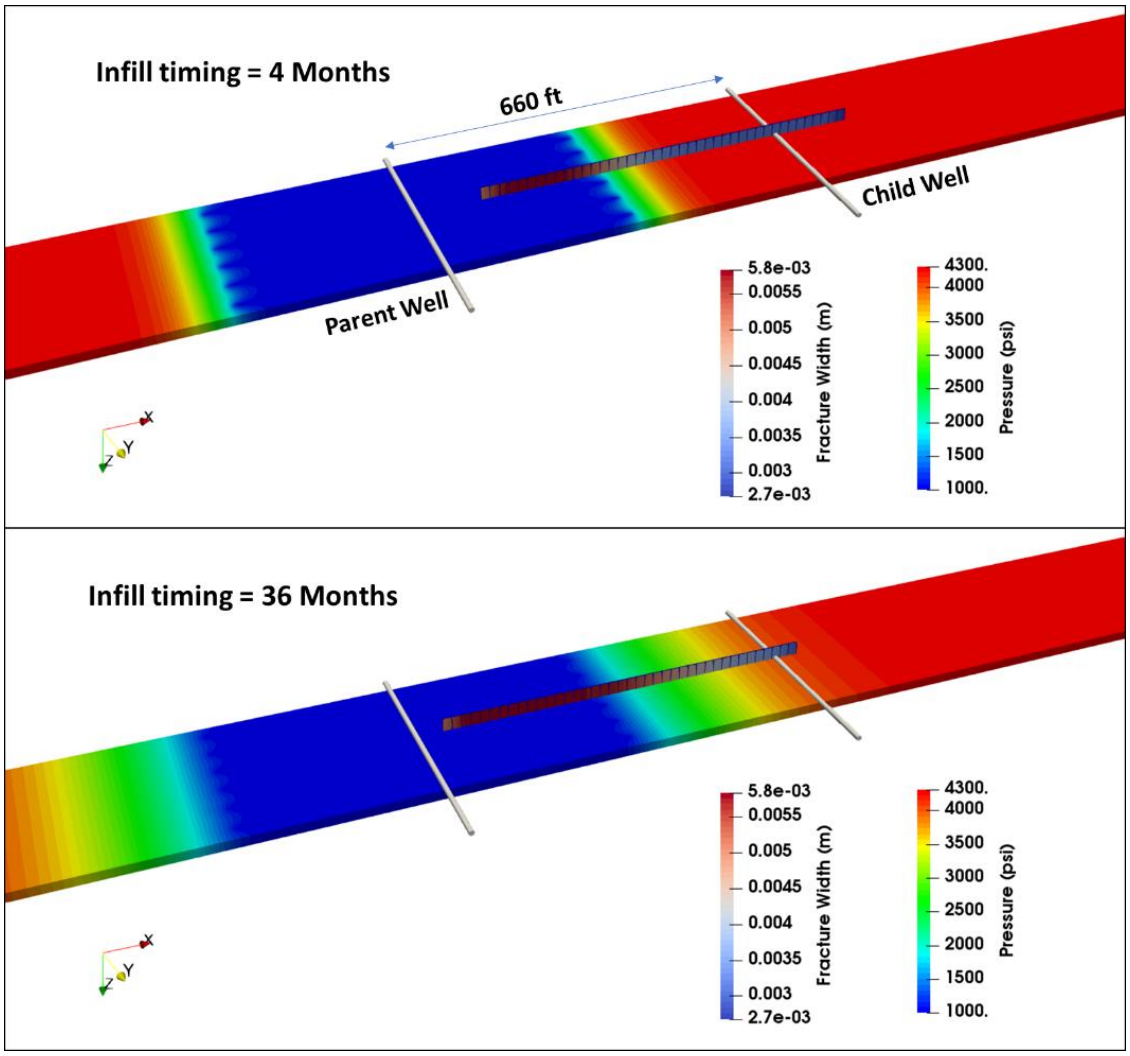

Figure 5.4: Impact of infill timing on child well fracture growth. Child well fracture is scaled vertically for visualization.

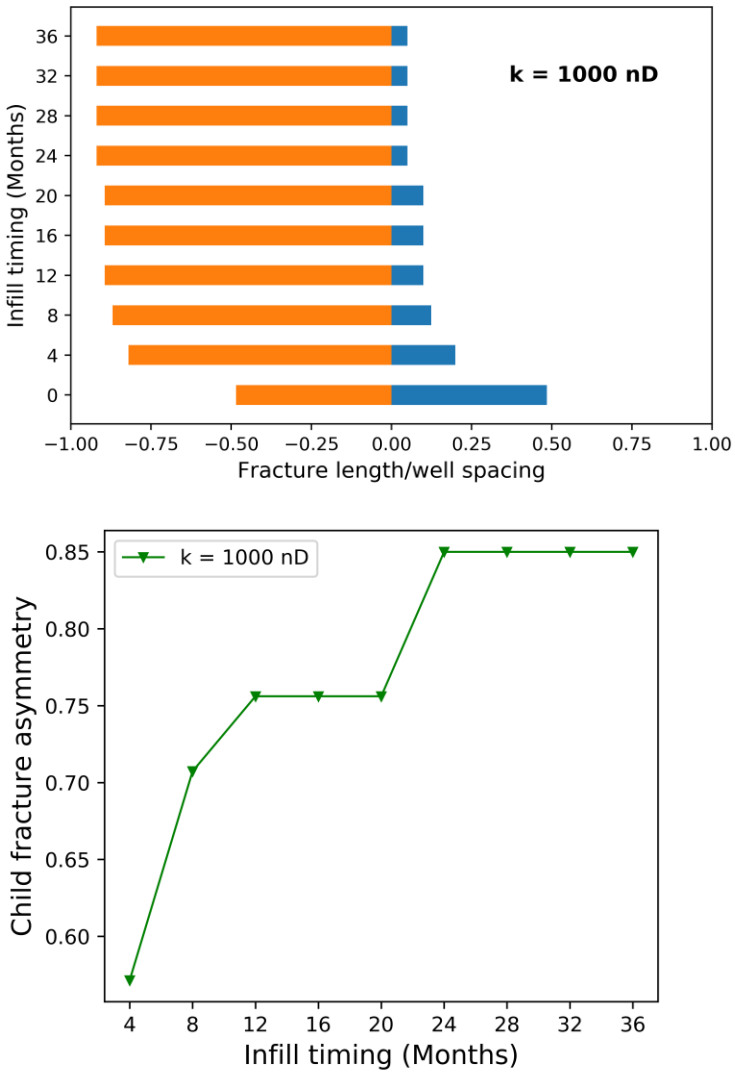

Figure 5.5: Impact of infill timing on the child well fracture growth

Next, we systematically analyzed the impact of reservoir permeability, porosity, viscosity, and total compressibility on the child well fracture asymmetry. Figure 5.6 and Figure 5.7 show the impact of reservoir permeability on the depletion pressure profile and the altered total stress after 850 days of production from the parent well. We observed that with an increase in reservoir permeability, parent well depletion pressure front extent

increases towards the child well (Figure 5.6). Due to the geomechanical coupling between pressure and stress, an increase in the reservoir permeability leads to a further decrease in the total stress around the child well (Figure 5.7). A much lower total stress due to an increase in the reservoir permeability leads to an increase in the child well fracture asymmetry as shown in Figure 5.8(a). Similarly, a decrease in porosity, reservoir fluid viscosity, and total compressibility leads to an increase in child well fracture asymmetry as shown in Figure 5.8 (b), (c), and (d). These flow properties can be combined as diffusivity $\left(\frac{k}{\phi\,\mu\,c_t}\right)$ which can be sufficient to describe the reservoir depletion. Several simulations were conducted at a fixed value of diffusivity but at different porosity, permeability, viscosity, and total compressibility. For these cases, child well fracture asymmetry was plotted as shown in Figure 5.9. We observed that asymmetry vs. infill timing curves for all cases collapse to a single curve when diffusivity is constant. Hence, diffusivity as a combined parameter helps in reducing the number of parameters in our analysis.

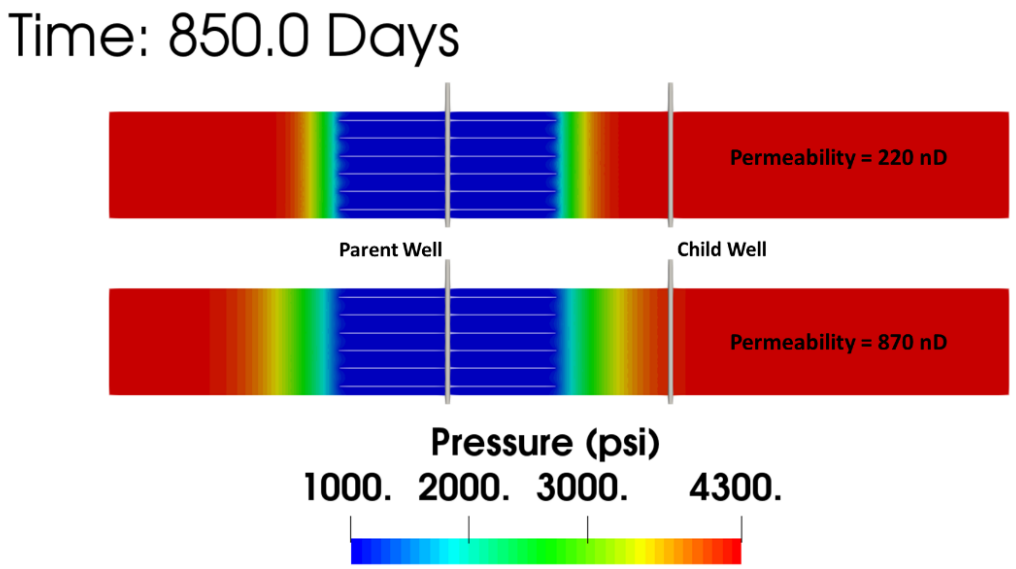

Figure 5.6: Effect of reservoir permeability on the depletion pressure front. With an increase in permeability, depletion pressure front extent increases towards the child well.

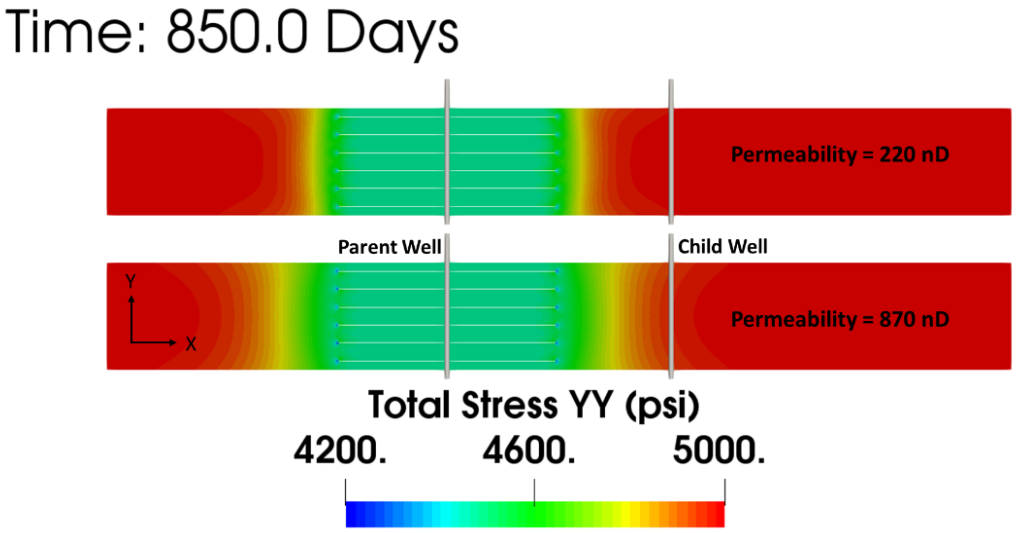

Figure 5.7: Effect of reservoir permeability on the total stress. With an increase in permeability, the total stress around the child well decreases.

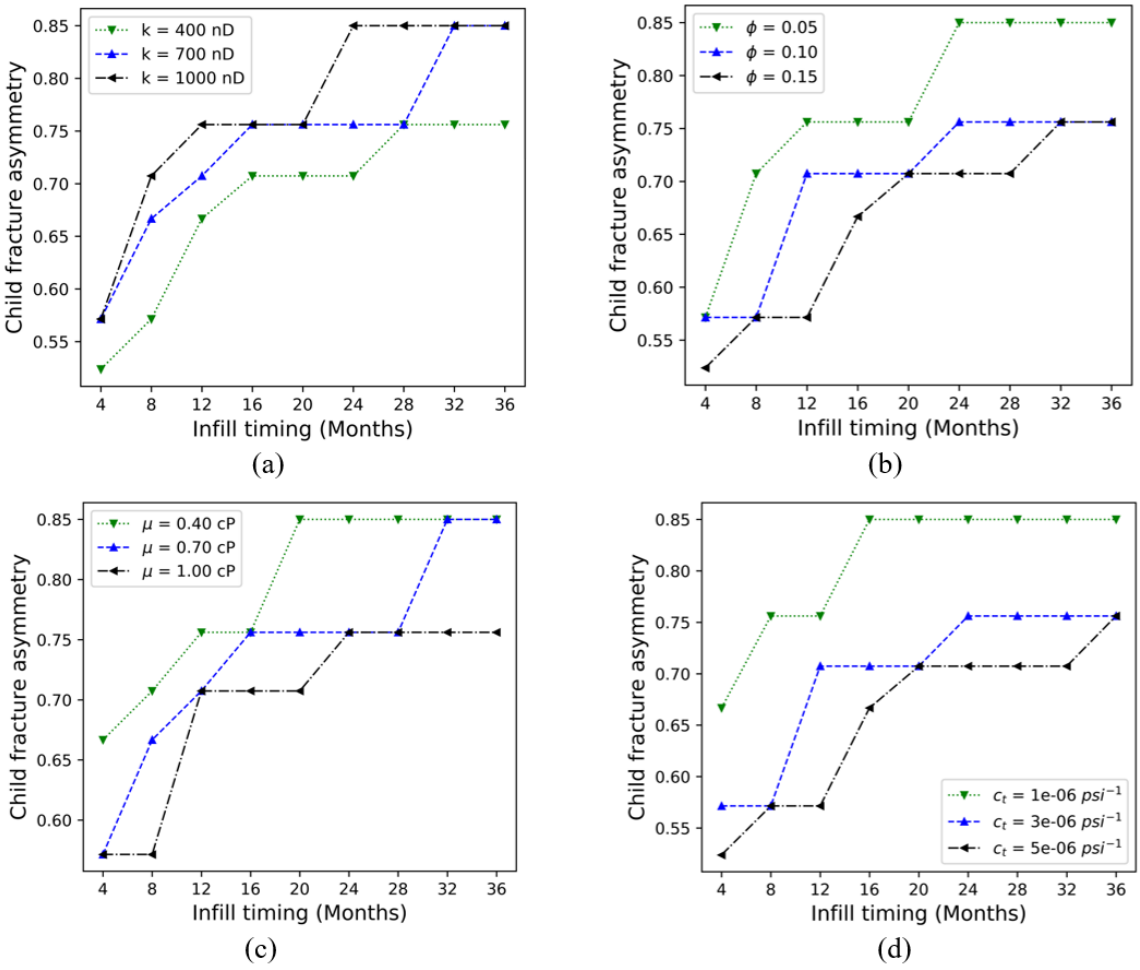

Figure 5.8: Impact of reservoir (a) permeability, (b) porosity, (c) viscosity, (d) total compressibility on child well fracture asymmetry

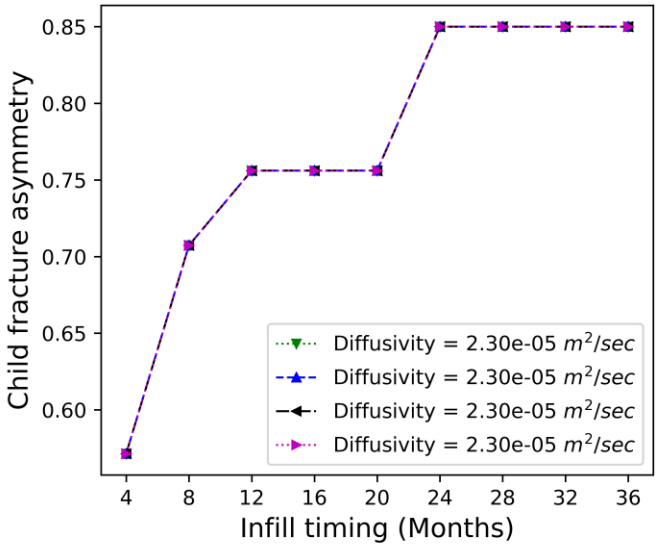

Figure 5.9: Combining the reservoir permeability, porosity, viscosity, and compressibility as diffusivity helps in reducing the number of parameters. Curves from all cases merge to a single curve when diffusivity is kept constant.

5.4 IMPACT OF DIFFUSIVITY AND INFILL TIMING ON CHILD WELL FRACTURE GROWTH

Figure 5.10 shows the impact of reservoir diffusivity, and infill timing on the child well fracture asymmetry. We varied the reservoir diffusivity to include typical values (taken from Meyer, 2013) for several formations. We observed that with an increase in reservoir diffusivity, the rate of the parent well depletion increases, which leads to an increase in child well fracture asymmetry. For a higher reservoir diffusivity, even a smaller infill timing leads to higher fracture asymmetry. At lower reservoir diffusivity, infill timing has a lower impact on fracture asymmetry. Production analysis for these cases is explained in the next section.

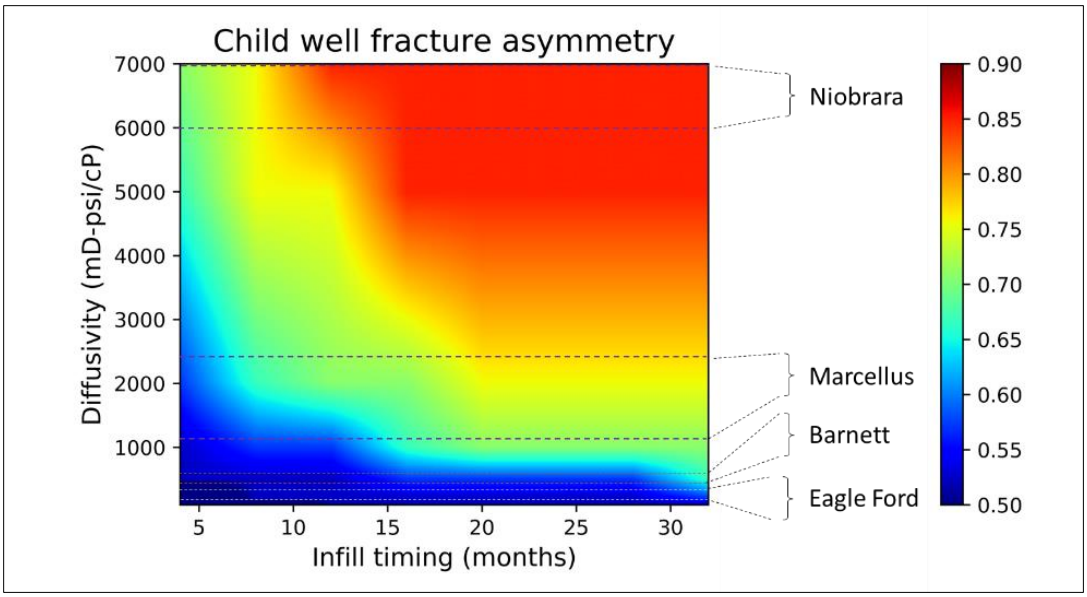

Figure 5.10: Impact of reservoir diffusivity and infill timing (extent of parent well depletion) on child well fracture asymmetry

5.5 IMPACT OF CHILD WELL FRACTURING ON PRODUCTION

We investigated the impact of fracture asymmetry on the production from parent and child well. The parent well was produced at 1000 psi bottom hole pressure before the child well was stimulated. After the child well stimulation, both parent and child well were produced at a constant bottom hole pressure of 1000 psi. Figure 5.11 shows the impact of the child well fracture asymmetry on the reservoir pressure profile after 2000 days of parent and child well production.

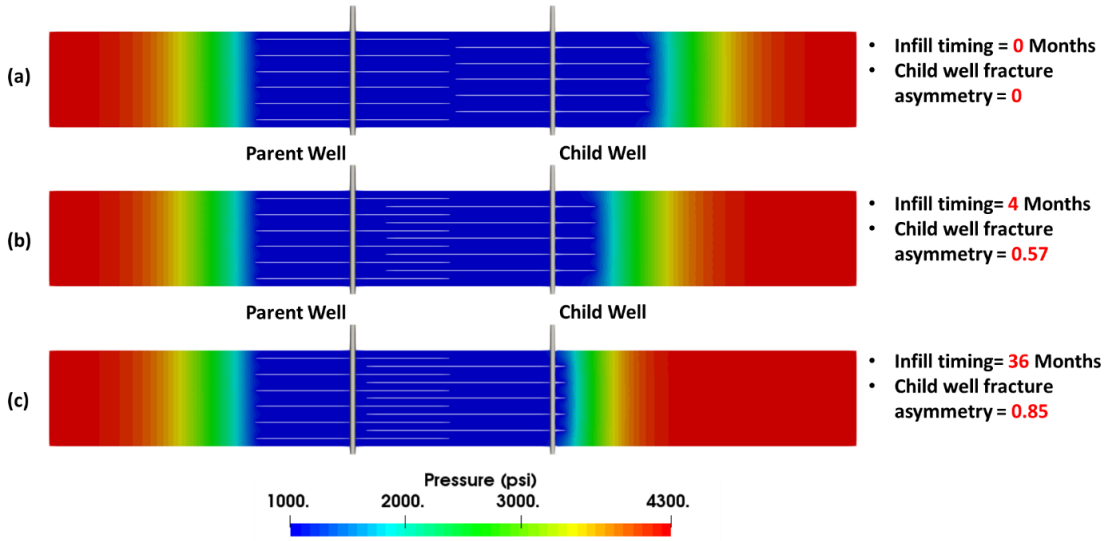

Figure 5.11: Impact of fracture asymmetry on the reservoir drainage. Drainage efficiency decreases with an increase in fracture asymmetry.

A zero-base case was simulated in which both parent and child well were fractured simultaneously (Figure 5.11-a). In this case, fracture asymmetry is zero; there is no overlap in the drainage area of the parent well and child well fractures, which leads to the maximum extent of the reservoir drainage area. Asymmetric fracture propagation caused by depletion in the parent well leads to an increase in the fracture area around the already depleted parent well. Since the volume of fracturing fluid injected is the same in all the cases, asymmetric fracture propagation leads to inefficient reservoir drainage as shown in Figure 5.11 (b) and (c). Cumulative production was normalized with respect to the zero-base case cumulative production (Equation (5.2)). Figure 5.12 shows that the cumulative production decreases as the child well fracture asymmetry increases.

$$Normalized\ production = \frac{Cumulative\ production\ in\ asymmetric\ fracture\ case}{Cumulative\ production\ in\ symmetric\ fracture\ case\ (base\ case)} \quad (5.2)$$

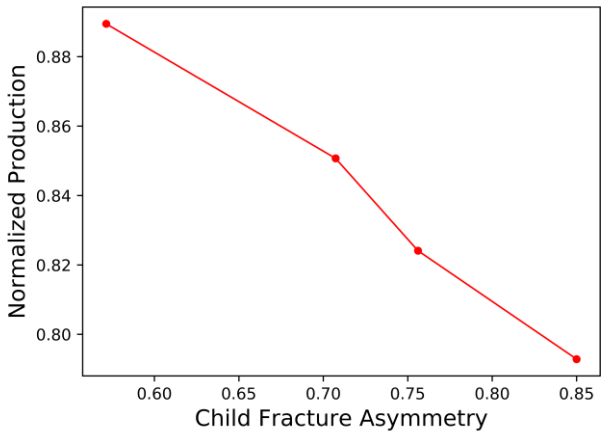

Figure 5.12: Impact of child fracture asymmetry on cumulative production. Cumulative production decreases with an increase in fracture asymmetry.

Next, we analyzed the total (parent + child) production for all diffusivity and infill timing cases (Figure 5.13). We calculated the percentage reduction in the total cumulative production from the zero-base case (symmetric fractures due to simultaneous parent and child well stimulation) to account for the production loss due to parent-child well interactions. We observe that for higher reservoir diffusivity, even a smaller infill timing can lead to higher production loss. For lower reservoir diffusivity, infill timing has a smaller impact on the total production. This type of plot can help an operator optimize the timing of infill drilling to reduce fracture asymmetry and maximize cumulative production.

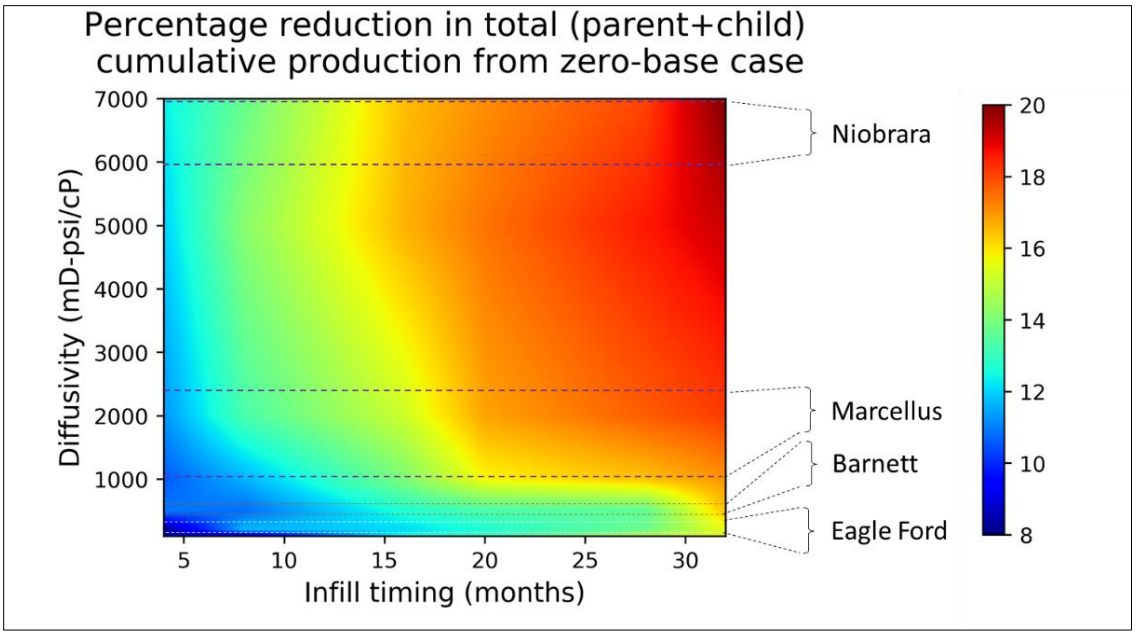

Figure 5.13: Impact of reservoir diffusivity and infill timing (extent of parent well depletion) on the total (parent and child) production

We used multivariate linear regression to find a correlation for estimating total cumulative production for a given diffusivity and infill timing. The obtained correlation is given in equation (5.3), where α is reservoir diffusivity in mD-psi/cP and t_{infill} is the infill timing in months. The metrics for testing the correlation is given in Table 5.2. Figure 5.14 shows the comparison between the correlation model prediction and actual simulation results. We observed that equation (5.3) could predict the ratio of total cumulative production to parent well cumulative production before infill drilling within an acceptable error as compared with the simulation results. This type of correlation can be used in estimating total cumulative production for given reservoir diffusivity and infill timing if parent well cumulative production at the infill time is known.

$$\frac{Total\ cumulative\ production}{Parent\ well\ cumulative\ production\ before\ infill\ drilling} = -1.698 * 10^{-5} * \alpha - 2.12 * 10^{-2} * t_{infill} + 2.2 \quad (5.3)$$

Table 5.2: Correlation prediction comparison with the simulation results

R square	0.84
Average absolute error	3.34 %
Standard deviation in the absolute error	2.59 %

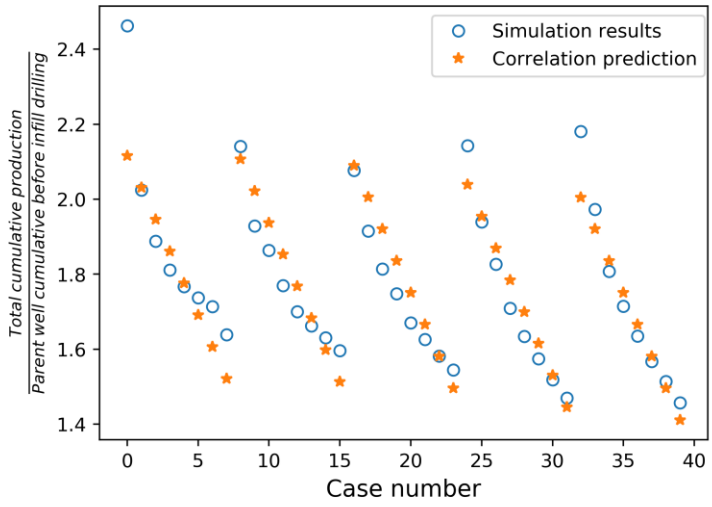

Figure 5.14: Comparison of actual vs. linear model predicted cumulative production

5.6 POSITIVE AND NEGATIVE IMPACT ON PARENT WELL PRODUCTION DUE TO PARENT-CHILD INTERACTIONS

Parent-child well interactions can have a positive or negative effect on parent well production, and this has been reported extensively in the literature (Miller et al., 2016; King

et al., 2017; Xu et al., 2019). There can be several reasons for this wide variability on parent well production, such as infill timing, stress contrast, proppant movement, relative permeability effects, natural fractures. In this chapter, we have investigated the effect of operating conditions on the parent well production performance after child well fracturing. The same case as described in the previous section, is used for this investigation. We analyzed two operating scenarios of the child well as demonstrated in Figure 5.15. In the first scenario, the child well starts producing at the same pressure as the parent well (Case-1 in Figure 5.15). In this case, the bottom hole pressure in the child well is lower than the depleted region around the parent well as the bottom hole pressure is fixed at 1000 psi, hence, the child well produces from both the virgin reservoir and the depleted region (near the parent well). As the child well and the parent well both produce from the same depleted region, the production from the parent well is impacted negatively. In the second scenario, the child well is kept shut-in after stimulation (Case-2 in Figure 5.15). This is an extreme case of production from the child well (child well production rate = 0) simulating a delay in the flowback of the child well due to complications in field operations. In this scenario, the high conductivity of the child well fractures allows the reservoir fluid to flow from the high pressure region (near the child well) to the depleted region (near the parent well). As this flow of the fluid increases the pressure of the reservoir near the parent well and allows the parent well to drain a larger reservoir region with higher pressure, it positively impacts the production rate from the parent well. This extreme case may be an unlikely scenario, although a higher bottom hole pressure in the child well can explain the positive impact observed in parent well production. Figure 5.16 shows the production rate for parent and child well for both case 1 and 2. From this analysis we can conclude that child well-operating conditions can significantly impact parent well production. Although, in our

simulations we didn't consider any direct connection between the fractures of parent and child wells, we observed a positive impact of 30% and a negative impact of 40% based on two extreme operating conditions. A direct connection between the fractures of parent and child wells (fracture driven communication) is expected to have a much larger influence on the production of the parent well as has been observed in the field (Whitfield et al., 2018).

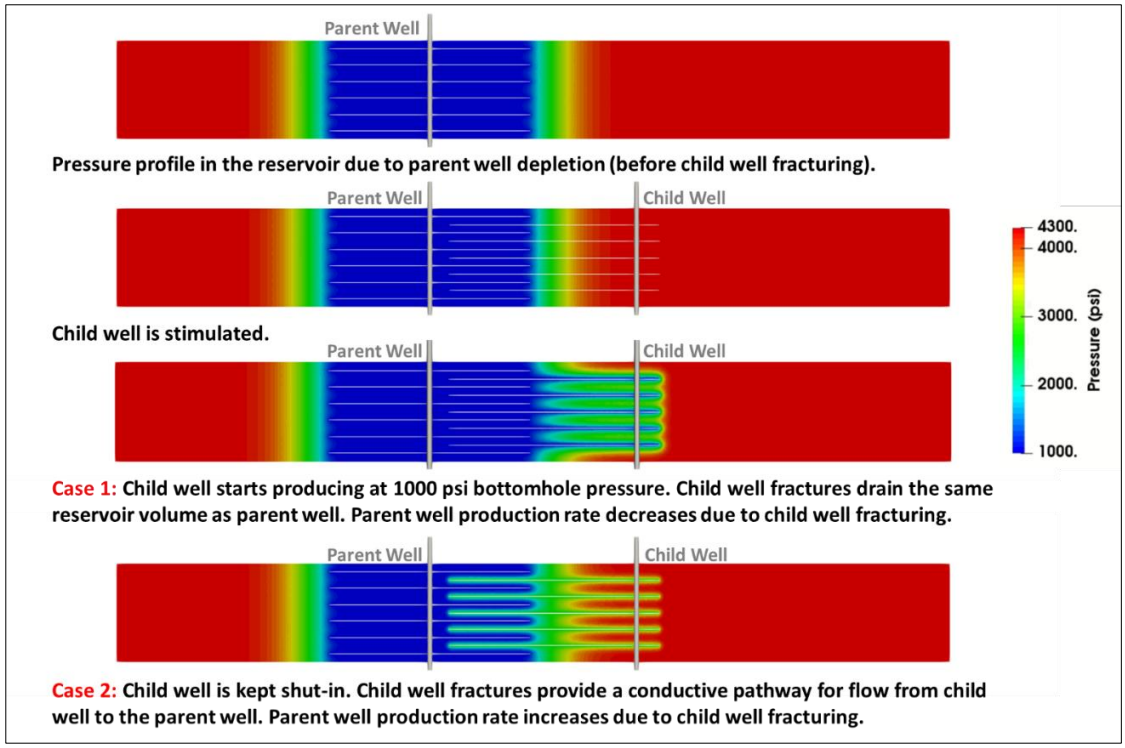

Figure 5.15: Child well operating condition affects the parent well production. Parent well production decreases when child well starts producing (Case-1). Parent well production gets a boost when child well is kept shut-in after stimulation (Case-2).

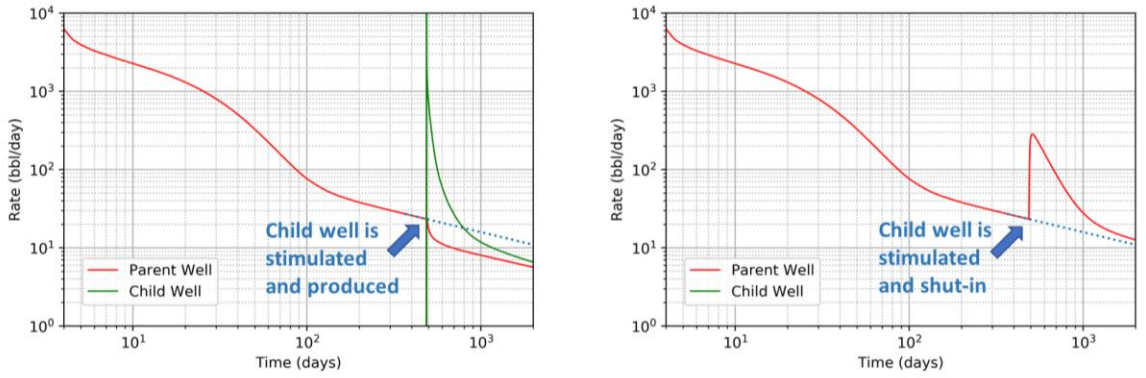

Figure 5.16: Depending upon the child well operating condition, negative and positive effect on parent well production is observed.

5.7 IMPACT OF WELL SPACING ON PARENT-CHILD WELL INTERACTIONS:

Three well spacing (660 ft, 754ft, 880 ft) cases were simulated. The volume of fracturing fluid was kept constant for all the cases. Therefore, parent well fracture length was the same for all well spacing cases. At larger well spacing, the parent well depletion pressure front takes longer to reach the child well. The impact of stress reduction on the child well fracture growth decreases with an increase in well spacing. Consequently, child well fracture asymmetry decreases with an increase in well spacing for a given infill timing. To quantify the impact of parent-child interactions, we calculated the percentage reduction in total (parent+child) cumulative production with respect to zero-base case (parent and child well fractured simultaneously). The percentage reduction in total cumulative production is plotted against infill timing in Figure 5.17. We observed that for lower well spacing, the impact of parent-child well interaction on production is higher. For tighter well spacing and delayed infill timing, the simulations indicate a 20% reduction in performance compared to a 13% reduction for a larger well spacing. This indicates an optimized field development strategy can potentially yield a 15% improvement in performance. This

simulation does not include the upsized child well completions, which can provide additional mitigation benefits. The authors realize that a real optimized scenario is a balance between cumulative production, section NPV, rate of return, and development decisions should be adjusted accordingly.

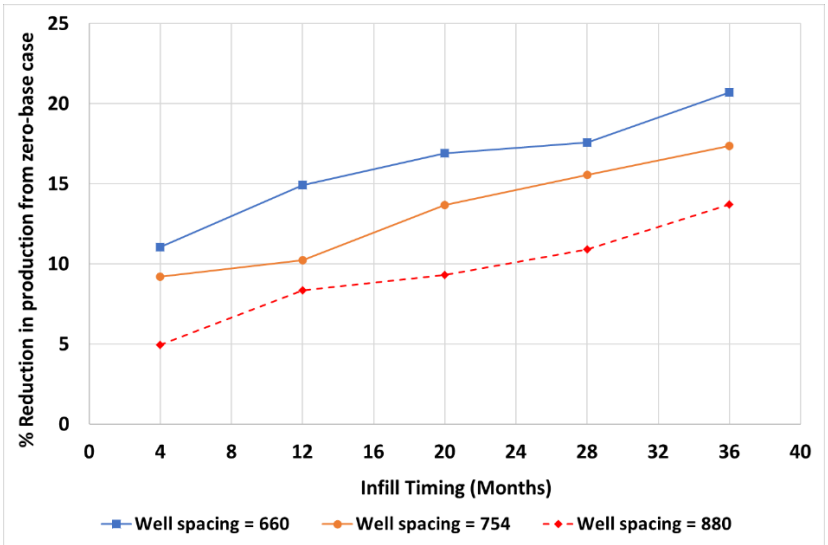

Figure 5.17: Impact of well spacing on parent-child well interactions. Loss in total production increases with decrease in well spacing.

5.8 CONCLUSIONS

In this chapter, we quantified the impact of parent well depletion on fracture propagation from child wells. Geomechanical reservoir simulation results were presented that show the impact of reservoir flow properties, and infill timing (extent of depletion in the parent well) on child well fracture growth. Some important conclusions can be drawn from this chapter are summarized below:

- The interconnected nature of infill timing, well spacing, and reservoir diffusivity has a significant impact on the overall financial and well performance of the parent and child wells.
- Delayed infill timing increases child well fracture asymmetry.
- Child well fracture asymmetry increases with:
    - Increase in reservoir permeability.
    - Decrease in porosity, reservoir fluid viscosity, and compressibility.
- Combining reservoir and fluid properties into the hydraulic diffusivity $\left(\frac{k}{\phi\ \mu\ c_t}\right)$ reduces the number of parameters for depletion pressure and stress calculation and hence child well fracture growth.
- Asymmetric fracture propagation in the child well leads to an overlap in the drainage area of the parent and child well fractures. Due to this overlap, total production (parent + child well) decreases with an increase in fracture asymmetry.
- Child well fracturing can have a positive or negative effect on parent well production depending upon the well operating conditions.
- The impact of parent-child interaction on production decreases with increasing well spacing if the volume of fluid injected and infill timing is kept constant.
- For tighter well spacing and delayed infill timing, the simulations indicate a 20% reduction in performance compared to a 13% reduction for a larger well spacing. Similar or more significant impacts are observed in the field where mechanisms other than asymmetric fracture growth (such as direct frac hits) are responsible for a reduction in cumulative production.

Chapter 6: Diagnosing Fracture Wellbore Connectivity Using Tracer Flowback

Existing fracture diagnostic methods such as micro-seismic monitoring and tiltmeters do not provide information about fracture connectivity to the wellbore. In this chapter, we present a chemical tracer flowback based fracture diagnostic method to (a) estimate the fraction of the created fracture area, which is open and connected to the wellbore and (b) understand the effect of induced un-propped (IU) fracture closure on the tracer response.

6.1 INTRODUCTION

The productivity of a hydraulically fractured well depends on the fracture geometry and fracture-wellbore connectivity. An accurate estimation of propped fracture geometry can also help in optimizing the hydraulic fracture design. Several fracture diagnostic methods have been developed to estimate fracture geometry. The most common fracture diagnostic methods are microseismic, tiltmeter, well testing, production logging, temperature logging, radioactive tracers, chemical tracers, and water hammer measurements. Each of these diagnostic methods have inherent advantages and limitations. Tiltmeter and microseismic mapping provide information about the dimensions and extent of the fracture network but cannot provide information about the fracture conductivity and the fracture connectivity to the wellbore. On the other hand, fluid and tracer transport are

This chapter is adapted from papers URTeC- 2902023 (Kumar, A., and Sharma, M.M., 2018. "Diagnosing Fracture-Wellbore Connectivity Using Chemical Tracer Flowback Data." In Unconventional Resources Technology Conference) and Energies 13-05644 (Kumar, A. and Sharma, M.M., 2020. Diagnosing Hydraulic Fracture Geometry, Complexity, and Fracture Wellbore Connectivity Using Chemical Tracer Flowback. Energies, 13(21), p.5644.). In these papers, Kumar developed the tracer transport model, designed, and performed the research, and documented the results.

dominated by open and connected fractures and how well they are connected to the wellbore, and these are reflected in the tracer response curve. Chemical tracer flowback analysis can be used as an alternative fracture diagnostic method to extend or complement traditional diagnostic tools.

Single-well chemical tracer tests for hydraulic fracture diagnosis were first investigated by Gardien et al. (1996). They used tracer flowback simulations to investigate the influence of fracture geometry on the shape of the tracer response curve. Elahi and Jafarpour (2015) investigated the sensitivity of tracer flowback to fracture length and conductivity. Tian et al. (2016) presented a partitioning chemical tracer-based method to estimate fracture volume. These studies were based on static planar bi-wing fracture geometry and constant fracture conductivity during flowback.

Li et al. (Li et al., 2017) analyzed chemical tracer flowback to evaluate the fracture network using temporal moment and classified the fracture network depending upon the degree of primary and secondary hydraulic fractures. In this study a correlation analysis between cumulative flow capacity and cumulative storage capacity was used and the tracer injection modeling during the fracture propagation was not considered in the analysis. Li et al. (Li et al., 2019) improved previous tracer flowback analysis by conducting numerical experiments by generating the fracture network stochastically, and modeling tracer transport in discrete fracture networks. They introduced a new parameter, conductivity weighted effective fracture density to describe the secondary fracture. Although fracture conductivity was not assumed to be uniform, there was no information about the impact of fracture propagation on tracer transport during tracer injection.

Existing flowback tracer analysis studies have ignored fracture propagation during tracer injection and fracture conductivity changes during flowback due to geomechanical

effects. However, during flowback, as fracture pressure is reduced, the induced unpropped (IU) fracture can close over time and lead to tracer retention in the reservoir and fractures. The IU fracture closure affects the tracer recovery, and this is clearly reflected in the tracer response curve. Models that assume static planar fractures with no fracture closure due to pore pressure depletion are unable to capture these important features of the tracer response curve.

In this chapter, we present the tracer injection and flowback simulations coupled with fracture propagation and fracture closure modeling. The Tracer transport model developed for this study has been described in detail in chapter 2 (section 2.2.4).

6.2 TRACER FLOWBACK SIMULATIONS WITH FRACTURE PROPAGATION

We simulated water-soluble tracer slug injection and flowback for a propagating planar fracture. Important reservoir and geomechanical properties for these simulations are summarized in Table 6.1.

Table 6.1: Reservoir and geomechanical properties for tracer flowback simulations.

Property	**Value**
Porosity	0.1
Reservoir Permeability	Varied from 10 nD to 5 µD
Initial Reservoir Pressure	40 MPa
Young's Modulus	20 GPa
Maximum Horizontal Stress (S_{Hmax})	52 MPa
Minimum Horizontal Stress (S_{hmin})	50 MPa

Fracturing Fluid Injection Rate	10^{-4} m^3/sec
Total Injection Time	30 Minutes
Injected Tracer Concentration	0.01 by volume
Flowback Pressure	20 MPa

Fracturing fluid was injected at a constant injection rate for 30 minutes. The tracer slug was injected for 15 minutes at a constant concentration (0.01 by volume). Tracer concentration inside the propagating fracture is shown in Figure 6.1. During the early time of fracture propagation, tracer concentration in the hydraulic fracture is the same as the injected tracer concentration. Once the tracer injection is stopped, injected fracturing fluid displaces the tracer towards the fracture tips and in the reservoir through leak-off. At the start of the flowback, tracer concentration near the wellbore is very low. Flowback tracer concentration starts with a very low value, and we observe a Gaussian type tracer response curve with a single peak, as shown in Figure 6.2.

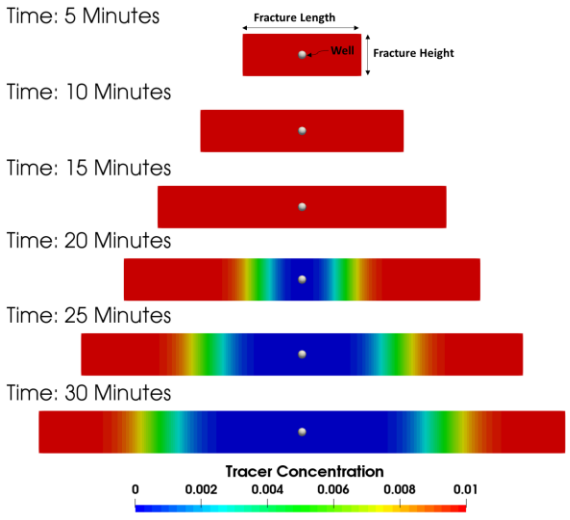

Figure 6.1: Tracer slug injection in a propagating planar fracture. Fracture surface plane is shown at different times during fracture propagation.

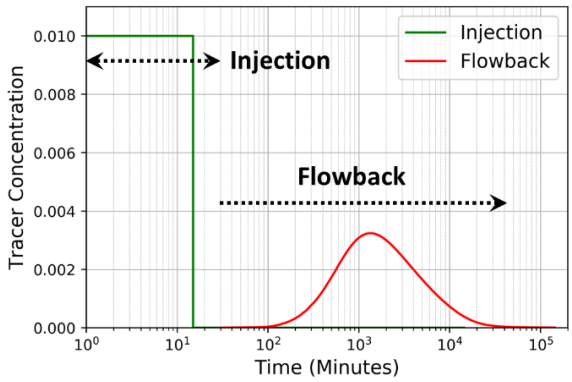

Figure 6.2: Tracer response curve from a tracer slug injection and flowback.

6.2.1 Impact of Fracture Length on Tracer Response Curves

Preliminary tracer tests were simulated to obtain tracer response curves by varying reservoir permeability from 10 nD to 5 µD. An increase in the reservoir permeability leads to a decrease in the created hydraulic fracture length due to higher leak-off rates (all other parameters are kept constant). The objective of this exercise was to analyze the difference in the tracer response curves to get some qualitative information about fracture length. An equal volume of tracer was injected in all cases, and the flowback was performed at the same constant bottom-hole pressure in each case. In these preliminary simulations, we did not consider fracture closure during flowback. For our analysis, we normalized the tracer concentration in the flowback fluid against injected tracer concentration,

$$Dimensionless\ Tracer\ Concentration\ (C_D) = \frac{Tracer\ Concentration\ in\ Flowback}{Injected\ Tracer\ Concentration} \quad (6.1)$$

Dimensionless tracer concentration (C_D) vs. time is plotted on a semilog scale for all reservoir permeability (K_m) cases (Figure 6.3). We observed that an increase in the reservoir permeability leads to an early peak in the tracer response curve. An increase in

reservoir permeability leads to an increase in the tracer dilution due to the higher flow rate of reservoir fluids from the matrix to fracture during flowback. Also, in case of lower fracture length (higher matrix permeability), the tracer penetrates deeper into the matrix, and dilution of tracer occurs due to mixing with the reservoir fluid. This tracer dilution leads to a decrease in the tracer peak concentration in higher matrix permeability cases, and increased dispersion is observed in the tracer response curve. Figure 6.4 shows the plot of peak tracer concentration vs. fracture half-length. We observed that the peak tracer concentration during flowback increases with an increase in the fracture length. The time at which tracer concentration reaches the peak value was measured for each case and is plotted vs. fracture length (Figure 6.5). We observed that the time of peak concentration is directly proportional to fracture length, and this correlation can be used to obtain qualitative information about fracture length.

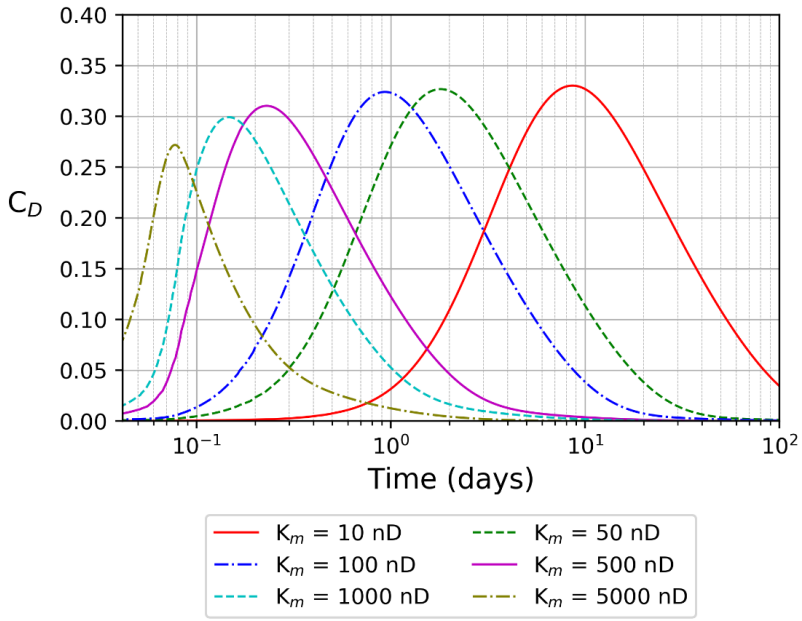

Figure 6.3: Tracer response curves during flowback for several reservoir permeability cases. An increase in reservoir permeability leads to an early peak and also a decrease in the peak tracer concentration.

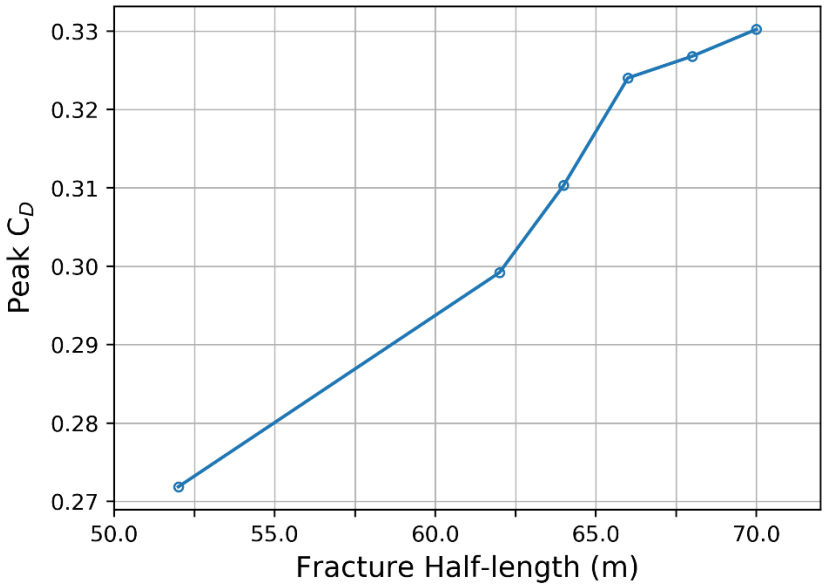

Figure 6.4: Peak tracer concentration vs. fracture half-length.

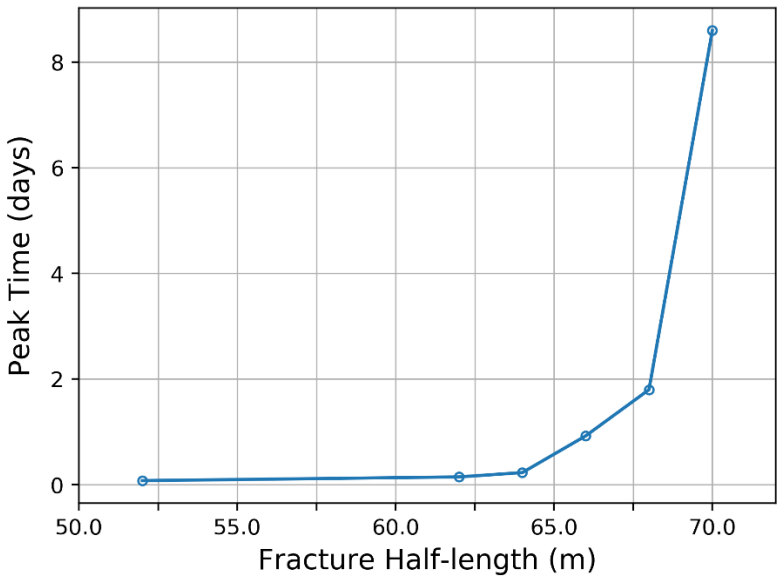

Figure 6.5: Time at which peak tracer concentration is observed increases with an increase in the fracture length.

Figure 6.6 shows the plot of tracer recovery (as a percentage of tracer injected) against time. Since fracture closure was not modeled in these simulations, we observed almost 100% recovery of the injected tracer during flowback. However, several field studies have shown very low tracer recovery (King and Leonard, 2011; Spencer et al., 2013; Goswick et al., 2014). The tracer retention due to fracture closure can help in understanding the low tracer recovery, which is explained in the next section.

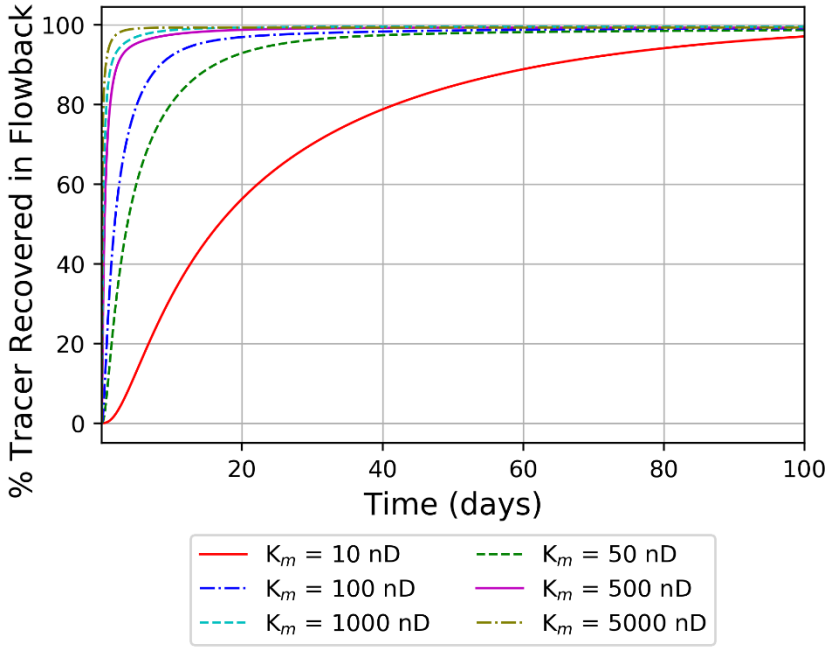

Figure 6.6: Flowback tracer recovery vs. time when fracture closure is not modeled.

6.2.2 Impact of Fracture Closure on Tracer Flowback

We analyzed the impact of fracture closure on the tracer response curve and tracer recovery. During flowback, increased effective stress on the fracture faces can lead to fracture closure. This fracture closure hinders the tracer transport from the fracture to the

wellbore. We model the fracture closure phenomenon using the Barton-Bandis normal contact stiffness relationship (Bandis et al., 1983), as explained in chapter 2. The magnitude of fracture closure depends on the fracture stiffness (K_{ni}) and offset width. In this section, we varied the fracture stiffness (from 10^8 Pa/m to 10^{11} Pa/m) to analyze the impact of fracture closure on the tracer flowback. Figure 6.7 illustrates the sensitivity of stiffness on the fracture width during the closure. We observed that the rate of fracture closure is inversely proportional to the stiffness.

Figure 6.8 shows the impact of the fracture closure rate on the tracer response curve. Flowback tracer concentration decreases sharply when fracture stiffness is lower (faster fracture closure). We also observed that the peak concentration decreases with an increase in fracture closure rate. Figure 6.9 and Figure 6.10 demonstrate the impact of fracture closure on the tracer recovered during flowback. These simulation results indicate that the tracer recovery decreases with an increase in the fracture closure. These preliminary simulations were conducted using a planar bi-wing fracture. In the next few sections, this analysis is extended for complex fractures.

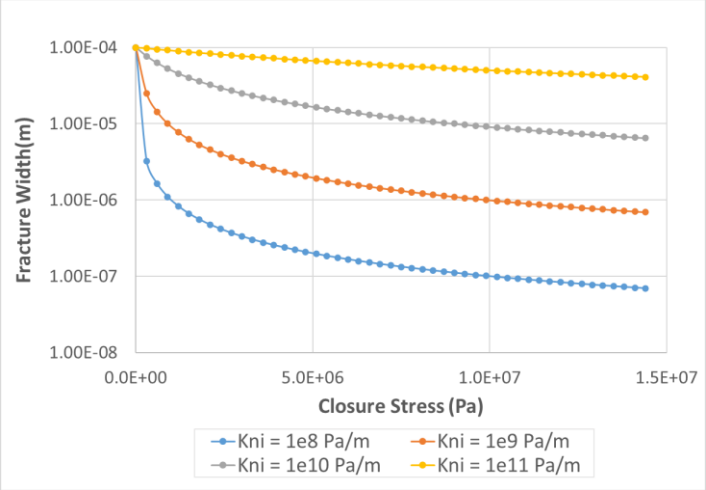

Figure 6.7: Fracture closure rate is controlled by stiffness (Kni)

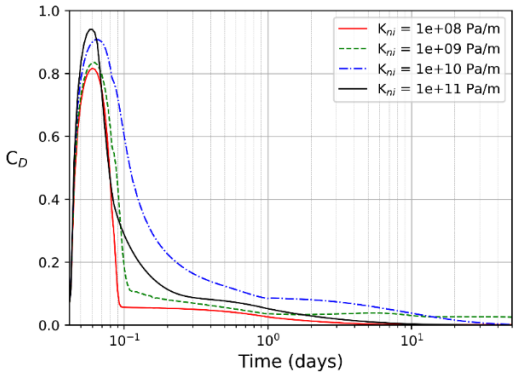

Figure 6.8: Impact of fracture stiffness (rate of fracture closure) on the tracer response curve.

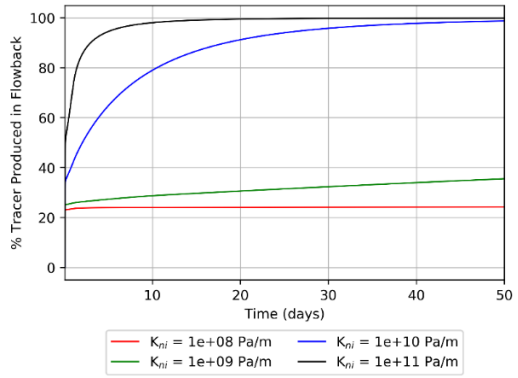

Figure 6.9: Flowback tracer recovery vs. time for several fracture stiffness values.

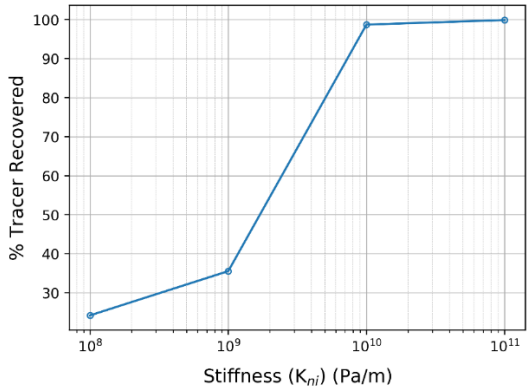

Figure 6.10: Percentage tracer recovered decreases with a decrease in the fracture stiffness. At lower fracture stiffness, fracture closure is faster, and this leads to tracer retention in the fracture and the reservoir.

6.2.3 Effect of Secondary Fracture

In this section, we analyzed the effect of secondary fracture intensity on the flowback tracer concentration of a multifractured horizontal well. A simulation case was set up with four fractures on a single wellbore having a different spacing of secondary fractures (Figure 6.11). A dual porosity-dual permeability model was used, and secondary fracture spacing was varied from 2 ft to 20 ft. Barton-Bandis fracture permeability model (Bandis et al., 1983) was used to analyze the secondary fracture closure effects. Each fracture was tagged with a unique tracer, and an equal volume of tracer was injected in all four fractures.

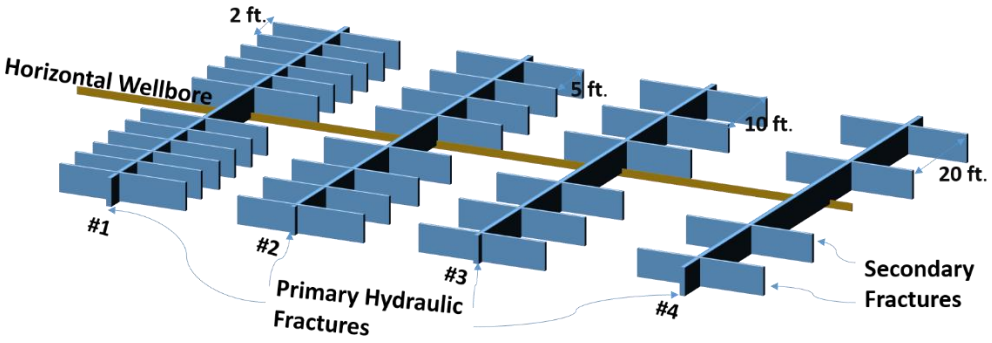

Figure 6.11: A simulation model for a multifractured well with secondary fractures

During flowback, the secondary fractures close because of the increase in the effective stress caused by pressure depletion due to production. Because of fracture closure, tracer flowback to the surface decreases. Simulation results (Figure 6.12) indicate that the tracer recovery decreases with an increase in fracture complexity (higher number of secondary fractures).

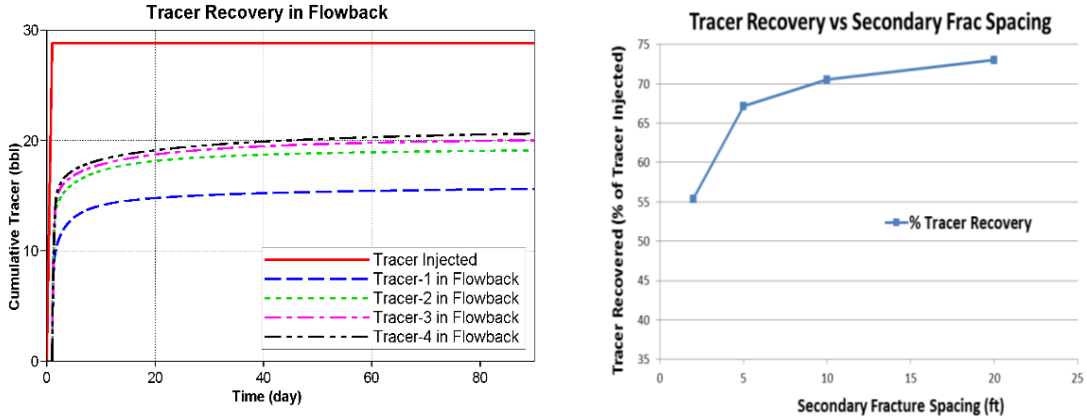

Figure 6.12: Effect of fracture complexity on tracer recovery.

6.3 Fracture Wellbore Connectivity using Chemical Tracer Flowback

In this section, we present a simulation study to model tracer injection and flowback in a complex fracture network with the help of an effective model to analyze the field tracer tests.

6.3.1 Complicated Tracer Response Curves Typically Observed in a Field Tracer Test

A typical field tracer test in a hydraulically fractured well shows very complex tracer response curves (Figure 6.13). There is no uniform trend observed in a tracer flowback test. A few stages have negligible tracer concentration during flowback/production, indicating that these stages have a minimal contribution towards flowback/production. By ignoring these small contributing stages, we can divide tracer response curves into two main categories.

- Simple tracer response curves with a single distinct early peak. (Figure 6.14(a))
- Tracer response curves with multiple peaks. (Figure 6.14 (b))

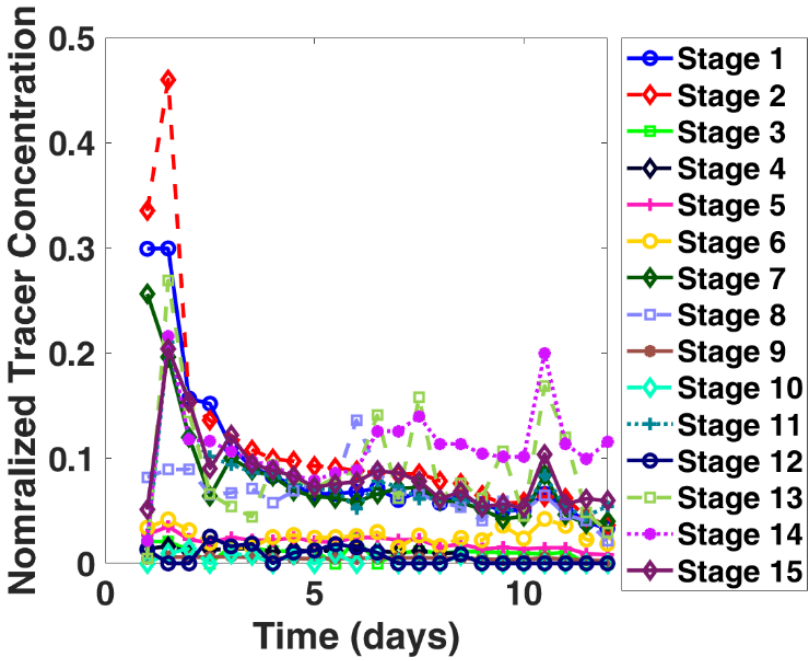

Figure 6.13: Tracer response curve from a multi-fractured well having 15 stages. Each stage was tagged with a unique chemical tracer.

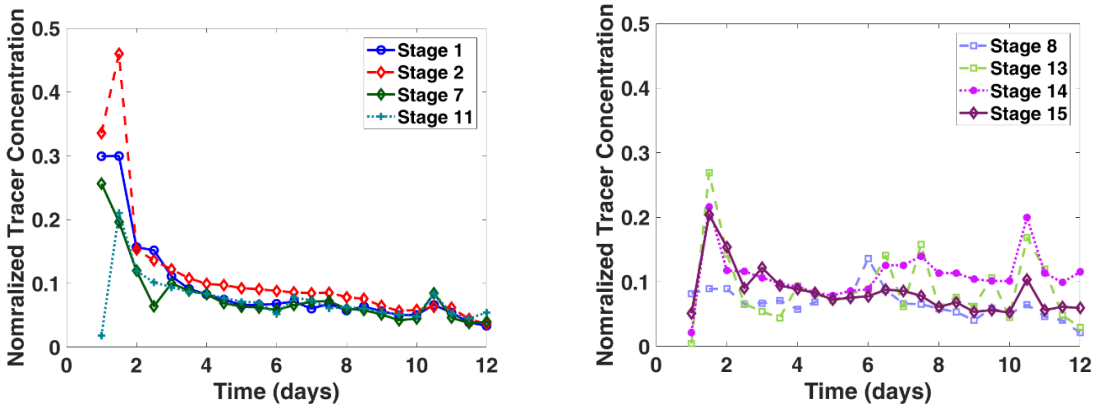

(a) (b)

Figure 6.14: Tracer response curve divided into two categories. Plot (a) shows stages having a single early peak. Plot (b) shows stages having multiple peaks.

As explained in the previous sections, if we analyze tracer flowback from a slug injection tracer test with a propped fracture that is connected to the wellbore, we observe a Gaussian type tracer response curve with one peak (Figure 6.2). Johnston et al. (2005) classified the tracer response curves into four general types (Gaussian, backward tailed, bimodal, multimodal) based on the matrix and fracture flow segregation depending upon fracture network heterogeneity. In their study, fracture aperture was assumed to be constant, and geomechanical effects were not considered. However, in the case of a tracer flowback test in a hydraulic fracturing operation, fracture width may change during flowback due to changes in fracture pressure. Fracture closure in a complex fracture network can lead to a decrease in the fracture connectivity to the wellbore (Seth et al., 2018). This reduction in fracture wellbore connectivity will be reflected in the tracer recovery and hydrocarbon production. The impact of fracture closure on the number of peaks in a tracer response curve, tracer recovery, and hydrocarbon production are discussed in this work using a tracer flowback simulation model.

6.3.2 Simulation Model Description

In a naturally fractured reservoir, complex fracture networks are formed during hydraulic fracturing operations (Fisher et al. 2002; Weng et al. 2011; Shrivastava and Sharma 2018). Figure 6.15 shows a hydraulic fracture network along with pre-existing natural fractures. The activated natural fractures in a complex fracture network aligned against maximum stress have relatively small fracture aperture, which makes it difficult for conventional size proppants to flow into them. These activated natural fractures do not contain proppant and can be referred to as induced unpropped (IU) fractures (Sharma and

Manchanda, 2015). These IU fractures may close during flowback/production because of the high stress acting on them.

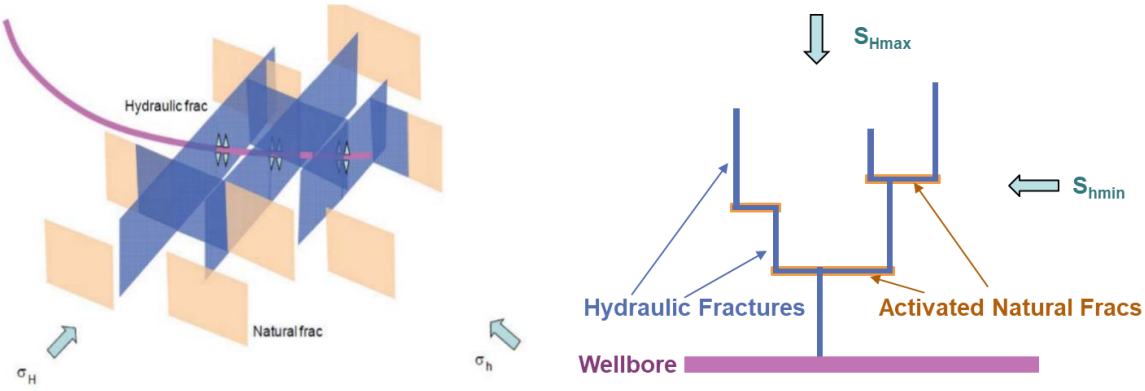

Figure 6.15: Complex fracture network created in the presence of natural fractures (Weng et al. 2011).

Fractures in a complex fracture network can be put into three categories based on the connectivity of a fracture to the wellbore: 1) closed fractures, 2) open and connected fractures, and 3) fractures open but not connected to the wellbore (Figure 6.16).

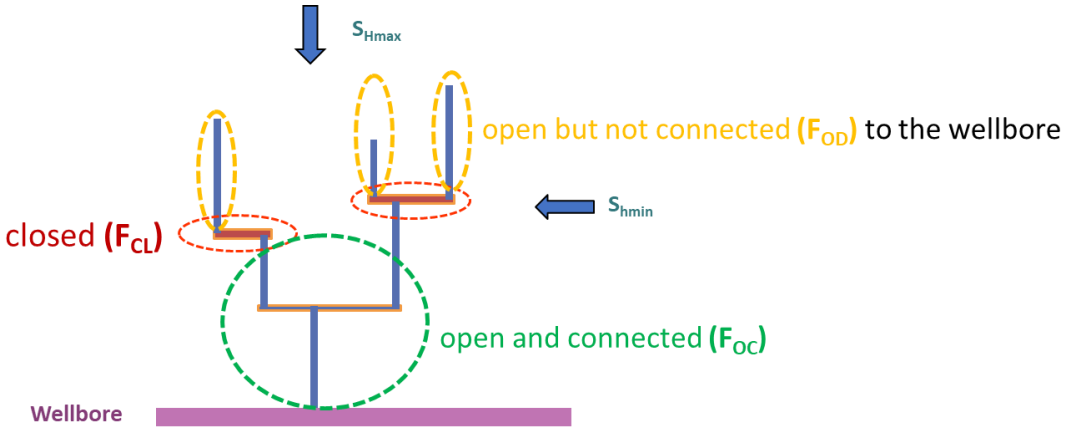

Figure 6.16: Fractures in a complex fracture network categorized based on the connectivity of a fracture to the wellbore

In the case of a low permeability reservoir, early flow in the reservoir at the matrix-fracture interface is mostly linear, and a complex fracture network can be simplified to an effective model comprised of multiple planar fracture segments connected to each other. Figure 6.17 shows a complex fracture network represented as an "effective" model having multiple segments with variable widths during flowback. Open fracture segments are assumed to have infinite conductivity (1000 mD in our simulations). The middle segment (F_{CL}) corresponds to activated natural fractures aligned against the maximum stress.

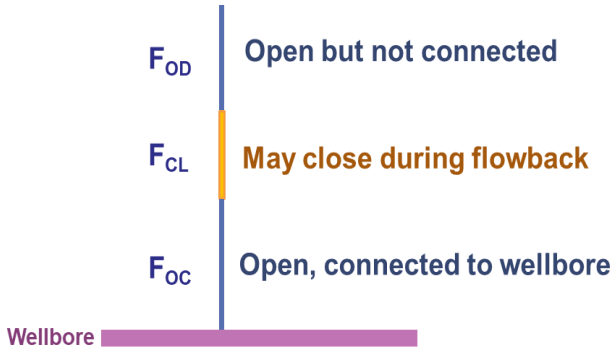

Figure 6.17: Complex fracture network simplified to an effective model.

To analyze the effect of IU fracture closure, middle segment (F_{CL}) fracture closure was modeled using the Barton-Bandis contact relationship (Bandis et al. 1983). Fracture closure modeling has been described in more detail in chapter 2. Important reservoir properties for these simulations are summarized in Table 6.2. Oil-water relative permeability is shown in Figure 6.18.

Table 6.2: Reservoir and geomechanical properties for effective model tracer simulations.

Property	**Value**
Porosity	0.1
Reservoir Permeability	1 µD
Initial Reservoir Pressure	4000 psi
Injected Tracer Concentration	0.01 by volume
Flowback Pressure	500 psi
Fracture Stiffness (K_{ni})	Varied from 10^4 to 10^7 psi/ft

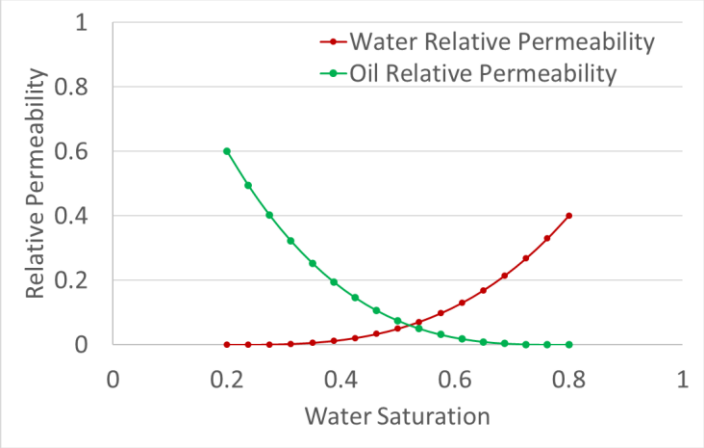

Figure 6.18: Oil-water relative permeability curve for tracer simulations.

We analyze the impact of IU fracture closure on the tracer response curve, tracer recovery, and hydrocarbon production. We use the effective model, as described in Figure 6.17. For our sensitivity analysis, the same volume of water-soluble tracer was injected in each case, and tracer flowback was performed at a constant bottomhole pressure. Tracer

concentration at the producer well was normalized (C_D) against the injected tracer concentration and plotted against time.

6.3.3 Multiple Peaks in the Tracer Response Curve Due to the Fracture Closure in a Complex Fracture Network

First, we analyzed the sensitivity of the fracture closure rate on the tracer response from a complex fracture network. Fracture stiffness (K_{ni}) was varied from 10^4 to 10^7 psi/ft. Figure 6.19 shows the tracer concentration during flowback at different rates of IU fracture closure. Multiple peaks are observed in case of fast closure when the closed IU fracture permeability is lower than the propped fracture permeability. The closed IU fracture acts as a resistance to tracer flow from the fracture segments far away from the wellbore. This slower flow from the disconnected fracture segments leads to late time peaks in the tracer response curves.

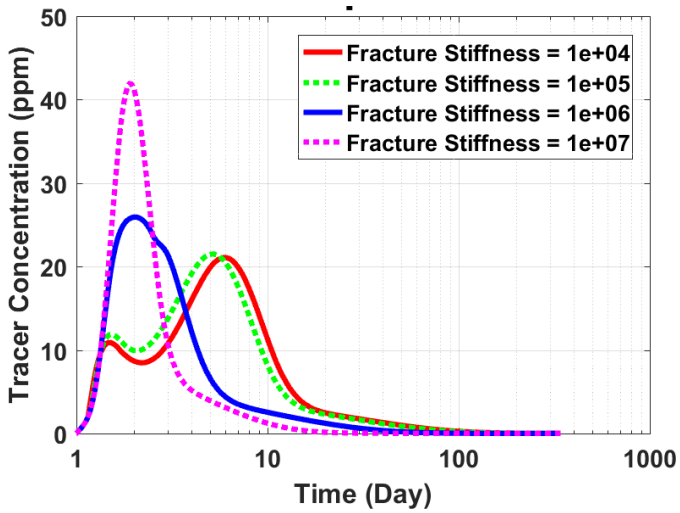

Figure 6.19: The impact of fracture closure rate on tracer response curves from a complex fracture.

Next, we analyzed the impact of the closed IU fracture permeability on the tracer response curves. As per the Barton-Bandis closure model, at a fixed fracture stiffness, the residual fracture permeability (after closure) depends on offset width. We varied offset width so that the closed fracture permeability ranges from the matrix permeability (1 μD) to the propped fracture permeability (1 Darcy). Figure 6.20 shows that multiple peaks are observed when the IU fracture is conductive enough to allow tracer flowback from the fracture segments away from the wellbore. When the residual permeability of the IU fractures is higher (comparable to the propped fracture conductivity), all fracture segments in a fracture network are connected to the wellbore, and flow in the fracture network is equivalent to the flow from a single open fracture. This results in a Gaussian type (single peak) tracer response curve. When the residual permeability of IU fractures is very low (comparable to the matrix permeability), fracture segments behind IU fractures are disconnected from the wellbore and flow in the fracture network is equivalent to the flow from a single fracture with a smaller created fracture network area, and this also results in a Gaussian type (single peak) tracer response curve. However, when the residual permeability of IU fractures has an intermediate value between the matrix and propped fracture permeability, multiple peaks are observed due to delayed flow from the fracture segments connected by IU fractures.

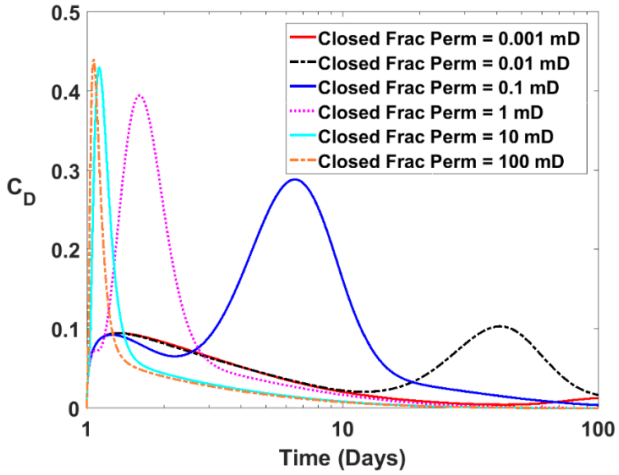

Figure 6.20: Impact of residual fracture permeability of IU fractures on tracer response curves.

Next, we analyzed the impact of the created fracture area, which is open and connected (F_{OC} as shown in Figure 6.17) to the wellbore. Figure 6.21 shows that multiple peaks can be observed when IU fracture closure leads to a reduction in the open connected (F_{OC}) fracture area. We observe that the first open-connected segment flows back early and contributes to the first peak. When the area of the open connected segments is smaller, then early time tracer recovery is lower, and the fracture segments connected via IU fractures lead to the late time tracer peaks. The first peak concentration is found to be proportional to the area of the open-connected segments. Hence, the volume of tracer recovered under the first peak can provide information regarding the fraction of the created fracture network that is open and connected to the wellbore.

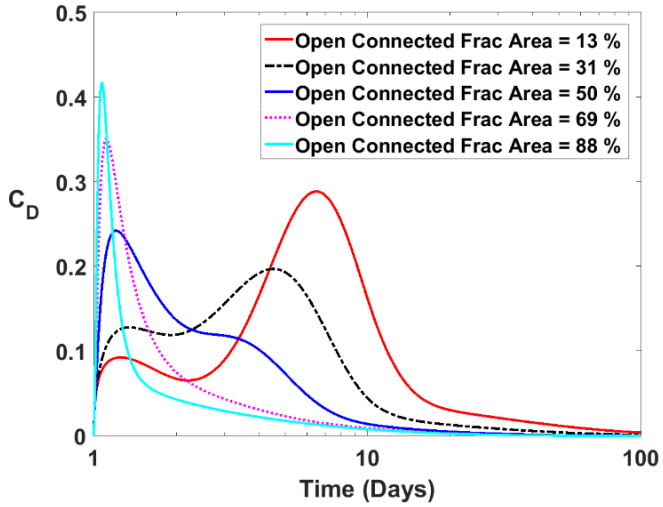

Figure 6.21: Impact of open connected (F_{OC}) fracture area on tracer response curves.

6.3.4 Impact of Fracture Closure on the Tracer Recovery from Complex Fractures

Fracture closure during flowback results in tracer retention in fracture networks, which can lead to low tracer recovery during flowback. Field tracer tests have also indicated very low tracer recovery. Based on our simulation results, we plotted tracer recovery vs. the open connected fracture area. Figure 6.22(a) shows that tracer recovery decreases with a decrease in the open connected fracture area. We also observed that a decrease in closed fracture permeability also leads to lower tracer recovery. Figure 6.22(b) shows the impact of initial water saturation on water-soluble tracer recovery. Lower water saturation reduces the water rate and water-soluble tracer production during flowback, and we observe that the tracer recovery decreases with a decrease in initial water saturation in the reservoir.

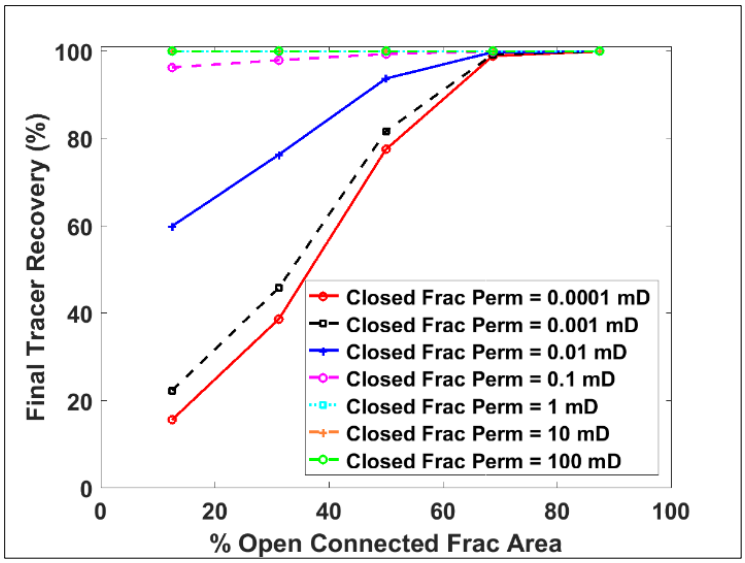

(a)

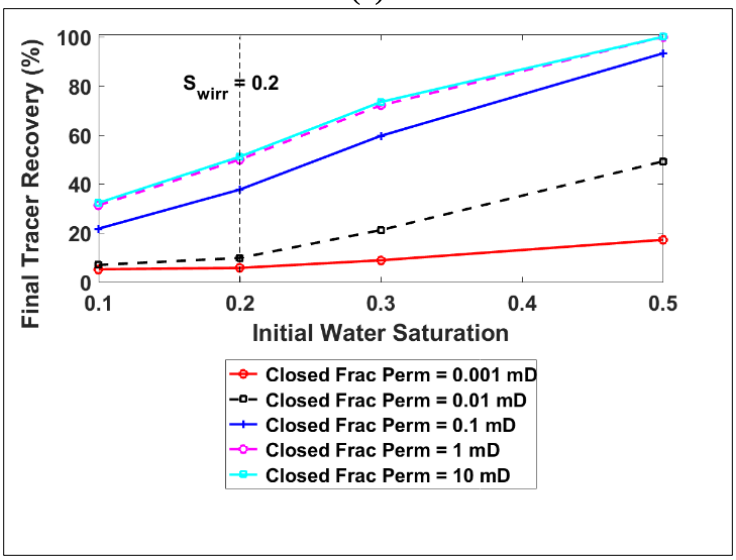

(b)

Figure 6.22: Impact of open connected (F_{OC}) fracture area on tracer response curves.

6.3.5 Tracer Recovery vs. Hydrocarbon Production

We plotted cumulative oil production vs. tracer recovery for all simulation cases. Figure 6.23 shows that there is a strong correlation between production from a stage and the tracer recovery from that stage. This information can be used to calculate the contribution of a stage to the overall flow from a multi-fractured well.

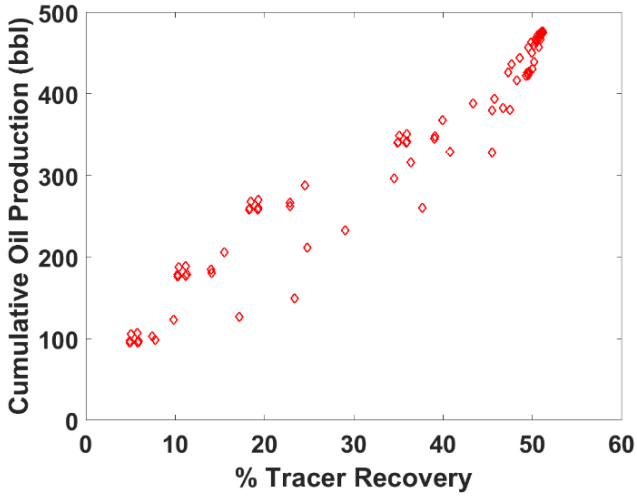

Figure 6.23: Cumulative oil production vs. tracer recovery

6.3.6 Inverse Modeling with Neural Network

Based on the forward modeling of tracer injection and flowback, we have identified the importance of fracture closure on tracer response curves and hydrocarbon production. In this section, we discuss an inverse modeling approach to estimate the fracture parameters from a given set of tracer data.

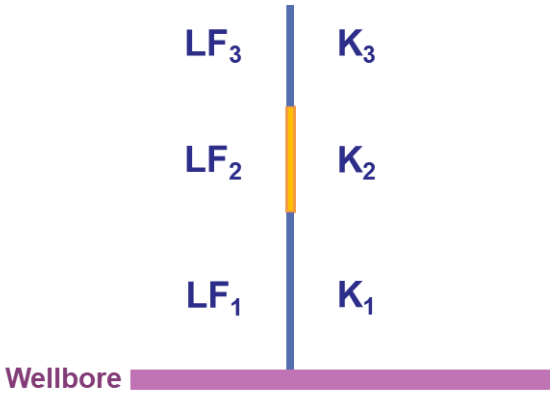

Figure 6.24: Effective model representing three fracture segments

In our effective model (Figure 6.24), we have six parameters (length and permeability of all three segments), and this large number of parameters makes the inverse problem very difficult. We tried to lump these parameters to simplify the inverse problem. We know that the flow from a fracture segment is proportional to the fracture length and permeability of the segment. However, the permeability of a segment will also affect the flow from the segments behind it. Based on these directional correlations, we combined the fracture lengths and permeabilities to define a lumped parameter called the effective connected fracture length (Equation (6.2)). Effective connected fracture length can be defined as:

$$Effective\ Connected\ Fracture\ Length = \frac{log\ K_1}{log\ K_f} * \left[LF_1 + \frac{log\ K_2}{log\ K_f} * \left\{LF_2 + \frac{log\ K_3}{log\ K_f} * (LF_3)\right\}\right] \qquad (6.2)$$

Where K_f is the propped fracture permeability. We observed that lumping all parameters to a single parameter (effective connected fracture length) helps in finding a better fit to the tracer recovery (Figure 6.25). The lumped parameter has a good correlation with tracer recovery and it can be used to predict production.

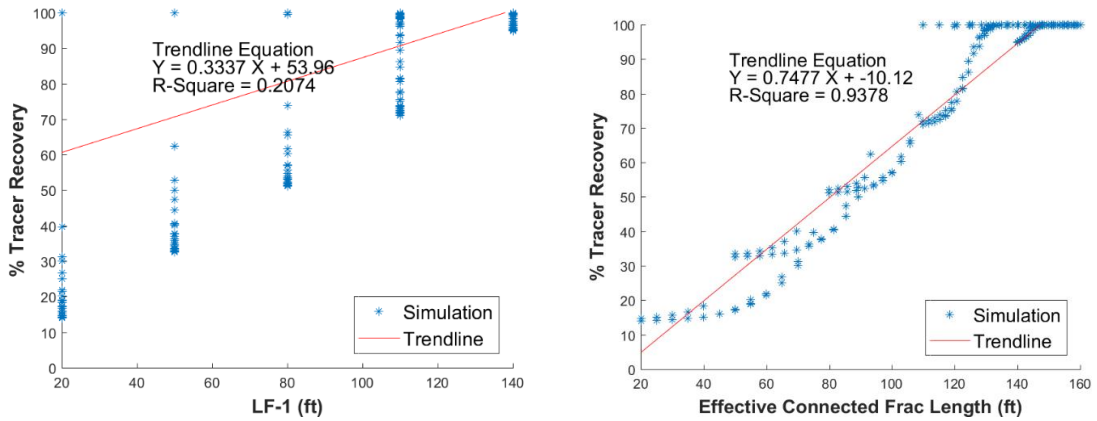

Figure 6.25: Advantage of lumping the fracture lengths and permeabilities to a single parameter (effective connected fracture length). The left plot shows a very weak correlation between tracer recovery and first connected fracture length. The right plot shows that lumping the parameters helps in finding a good correlation to the tracer recovery.

We formulated the inverse problem to estimate the effective connected fracture length from the following observations from a tracer test:

- Tracer recovery
- Number of peaks
- First peak concentration
- First peak time

A neural network-based inverse model was used. The neural network was trained for a set of known tracer response curves and the effective connected fracture length from the simulation cases. The trained neural network was then used for estimating the effective

connected fracture length for cases not included in the training. Figure 6.26 shows that the trained neural network prediction has a good match (error around 5%) with the effective connected fracture length used as the simulation input. A similar type of inverse model can be used for data from an actual field tracer test to estimate the effective connected fracture length. This parameter has a good correlation with the cumulative production.

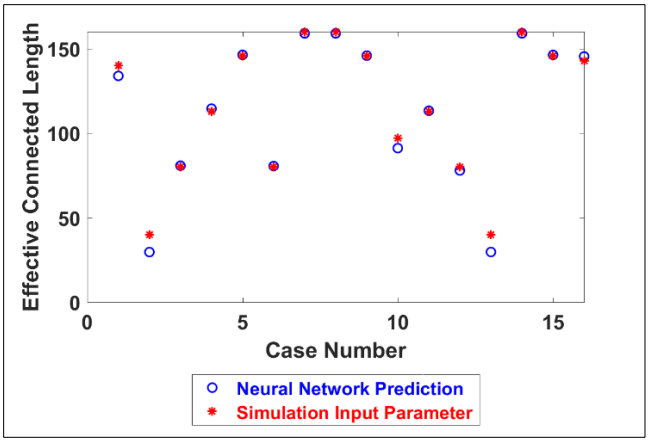

Figure 6.26: Inverse model prediction comparison with the simulation input parameters

6.4 CONCLUSIONS

Understanding the connectivity of a hydraulic fracture network to the wellbore is important while analyzing multi-fractured well performance. In this chapter, we proposed a tracer flowback based method to estimate the open connected fracture area in a created fracture network. We used an effective model to simulate tracer injection and flowback from a complex fracture network. IU fracture closure due to geomechanical effects was modeled using the Barton-Bandis fracture closure model. We performed a sensitivity analysis to quantify the impact of fracture closure on tracer response curves, tracer

recovery, and hydrocarbon production. Important conclusions drawn from this chapter are presented below:

- Multiple peaks in the tracer response curves can be explained by the closure of IU fractures during flowback.
- Tracer recovery (%) and the number of peaks can help determine the fraction of the created fracture area that is open and connected to the wellbore.
- Early time peaks correlate with fracture closure occurring near the wellbore. Late time peaks are observed due to tracer flowback from fractures that are connected to the wellbore through IU fractures.
- The area under the early time peak is directly correlated with the fraction of created fracture area that is in good hydraulic communication with the wellbore.
- The area under later peaks is related to the area of the fracture that is only connected to the wellbore through induced unpropped (IU) fractures. The timing of these peaks is related to the conductivity of the IU fractures.
- Low tracer recovery typically observed in the field can be explained by the closure of induced unpropped fractures and low initial water saturation in the reservoir.
- Production from a stage is directly proportional to the tracer recovery from that stage. This can help in comparing the production performance of a fracture stage with respect to overall flow from a multi-fractured well.

Chapter 7: Integrated Analysis of Tracer and Pressure Interference Tests to Identify Well Interference

Understanding the connectivity between fractured horizontal wells in a multi-well pad is important for infill well drilling and parent-child well interactions. Inter-well tracer and pressure interference tests involve two or more fractured horizontal wells and provide information about hydraulic fracture connectivity between the wells. In this chapter, we present a workflow based on combining the analysis of tracer and pressure interference data to obtain the degree of interference between fractured horizontal wells in a multi-well pad.

7.1 INTRODUCTION

In conventional reservoirs, well interference tests have been widely used to gather information about inter-well communication and reservoir permeability. In such high permeability reservoirs, well interference has been well studied and is based on hydraulic pressure diffusion (pressure communication due to fluid diffusion) in the reservoir. However, in unconventional reservoirs, due to the ultra-low permeability of the reservoir, hydraulic pressure diffusion through the reservoir rock is negligible as compared to the elastic response and hydraulic pressure diffusion through the fracture network. This renders traditional well interference techniques based on hydraulic pressure diffusion through the reservoir inapplicable.

This chapter is adapted from paper SPE-201233-PA (Kumar, A., Seth, P., Shrivastava, K., Manchanda, R., & Sharma, M. M.,2020, "Integrated Analysis of Tracer and Pressure-Interference Tests To Identify Well Interference." SPE Journal. In this paper, Kumar analyzed the HFTS (Hydraulic Fracturing Test Site) inter-well fluid and radioactive tracer communication data and documented the results.

Horizontal wells drilled in ultra-low permeability reservoirs need to be hydraulically fractured to be economical. Hydraulic fracturing is generally done in multiple stages along the length of the horizontal portion of the well and results in the formation of complex fracture networks in the presence of natural fractures (Fisher *et al.*, 2002; Weng *et al.*, 2011; Shrivastava and Sharma, 2018; Shrivastava *et al.*, 2018). In the case of a multi-well pad, the hydraulic fracture network of a well can intersect with networks from other wells resulting in frac-hits (Sardinha *et al.*, 2014). Moreover, in a non-uniform pore pressure field, these fractures may be attracted towards depleted regions due to reduced total stress after production (Manchanda *et al.*, 2018; Agrawal and Sharma, 2018). With the increasing size of frac jobs and the size of the created fractures, the probability of interaction between multiple wells has increased. Wells in a pad are more likely to be connected through a hydraulically conductive fracture pathway. These conductive fracture pathways can lead to interference between wells and can be diagnosed using data collected in the field. Chemical tracer, radioactive proppant tracer, microseismic data, and pressure data are the most common forms of data that can help in detecting the interference between wells. In this chapter, we analyzed chemical tracer, radioactive proppant tracer, and pressure interference data to study well interference. The advantages and limitations of each of these techniques are shown in Table 7.1. We show that these methods complement each other and facilitate a comprehensive analysis of well interference during production. For instance, radioactive proppant tracer provides well communication information post-pumping (during early-time production only). Proppant tracers, when used in conjunction with pressure interference data, as shown in this chapter, provide well interference information throughout the life cycle of the producing wells.

Table 7.1: Comparison of the well interference diagnostic methods

	Chemical Fluid Tracer Tests	**Radioactive Proppant Tracer Test**	**Pressure Interference Test**
Description	Chemical tracers are injected with fracturing fluids to analyze stage efficiency and inter-well communication.	Proppants are tagged with a radioactive material (low-level gamma-emitting sources) to identify frac initiation points, proppant interference between fractures and wells (King and Leonard, 2011).	Pressure interference test is conducted by measuring pressure at a monitor well by applying pressure or rate changes at another source well to identify communication between the wells.
Advantage	Chemical tracer analysis provides a measurement for a more extended period for different regions of the well. This is a non-intrusive method and does not lead to any risk to the well. (Panichelli et al., 2017)	Radioactive proppant tracer tests provide information about proppant placement in the fractures, which helps in distinguishing propped fractures from unpropped fractures.	Pressure interference test is relatively inexpensive and requires only operational changes in the wellbore. It is a direct measurement of real-time well interference.
Limitation	Tracer concentration measurement can be skewed due to irregular flow patterns	Radioactive proppant tracer tests provides only near-wellbore measurement.	Pressure changes in the monitor well can be influenced by operational changes

	(e.g., slugging) in the wellbore. So real-time tracer analysis can be inaccurate and should be used only as a trend over time. (King and Leonard, 2011)	Radioactive tracer logging is expensive and requires well intervention, and it is difficult to obtain the propped fracture information during production.	in nearby producing wells if surface equipment is shared among wells.

Pressure interference tests in hydraulically fractured horizontal wells have been used to understand the interference between wells (Sardinha *et al.*, 2014; Awada *et al.*, 2015; Dawson and Kampfer, 2016; Roussel and Agrawal, 2017; Seth *et al.*, 2018; Seth *et al.*, 2019). These tests involve two or more fractured horizontal wells (source and monitor wells) and provide information about hydraulic fracture connectivity (or lack thereof) between the wells. Pressure interference tests during production involve monitoring the pressure changes at the monitor well in response to rate changes at the source well. If sudden rate changes (shut-ins or restarts) in the source well cause a change in the pressure profile of the monitor well, we can infer that the source and monitor well are interfering. As shown in Figure 7.1 (Awada et al., 2015) event 4 and 5 represents the pressure interference events at well A due to changes in well 0. Well A is shut-in for 12 days before well 0 starts production. The restart of well 0 results a change in the pressure build-up profile of well A (event 4 and 5).

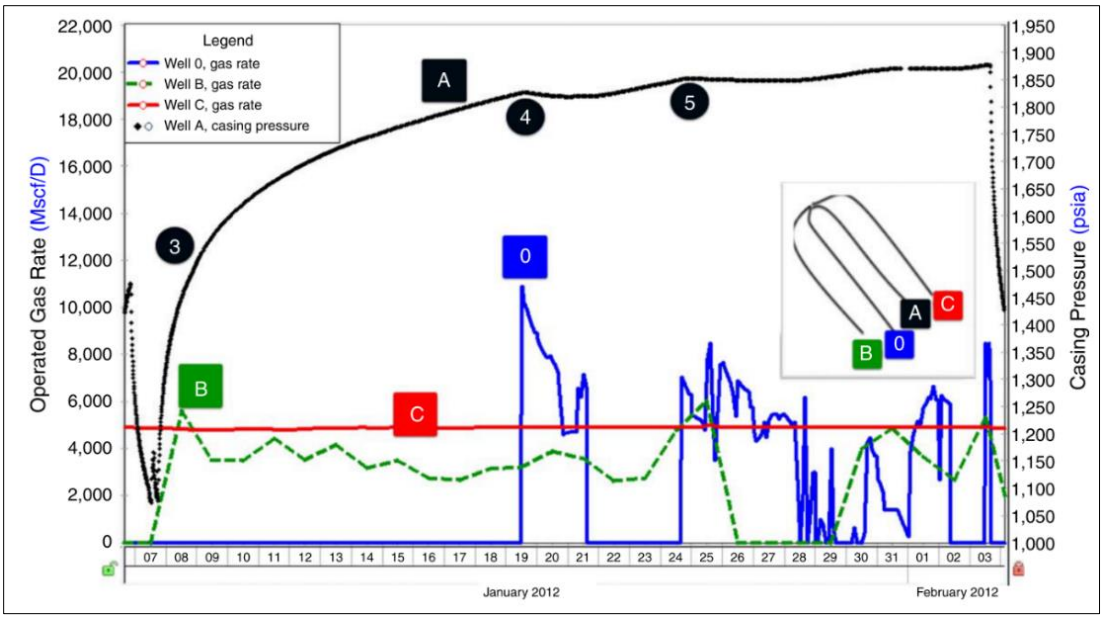

Figure 7.1: Pressure interference between Well 0 and well A (Awada et al., 2015)

Fracture connectivity between wells is reflected in fluid and tracer transport in a fractured reservoir. Chemical fluid tracers have been used for evaluating the extent of fracture communication with offset wells (Mulkern et al., 2010), estimating fracture volume between well pairs (Leong et al., 2015), and diagnosing fracture wellbore connectivity (Kumar and Sharma 2018). However, fracture connectivity can change due to fracture closure because of in-situ stress changes during flowback and production (Seth *et al.*, 2018; Kumar *et al.*, 2018). Due to fracture closure over time, well interference is time-dependent, and only analyzing fluid tracer can lead to erroneous conclusions. Fracture connectivity is a function of proppant distribution during stimulation. Radioactive proppant tracers (sand coated with radioactive materials) can provide information about the proppant distribution around wellbores (Liang et al., 2016). Combining fluid tracer data with proppant tracer data provides useful information on fracture connectivity between wells.

The impact of stimulation sequence and the extent, onset and duration of interference observed is described in this chapter using a data set obtained at the Hydraulic Fracturing Test Site (HFTS) (Courtier *et al.*, 2017).

7.2 FIELD INFORMATION

At the HFTS, chemical fluid tracer, radioactive proppant tracer, and pressure interference data were collected by Laredo Petroleum for 11-wells in the Permian Basin.

7.2.1 Methodology

Chemical fluid tracers were injected during the pad and proppant stage of the fracturing treatment. Produced water samples were collected and analyzed to estimate tracer concentration. Radioactive proppant tracers were injected with the proppant stage of the fracturing treatment. Near-wellbore proppant concentration is estimated by running a spectrum gamma-ray log. HFTS tracer test methodology is provided in detail in Wood *et al.* (2018). A pressure interference test was conducted after eight months of production.

7.2.2 Well Configuration and Stimulation Sequence

The well configuration is shown in Figure 7.2 using a gun-barrel view. The upper layer (Upper Wolfcamp) comprises six wells (UWC1-UWC6) separated by 660 feet, and the lower layer (Middle Wolfcamp) has five wells (MWC1-MWC5) spaced 660 feet apart. The vertical distance between the UWC and MWC layers is 325 feet, and the wells in the lower layer are chevroned 330 feet horizontally offset to UWC wells. The well stimulation sequence is shown in Figure 7.3. The eight wells were zipper fractured in pairs. The remaining three wells were zipper fractured as a triplet. The text under the arrows

represents the order of stimulation, with ZF-1 being the first well-pair stimulated and ZF-5 being the last. More information about the wells can be found in Courtier et al. (2017).

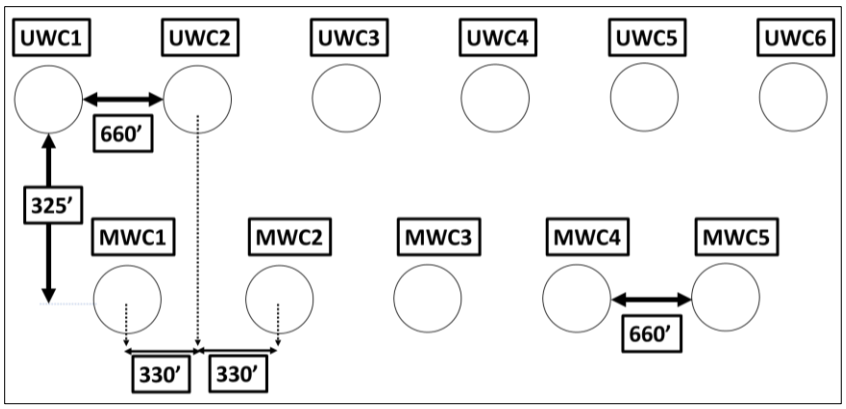

Figure 7.2: Well configuration showing UWC and MWC wells (circles) using a gun-barrel view. MWC wells are 325 feet deeper and chevroned 330 feet horizontally offset to UWC wells.

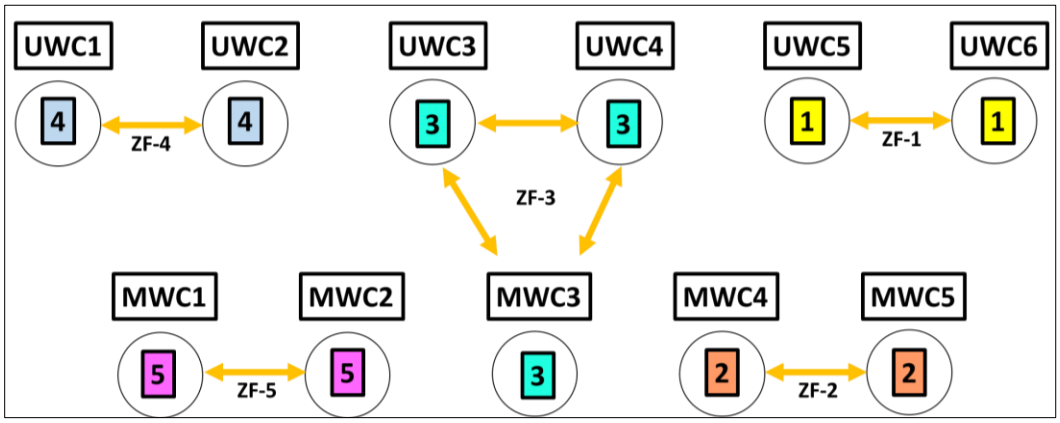

Figure 7.3: Well stimulation sequence, ZF denotes zipper fracturing

7.3 FIELD OBSERVATIONS AND ANALYSIS

7.3.1 Fluid Tracer Test Analysis

Water-soluble chemical fluid tracers were injected in 8 of the 11 wells. All stages in a well were clubbed and divided into three/four zones, and a different unique tracer was injected in each zone. These chemical fluid tracers are water-soluble and will remain only in the water phase. Produced water samples were analyzed (gas chromatography/ mass spectrometry) to estimate the fluid tracer concentration. Tracer injected at a well can be observed at other offset wells, and the concentration of each tracer was monitored at all wells on daily basis. Using the tracer concentration and water rates from field reports, we calculated the volume of tracer recovered at each observation well as shown in Figure 7.4. For a given tracer injection well, observed tracer volume recovered was normalized to calculate the relative percentage recovery (Figure 7.5) at each observation well to quantify the degree of communication between interacting wells.

		Observation Well										
		UWC1	MWC1	UWC2	MWC2	UWC3	MWC3	UWC4	MWC4	UWC5	MWC5	UWC6
Injected Well	UWC1	0	0	0	0	0	0	0	0	0	0	0
	MWC1	0.005083	0.006818	0.003553	0.00272	0.001685	0.002236	0.000543	0.00135	8.57E-05	0.000425	1.89E-06
	UWC2	0.001011	0.000125	0.002699	6.37E-05	0.000679	3.51E-05	3.16E-05	1.65E-06	6.23E-06	0	0
	MWC2	0	0	0	0	0	0	0	0	0	0	0
	UWC3	0	0	0	0	0	0	0	0	0	0	0
	MWC3	3.59E-05	0.000485	6.35E-05	0.000578	0.000907	0.00256	0.000907	0.000997	0.000146	0.000651	0.000149
	UWC4	0	0	3.43E-06	1.56E-05	0.000214	8.45E-05	0.001623	0.000152	0.000229	3.04E-06	2.13E-06
	MWC4	0	2.28E-05	8.26E-06	9.13E-05	0.000246	0.001651	0.001844	0.003956	0.001598	0.003005	0.000595
	UWC5	0	0	0	0	0	0	3E-05	2.03E-06	0.00107	6.79E-06	0.000262
	MWC5	6.44E-07	9.49E-05	8.63E-06	0.000178	0.000267	0.001368	0.000877	0.001624	0.001981	0.003779	0.002541
	UWC6	0	0	0	0	0	0	0	2.29E-06	0.000206	3.72E-05	0.001569

Figure 7.4: Inter-well fluid tracer communication table for HFTS wells based on absolute tracer volume recovered at each observation well. Data color bars scale with the relative tracer recovery at the observation well.

Injected Well \ Observation Well	UWC1	MWC1	UWC2	MWC2	UWC3	MWC3	UWC4	MWC4	UWC5	MWC5	UWC6
UWC1											
MWC1	20.7	27.8	14.5	11.1	6.9	9.1	2.2	5.5	0.3	1.7	0.0
UWC2	21.7	2.7	58.0	1.4	14.6	0.8	0.7	0.0	0.1	0.0	0.0
MWC2											
UWC3											
MWC3	0.5	6.5	0.8	7.7	12.1	34.2	12.1	13.3	2.0	8.7	2.0
UWC4	0.0	0.0	0.1	0.7	9.2	3.6	69.8	6.5	9.8	0.1	0.1
MWC4	0.0	0.2	0.1	0.7	1.9	12.7	14.2	30.4	12.3	23.1	4.6
UWC5	0.0	0.0	0.0	0.0	0.0	0.0	2.2	0.1	78.0	0.5	19.1
MWC5	0.0	0.7	0.1	1.4	2.1	10.8	6.9	12.8	15.6	29.7	20.0
UWC6	0.0	0.0	0.0	0.0	0.0	0.0	0.0	0.1	11.3	2.1	86.5

Figure 7.5: Inter-well fluid tracer communication table for HFTS wells based on percentage tracer recovered at each observation well. Data color bars scale with the relative percentage tracer recovery at the observation well.

We also computed the time-weighted average tracer concentration for all fluid tracers at all wells during the first three months of flowback/production. A well had three/four tracer injected and for inter-well communication analysis, we combined those three/four tracers by averaging the concentration of tracers injected at a well. This average tracer concentration at each well was normalized on a scale of integer values (0 to 10) based on the minimum and maximum tracer concentration observed. Figure 7.6 shows a summary of these averaged fluid tracer results for all wells using a gun-barrel view. Each sub-figure represents an inter-well tracer test for a specific tracer injected in a well (enclosed by a square) and normalized tracer concentration observed at all the wells. The numbers (and

the color) on the well represent the normalized tracer concentration at that well during flowback. The white color at a well represents that the tracer was not recovered at that well.

Important observations based on fluid tracer analysis:

- Tracer injected at well UWC4 has a higher concentration at wells UWC5, UWC6, MWC4, MWC5 as compared to wells UWC1, UWC2, MWC1, and MWC2 (Figure 7.6-b). Similar examples are shown for tracer injected at well UWC5 (Figure 7.6-c) and MWC3 (Figure 7.6-f). These observations suggest that more fluid tracer is recovered from previously fractured wells. This is because fluid travels easily through the pre-existing fracture network from previous stimulations. In some instances, connectivity between all previously fractured wells is observed (Figure 7.6-e). This indicates that the previously created fracture network can extend thousands of feet away from the wellbore, at least during the early life of the well.
- Tracer injected at well UWC2, UWC5 and MWC3 has a higher concentration at the corresponding zipper fractured wells UWC1, UWC6, and UWC3-UWC4 as compared to the nearby wells at a similar distance. These observations suggest that zipper fractured wells show better tracer communication. This may be due to the fact that the time between two successive fractures created in the two zippered wells is short, and the induced unpropped fractures have not closed over this short time. These zipper fractured wells can potentially create comingled fracture networks. This network can allow the chemical fluid tracers to travel between the zippered wells.

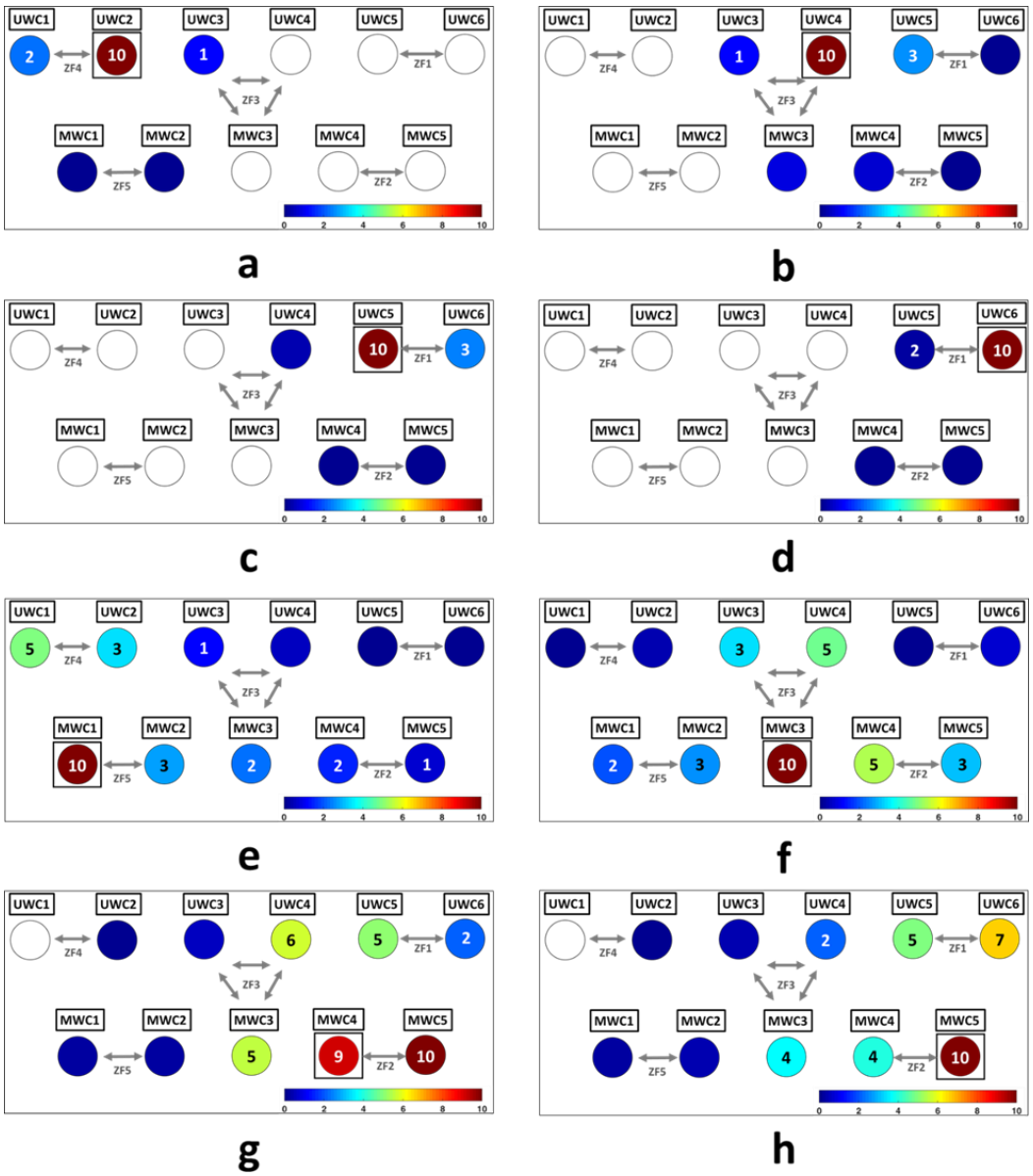

Figure 7.6: Water-soluble chemical fluid tracer analysis during flowback/production. Each sub-figure represents an inter-well tracer test response with different unique chemical fluid tracers injected in a well (enclosed by a square) and observed at all wells. The numbers on the well (and the color) represents the normalized tracer concentration at that well (high numbers indicate more tracer observed).

7.3.2 Proppant Tracer (Radioactive Tracer) Tests Analysis

Radioactive (RA) tracers were pumped in wells UWC2, UWC4, and MWC3. These wells along with offset wells were logged to determine the proppant distribution around the wells. Figure 7.7 shows the RA tracer distribution at each well. Red, blue, and yellow colors represent Iridium, Antimony, and Scandium RA tracers respectively.

Important observations based on RA tracer analysis:

- RA tracers have a higher tendency to stay close to the wellbore as compared to the fluid tracer. This is because RA tracers are tagged on the proppant, and proppant generally does not travel as far as the fluid due to the tortuous path in a complex fracture network.
- Wells that are zipper fractured show better communication than adjacent wells that were previously fractured. We postulate that this is due to the time-dependent closure of induced unpropped fractures (Manchanda et al., 2014). For example, Well UWC3 was fractured and shut-in for ~15 days before wells UWC2-UWC1 were zipper fractured. The RA tracer from well UWC2 did not show up near well UWC3 because the fracture network created by the stimulation of well UWC3 had probably closed before the stimulation of well UWC2 was started.
- During the zipper fracturing of wells UWC-3, UWC-4, and MWC-3, we see that the proppant tracer injected in MWC3 is observed in UWC3 and UWC4. This indicates transport of proppant between the Middle Wolfcamp and Upper Wolfcamp during fracturing and suggests that the frac barrier between the two formations is ineffective in containing fractures created in the middle Wolfcamp wells.

- Proppant tracer from previous stimulations is observed in newly stimulated wells. This indicates the creation of at least a few long, dominant fractures.

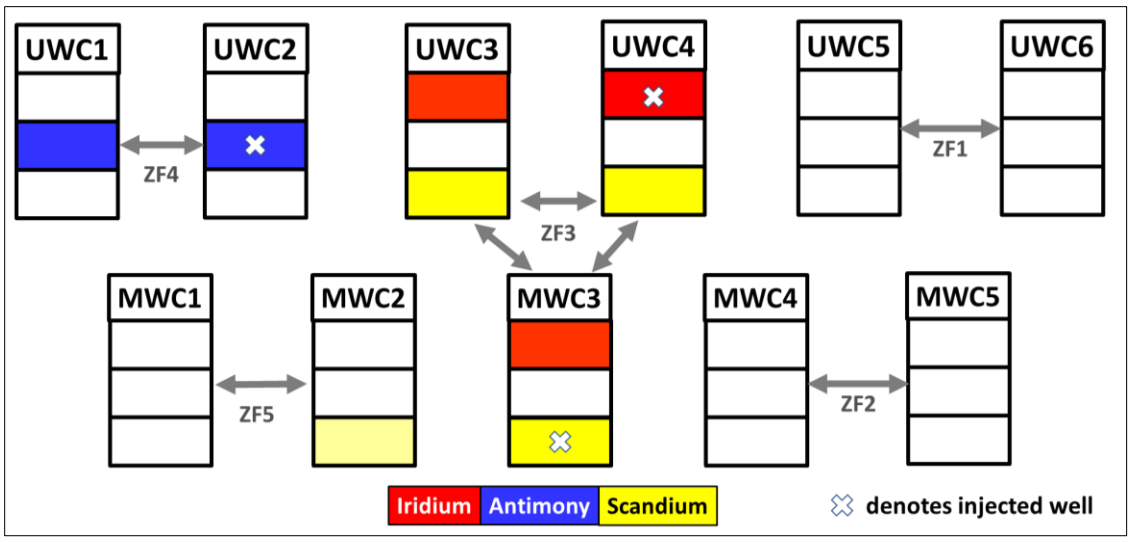

Figure 7.7: Proppant communication between wells based on radioactive tracer (Red: Iridium; Blue: Antimony; Yellow: Scandium) presence at each well. Cross mark denotes the well where the RA tracer was injected.

Pressure interference tests were conducted by Laredo Petroleum approximately eight months after production was commenced. Bottomhole pressure gauges were used to record high-resolution pressure data for all wells during pressure interference testing. The pressure response observed in all the wells is shown in Figure 7.8. As seen in Figure 7.8, sudden rate changes (shut-in or restarts) in source wells causes a change in the pressure build-up response at the monitor wells. Figure 7.8 shows four pressure interference events with the help of arrows (monitor well) and stars (source well). Field data shows pressure interference between well pairs UWC1-UWC2 (event-1), UWC3-UWC4 (event-3), MWC2-MWC3 (event-2), and MWC3-MWC4 (event-4).

Approximate travel time for the pressure pulse to reach the monitor well is defined as the response time. Response time can also be interpreted as the time-lag following a sudden rate change in the source well, after which the pressure build-up profile at the monitor well changes. Figure 7.9 summarizes the pressure interference observed between all UWC and MWC wells. Green arrows represent an apparent interference observed, while yellow arrows represent possible communication. The numbers beneath the arrow represent response time. A lower response time signifies stronger communication between wells. The response time observed for all the field cases that show pressure interference was in the range of one to two hours.

Here are some of the important observations based on correlating pressure interference test with pressure interference test:

- Wells that show RA tracer (proppant) communication (UWC1-UWC2 and UWC3-UWC4) are much more likely to show pressure communication with each other in the same layer. This indicates that the propped fractures remain open and are, therefore, primarily responsible for pressure communication.
- Pressure communication (after ~200 days of production) is not directly correlated with the interference obtained from inter-well fluid tracer data. Figure 7.6-e to 7.6-h show fluid tracer communication among all the wells, but only a few well pairs show pressure communication. This indicates that the hydraulically conductive fracture pathways created during stimulation may close during production.
- Pressure interference (after ~200 days of production) between Upper and Middle Wolfcamp is not observed even for zipper fractured wells even though strong fluid tracer and proppant tracer (radioactive) exchange is observed. This indicates post fracturing closure of connected pathways. A possible reason for such loss of

connectivity may be due to the formation of disconnected proppant banks between layers (Shrivastava and Sharma, 2018).

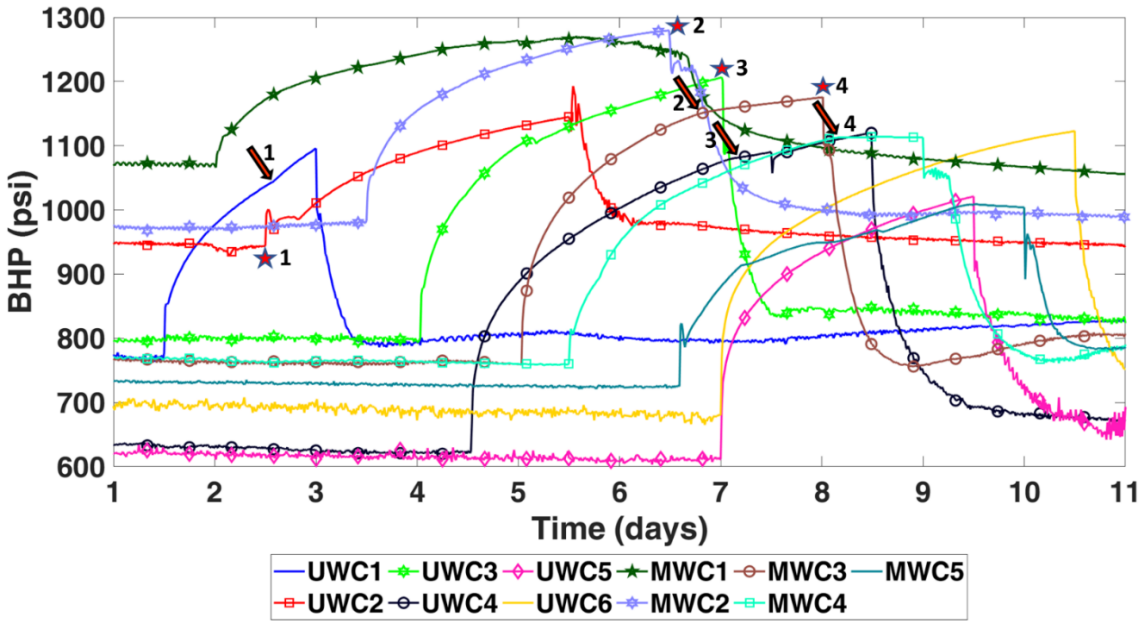

Figure 7.8: Bottomhole pressure monitored in 11 wells during pressure interference testing. Arrows in the figure represent pressure interference events at the monitor well corresponding to a source well which is shown by a star.

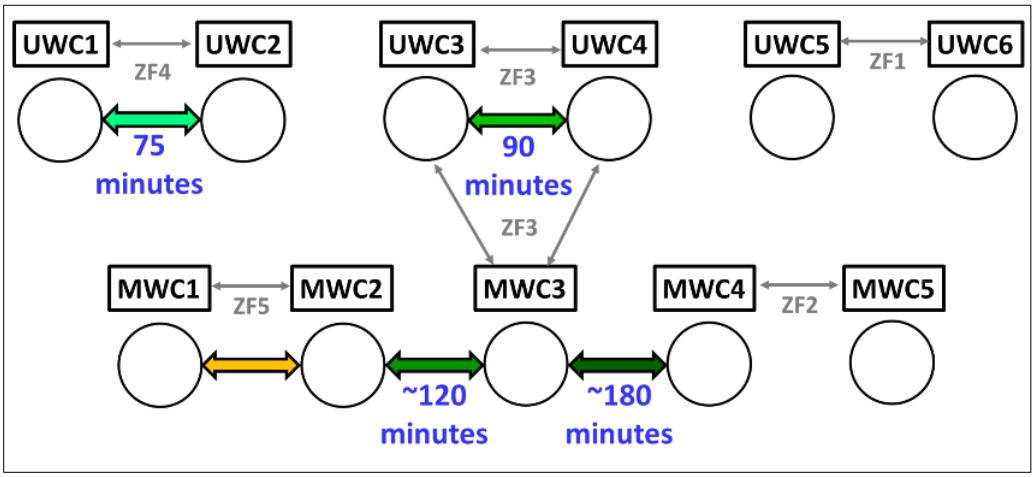

Figure 7.9: Summary of pressure interference test. Arrows represent interference between well pairs, and the corresponding number is the response time in minutes.

7.4 Summary And Discussion

Important observations from the three diagnostic methods are summarized in Table 7.2.

Table 7.2: Well interference diagnostic results summary

Chemical Fluid Tracer Tests	**Radioactive Proppant Tracer Test**	**Pressure Interference Test**
Fluid tracers travel easily through the pre-existing fractures.	Proppant tracers generally do not travel as far as the fluid tracers travel.	Pressure interference correlates well with proppant tracer communication.
All previously fractured wells showed a tracer response (direct frac communication), not just nearest neighbors. This suggests that direct fracture connection exists between all wells during the early life of the well.	Zipper fractured wells show better proppant communication.	Well communication as indicated by strong fluid tracer and proppant tracer exchange is not observed during pressure interference testing. This suggests the possibility of closure of connecting fracture pathways.

Fluid tracer transport between the wells shows a clear connection between the created fracture networks originating from multiple wells during the hydraulic fracturing process. These channels (fracture network) can provide pathways for the fluid to escape to regions near pre-fractured wells. As the path of connectivity is expected to have a reduced width (due to fluid leak-off in the pre-existing fracture network and pressure drop across tortuous pathways), the likelihood of the proppant transport in these regions is small. This can lead to the generation of unpropped fracture networks. Unpropped fracture closure is evident from the absence of pressure communication between the wells after a few months of production. During pressure interference testing, the pressure in the fracture network is well below the far-field stresses. This makes it unlikely for the closed fracture networks to reopen and regain lost connectivity. In addition, the pressure connectivity is observed to be strong between the wells that exhibited an exchange of proppant tracer. It is observed that this proppant exchange is very likely to happen between zipper fractured wells. This signifies the commingled nature of the fracture network generated during the zipper fracturing process. The creation of this commingled fracture network should be accounted for while deciding on well spacing and infill well drilling for zipper fractured wells, as the network between zipper fractured wells is more likely to be propped and contributing to production. It is also observed that zipper fracturing between different layers does not result in pressure connectivity, indicating the disconnected nature of the fracture networks (after production) despite the commingled nature of the IU fracture network. It is possible that proppant settling plays an important role in inducing this behavior. This study enhances our understanding of the geometry of the fracture network and clearly shows dynamic fracture closure due to production. Pressure interference can, therefore, be useful for deciding the locations of infill wells and well spacing.

7.5 CONCLUSIONS

In this chapter, we presented an integrated analysis of chemical fluid tracer, proppant tracer and pressure interference test analysis from an 11 well pad in Permian basin to understand well communication. Important conclusions from this chapter are summarized below.

7.5.1 Conclusions based on Fluid and Proppant Tracer Tests

- Fluid tracers travel much further than the proppant tracer. Fluid tracer recovery at multiple offset wells indicates frac-hits during stimulation.
- Fluid tracer recovery is higher at previously fractured wells. This is because fluid can travel more easily through the pre-existing fracture network.
- Zipper fractured wells show better communication between each other as compared to adjacent wells that were previously fractured. This is most likely due to the closure of induced unpropped fractures resulting from the time delay between the creation of fractures in previously fractured wells.
- Proppant tracer exchange between Middle and Upper Wolfcamp is observed during zipper fracturing. This suggests that the frac barrier layer between the two formations allows fracture breakthrough from middle Wolfcamp wells.
- Proppant tracer from previous stimulations in newly stimulated wells indicates the creation of at least a few long, dominant fractures.

7.5.2 Integrating Pressure Responses with Tracer Responses

- In a layer, wells that show proppant tracer exchange are much more likely to show pressure communication with each other. This pressure communication can be due

to the propped fractures that remain open at the time of pressure interference testing.

- Interference obtained from inter-well water-soluble tracer data does not correlate with inter-well pressure communication observed after ~200 days of production. This indicates the possibility of induced unpropped fracture closure during this period of production.
- Connectivity between the Upper and Middle Wolfcamp wells, as indicated by strong fluid tracer and proppant tracer exchange, is not observed during pressure interference testing (after ~200 days of production). This indicates the possibility of post-fracture closure of connecting fracture pathways between the two layers due to proppant settling.

Chapter 8: Conclusions and Future Work

8.1 CONCLUSIONS

This dissertation's primary objectives were to develop a geomechanical reservoir simulation model to analyze the productivity of wells producing from complex fracture networks and then utilize chemical tracer tests to diagnose fracture wellbore connectivity and well interference.

Important conclusions from each chapter are summarized in the following sections.

8.1.1 Model development for complex fracture networks (Chapter 2)

i. A geomechanics coupled reservoir simulation model was developed to simulate production from complex fracture networks. The model can capture the fracture closure effects during depletion.
ii. An automated meshing methodology was developed to generate finite-volume mesh around any given arbitrarily shaped complex fracture network.
iii. Tracer transport was incorporated in the model to simulate tracer injection and flowback coupled with fracture propagation and closure.
iv. We developed an adaptive time-stepping scheme coupled with an output time series to conduct large time scale simulations efficiently.
v. The model was verified and validated for production and tracer transport simulations.

8.1.2 Optimizing drawdown strategies in well producing from complex fracture networks (Chapter 3)

i. We observed that fracture closure can disconnect a significant fraction of the created fracture area from the wellbore, leading to a sharp decline in production rates.
ii. In 3D fracture networks, the smaller fracture width near the intersection of hydraulic fracture and natural fracture acts as a bottleneck for flow from the fracture network to the wellbore.
iii. Improper drawdown strategy can lead to the early closure of the fracture connections and can affect well productivity.
iv. Optimum drawdown strategy was calculated based on NPV maximization.

8.1.3 Effective permeability estimation for complex fracture networks (Chapter 4)

i. We developed a workflow to estimate the effective permeability of the activated natural fracture region around the hydraulic fracture.
ii. The impact of natural fracture orientation on the created SRV was analyzed. Negligible shear failure of the natural fractures was observed when natural fractures are oriented at a low angle from maximum stress direction.
iii. We observed that once the depletion pressure front reaches the activated natural fractures, the rate decline slope is reduced due to the production contribution from the SRV.
iv. The spatial extent of the SRV increases with an increase in the propagating fracture height.

v. The calculated effective permeability of the complicated fracture network can be used in upscaled traditional reservoir simulation models.

8.1.4 Effect of parent well production on child well stimulation and productivity (Chapter 5)

i. We observed that the interconnected nature of infill timing, well spacing, and reservoir diffusivity has a significant impact on the well performance of parent and child wells.
ii. Overlap in the drainage area of the parent well and child well fractures lead to a decrease in the overall production from parent and child wells.
iii. Parent well production can have a positive or negative impact due to child well fracturing depending upon the well operating conditions.
iv. The impact of parent well depletion on child well cumulative production increases with decreasing well spacing, longer times before infill drilling, and smaller hydraulic diffusivity.

8.1.5 Diagnosing fracture wellbore connectivity using tracer flowback (Chapter 6)

i. Geomechanics coupled fluid flow and tracer transport model was used to analyze the impact of (a) fracture geometry, (b) fracture propagation and closure effects, and (c) fracture complexity on the tracer response curves.
ii. Tracer injection and flowback in a complex fracture network were modeled with the help of an effective model. The closure of activated natural fractures can explain multiple peaks in the tracer response curves.
iii. Low tracer recovery typically observed in field tests can be explained by tracer retention due to fracture closure.

iv. In a complex fracture network, segment length and permeability were lumped to define an effective connected fracture length, a parameter that correlates with production. Neural network-based inverse modeling was performed to estimate effective connected fracture length using chemical tracer flowback data.

8.1.6 Integrated analysis of tracer and pressure interference tests to identify well interference (Chapter 7)

i. Chemical tracer, radioactive proppant tracer, and pressure interference observations were integrated to understand the well communication for Hydraulic Fracturing Test Site # 1.

ii. Difference between early time and late time well communication was explained based on the well stimulation sequence and delay between fracturing.

iii. We observed that zipper fracturing wells have better proppant communication than the adjacent wells that were previously fractured.

iv. Created fracture networks can extend thousands of feet away from the wellbore, at least during the early life of the well.

v. Well communication observed based on pressure interference (conducted after ~200 days of production) does not correlate with fluid tracer observations. This suggests the possibility of closure of the connecting fracture pathways.

8.2 RECOMMENDATIONS FOR FUTURE RESEARCH

- In this research, we used a displacement discontinuity method based model (Shrivastava and Sharma, 2018a) for complex fracture propagation, and then flowback/production was simulated in the developed model. This explicit workflow can be improved by simulating complex fracture propagation and flowback in a single model. This will require fracture propagation using unstructured mesh and updating the mesh after each failure iteration.
- The unstructured meshing algorithm can be implemented in the general framework of Multi-Frac-3D (Zheng et al., 2019b) to solve compositional and black oil reservoir simulations in complex fractures.
- The effect of bubble point and the dew point was not considered during drawdown strategy optimization. In the case of multiphase flow in the reservoir, if the pressure in the wellbore drops below the bubble point pressure, then gas will come out of the solution in oil. Similarly, in the case of gas condensate reservoirs, below dew point pressure, liquid may drop out of the reservoir. This drop in the oil or gas flow can affect the production performance of the well; hence the effect of bubble point and dew point should be considered in future research.
- A wellbore flow model can be coupled with the developed model to improve drawdown optimization and tracer flowback analysis.
- Tracer adsorption can be incorporated in the tracer transport equations to analyze tracer retention on rock surfaces.
- Parent-child well interference analysis can be extended for naturally fractured reservoirs. Pore pressure changes due to the depletion of the parent well can affect the shear failure of natural fractures during child well fracturing. Also, the

presence of natural fractures may cause frac-hits during child well fracturing. These phenomena can help in explaining the positive or negative well interference behavior (Miller et al., 2016) in different shale plays.

References

Agca, C., Pope, G.A., Sepehrnoori, K., 1990. Modelling and analysis of tracer flow in oil reservoirs. J. Pet. Sci. Eng. 4, 3–19. https://doi.org/10.1016/0920-4105(90)90042-2

Agrawal, S., Sharma, M.M., 2018. Impact of Pore Pressure Depletion on Stress Reorientation and its Implications on the Growth of Child Well Fractures. 6th Unconv. Resour. Technol. Conf. https://doi.org/10.15530/urtec-2018-2875375

Agrawal, S., Shrivastava, K., Sharma, M.M., 2019. Effect of Shear Slippage on the Interaction of Hydraulic Fractures with Natural Fractures, in: SPE Hydraulic Fracturing Technology Conference and Exhibition. Society of Petroleum Engineers. https://doi.org/10.2118/194361-MS

AlTammar, M.J., Sharma, M.M., Manchanda, R., 2018. The Effect of Pore Pressure on Hydraulic Fracture Growth: An Experimental Study. Rock Mech. Rock Eng. 51, 2709–2732. https://doi.org/10.1007/s00603-018-1500-7

ASADI, M., WOODROOF, R.W., MALONE, W.S., SHAW, D.R., PROTECHNICS, CORP, P.O.I.L.& G.A.S., 2002. Monitoring Fracturing Fluid Flowback With Chemical Tracers: a Field Case Study. Annu. Spe Tech. Conf. (San Antonio, Tx, 9/29/2002-10/2/2002) Proc.

Awada, A., Santo, M., Lougheed, D., Xu, D., Virues, C., 2015. Is That Interference? A Workflow for Identifying and Analyzing Communication Through Hydraulic Fractures in a Multi-Well Pad. Proc. 3rd Unconv. Resour. Technol. Conf. https://doi.org/10.15530/urtec-2015-2148963

Bandis, S.C., Lumsden, A.C., Barton, N.R., 1983. Fundamentals of rock joint deformation. Int. J. Rock Mech. Min. Sci. 20, 249–268. https://doi.org/10.1016/0148-9062(83)90595-8

Barree, R.D., 2015. Stress Shadowing and Fracture Interference in GOHFER ®.

Barree, R.D., Mukherjee, H., 1995. Engineering Criteria for Fracture Flowback Procedures, in: SPE Rocky Mountain RagionaULow-PermeafNii Reaamoire Symposium Held. Denver.

Bhardwaj, P., Manchanda, R., Hwang, J., Cardiff, P., Sharma, M.M., 2016. A new reservoir scale model for fracture propagation and stress reorientation in injection wells, 50th US Rock Mechanics / Geomechanics Symposium 2016. American Rock Mechanics Association.

Brenner, H., 1962. The diffusion model of longitudinal mixing in beds of finite length. Numerical values. Chem. Eng. Sci. 17, 229–243. https://doi.org/10.1016/0009-2509(62)85002-7

Bryant, E.C., 2016. Hydraulic fracture modeling with finite volumes and areas.

Bryant, E.C., Hwang, J., Sharma, M.M., 2015. Arbitrary Fracture Propagation in Heterogeneous Poroelastic Formations Using a Finite Volume-Based Cohesive Zone Model, in: SPE Hydraulic Fracturing Technology Conference. pp. 3–5. https://doi.org/10.2118/173374-MS

Cardiff, P., Manchanda, R., Ivanković, A., Bryant, E.C., Lee, D., Sharma, M.M., 2015. Simulation of Fractures in OpenFOAM: From Adhesive Joints to Hydraulic Fractures, in: 10th OpenFOAM Workshop. p. 2015.

https://doi.org/10.13140/RG.2.1.1514.1203.

Cipolla, C., Wallace, J., 2014. Stimulated Reservoir Volume: A Misapplied Concept? SPE Hydraul. Fract. Technol. … 4–6. https://doi.org/10.2118/168596-MS

Cipolla, C.L., Warpinski, N.R., Mayerhofer, M.J., 2010. Hydraulic fracture complexity: Diagnosis, remediation, and exploitation, in: Society of Petroleum Engineers - International Oil and Gas Conference and Exhibition in China 2010, IOGCEC. pp. 34–57. https://doi.org/10.2118/115771-ms

Cook, Troy; Perrin, Jack; Wagener, D. Van, 2018. Hydraulically fractured horizontal wells account for most new oil and natural gas wells [WWW Document]. U.S. Energy Inf. Adm. URL https://www.eia.gov/todayinenergy/detail.php?id=34732 (accessed 7.7.20).

Courant, R., Friedrichs, K., Lewy, H., 1928. On the Partial Difference Equations of Mathematical Physics, IBM Journal of Research and Development. https://doi.org/10.1147/rd.112.0215

Courtier, J., Ciezobka, J., Chandler, K., Martin, S., Thomas, R., 2017. Best Practices in Designing and Executing a Comprehensive Hydraulic Fracturing Test Site in the Permian Basin. Proc. 5th Unconv. Resour. Technol. Conf. 24–26. https://doi.org/10.15530/urtec-2017-2697483

Courtier, J., Gray, D., Smith, M., Petroleum, L., Stegent, N., Carmichael, J., Hassan, M., Ciezobka, J., 2016. Legacy well protection refrac mitigates offset well completion communications in joint industry project, in: Society of Petroleum Engineers - SPE Liquids - Rich Basins Conference - North America 2016. pp. 1–18.

Crouch, S.L., Starfield, A.M., Rizzo, F.J., 1983. Boundary Element Methods in Solid Mechanics. J. Appl. Mech. 50, 704. https://doi.org/10.1115/1.3167130

Dawson, M., Kampfer, G., 2016. Breakthrough in Hydraulic Fracture & Proppant Mapping: Achieving Increased Precision with Lower Cost. Proc. 4th Unconv. Resour. Technol. Conf. 1–3. https://doi.org/10.15530/urtec-2016-2432330

Du, Y., Guan, L., 2005. Interwell Tracer Tests : Lessons Learned From Past Field Studies. SPE Asia Pacific Oil Gas Conf. Exhibtion, Jakharta, Indones. April 5-7 1–9. https://doi.org/10.2118/93140-MS

Erdogan, F., Sih, G.C., 1963. On the Crack Extension in Plates Under Plane Loading and Transverse Shear. J. Basic Eng. 85, 519. https://doi.org/10.1115/1.3656897

Fisher, M.K., Heinze, J.R., Harris, C.D., Davidson, B.M., Wright, C.A., Dunn, K.P., 2004. Optimizing Horizontal Completion Techniques in the Barnett Shale Using Microseismic Fracture Mapping, SPE Annual Technical Conference and Exhibition. https://doi.org/10.2118/90051-MS

Fisher, M.K., Wright, C.A., Davidson, B.M., Goodwin, A.K., Fielder, E.O., Buckler, W.S., Steinsberger, N.P., 2002. Integrating Fracture Mapping Technologies to Optimize Stimulations in the Barnett Shale. SPE Annu. Tech. Conf. Exhib. https://doi.org/10.2118/77441-MS

Fredd, C.N., McConnell, S.B., Boney, C.L., England, K.W., 2000. Experimental Study of Hydraulic Fracture Conductivity Demonstrates the Benefits of Using Proppants. SPE Rocky Mt. Reg. Reserv. Symp. Exhib. https://doi.org/10.2118/60326-MS

Gale, J.F.W., Elliott, S.J., Laubach, S.E., 2018. Hydraulic fractures in core from stimulated

reservoirs: Core fracture description of HFTs slant core, Midland Basin, West Texas, in: SPE/AAPG/SEG Unconventional Resources Technology Conference 2018, URTC 2018. Unconventional Resources Technology Conference (URTEC). https://doi.org/10.15530/urtec-2018-2902624

Gardien, C.J., Pope, G.A., Hill, A.D., 1996. Hydraulic Fracture Diagnosis Using Chemical Tracers (SPE 36675). SPE Annu. Tech. Conf. Exhib. held Denver, Color. 925–932.

Goswick, R.A., Corp, A., Larue, J.L., 2014. SPE-170929-MS Utilizing Oil Soluble Tracers to Understand Stimulation Efficiency Along the Lateral 27–29. https://doi.org/10.2118/170929-MS

Guo, X., Wu, K., Killough, J., 2018. Investigation of production-induced stress changes for infill-well stimulation in eagle ford shale, in: SPE Journal. Society of Petroleum Engineers, pp. 1372–1388. https://doi.org/10.15530/urtec-2017-2670745

Hajibeygi, H., Karvounis, D., Jenny, P., 2011. A hierarchical fracture model for the iterative multiscale finite volume method. J. Comput. Phys. 230, 8729–8743. https://doi.org/10.1016/j.jcp.2011.08.021

Hakim Elahi, S., Jafarpour, B., 2015. Characterization of Fracture Length and Conductivity From Tracer Test and Production Data With Ensemble Kalman Filter. Unconv. Resour. Technol. Conf. 1192–1200. https://doi.org/10.2118/178707-MS

Jacobs, T., 2017. Oil and Gas Producers Find Frac Hits in Shale Wells a Major Challenge. J. Pet. Technol. 69, 29–34. https://doi.org/10.2118/0417-0029-jpt

Jeffrey, R.G., Settari, A., Smith, N.P., 1995. Comparison of hydraulic fracture field experiments, including mineback geometry data, with numerical fracture model

simulations, in: Proceedings - SPE Annual Technical Conference and Exhibition. pp. 591–606.

Jin, M., Delshad, M., Dwarakanath, V., McKinney, D.C., Pope, G.A., Sepehrnoori, K., Tilburg, C.E., Jackson, R.E., 1995. Partitioning Tracer Test for Detection, Estimation, and Remediation Performance Assessment of Subsurface Nonaqueous Phase Liquids. Water Resour. Res. 31, 1201–1211. https://doi.org/10.1029/95WR00174

Johnston, P.B., Atkinson, T.C., Odling, N.E., Barker, J.A., 2005. Models of tracer breakthrough and permeability in simple fractured porous media. Geol. Soc. London, Spec. Publ. 249, 91–102. https://doi.org/10.1144/GSL.SP.2005.249.01.08

Karantinos, E., Sharma, M.M., Ayoub, J.A., Parlar, M., Chanpura, R.A., 2016. Choke Management Strategies for Hydraulically Fractured Wells and Frac–Pack Completions in Vertical Wells. SPE Int. Conf. Exhib. Form. Damage Control. https://doi.org/10.2118/178973-MS

Karimi-Fard, M., Durlofsky, L.J., Aziz, K., 2004. An Efficient Discrete Fracture Model Applicable for General Purpose Reservoir Simulators. SPE Journal, SPE-88812-PA 9, 227–236. https://doi.org/10.2118/79699-MS

King, G.E., Leonard, D., 2011. Utilizing Fluid and Proppant Tracer Results to Analyze Multi-Fractured Well Flow Back in Shales: A Framework for Optimizing Fracture Design and Application. SPE Hydraul. Fract. Technol. Conf. Exhib. Woodlands, Texas, USA, 24-26 January 2011. https://doi.org/10.2118/140105-MS

King, G.E., Rainbolt, M.F., Swanson, C., 2017. Frac hit induced production losses: Evaluating root causes, damage location, possible prevention methods and success of

Remedial treatments. Proc. - SPE Annu. Tech. Conf. Exhib. https://doi.org/10.2118/187192-ms

Kumar, A., Seth, P., Shrivastava, K., Manchanda, R., Mukul, M., Engineering, G., 2018a. Well Interference Diagnosis through Integrated Analysis of Tracer and Pressure Interference Tests. https://doi.org/10.15530/urtec-2018-

Kumar, A., Seth, P., Shrivastava, K., Manchanda, R., Sharma, M.M., 2018b. Well interference diagnosis through integrated analysis of tracer and pressure interference tests, in: SPE/AAPG/SEG Unconventional Resources Technology Conference 2018, URTC 2018. Unconventional Resources Technology Conference (URTEC). https://doi.org/10.15530/urtec-2018-2901827

Kumar, A., Seth, P., Shrivastava, K., Sharma, M.M., 2018c. Optimizing Drawdown Strategies in Wells Producing from Complex Fracture Networks, in: SPE International Hydraulic Fracturing Technology Conference and Exhibition. Muscat, Oman. https://doi.org/10.2118/191419-18IHFT-MS

Kumar, A., Sharma, M.M., Engineering, P., States, U., 2018d. Diagnosing Fracture-Wellbore Connectivity Using Chemical Tracer Flowback Data 1–11. https://doi.org/10.15530/urtec-2018-2902023

Lake, L., 1996. Enhanced oil recovery. Society of Petroleum Engineers.

Leong, Y., Iongh, J.E. De, Oil, M., Gas, A.S., Bähring, S., Tuxen, A.K., Nielsen, T.B., 2015. SPE-174832-MS Estimation of Fracture Volume Between Well Pairs Using Deuterium Tracer.

Li, L., Jiang, H., Wu, K., Li, J., Chen, Z., 2019. An analysis of tracer flowback profiles to

reduce uncertainty in fracture-network geometries. J. Pet. Sci. Eng. 173, 246–257. https://doi.org/10.1016/j.petrol.2018.10.023

Li, L., Pinprayong, V., Ksp, W., 2017. SPE-189273-MS Fracture Network Evaluation Using Tracer Flowback : A Case Study.

Liang, F., Sayed, M., Al-Muntasheri, G.A., Chang, F.F., Li, L., 2016. A comprehensive review on proppant technologies. Petroleum 2, 26–39. https://doi.org/10.1016/j.petlm.2015.11.001

Lindsay, G., Miller, G., Xu, T., Shan, D., Baihly, J., 2018. Production performance of infill horizontal wells vs. Pre-existing wells in the major US unconventional basins. Soc. Pet. Eng. - SPE Hydraul. Fract. Technol. Conf. Exhib. 2018, HFTC 2018. https://doi.org/10.2118/189875-ms

Manchanda, R., 2015. A General Poro-Elastic Model for Pad-Scale Fracturing of Horizontal Wells.

Manchanda, R., Bhardwaj, P., Hwang, J., Sharma, M.M., 2018. Parent-Child Fracture Interference: Explanation and Mitigation of Child Well Underperformance. SPE Hydraul. Fract. Technol. Conf. Exhib. 23–25. https://doi.org/10.2118/189849-MS

Manchanda, R., Sharma, M.M., Holzhauser, S., 2014. Time-Dependent Fracture-Interference Effects in Pad Wells. SPE Prod. Oper. 29, 274–287. https://doi.org/10.2118/164534-PA

Manchanda, R., Sharma, M.M., Rafiee, M., Ribeiro, L.H., 2017. Overcoming the impact of reservoir depletion to achieve effective parent well refracturing, in: SPE/AAPG/SEG Unconventional Resources Technology Conference 2017.

Unconventional Resources Technology Conference (URTEC), p. 233DUMMY. https://doi.org/10.15530/urtec-2017-2693373

Mayerhofer, M.J., Lolon, E., Warpinski, N.R., Cipolla, C.L., Walser, D.W., Rightmire, C.M., 2010. What Is Stimulated Reservoir Volume? SPE Prod. Oper. 25, 16–18. https://doi.org/10.2118/119890-PA

Meyer, B.R., 2013. SPE 165702 Key Parameters Affecting Successful Hydraulic Fracture Design and Optimized Production in Unconventional Wells. Bazan Consulting, Inc, SPE and Bill C. Brinzer, Baker Hughes, Inc., SPE.

Miller, G., Lindsay, G., Baihly, J., Xu, T., 2016. Parent Well Refracturing : Economic Safety Nets in an Uneconomic Market The Rising Number of Infill Wells. Cc 5–6. https://doi.org/10.2118/180200-MS

Monteagudo, J.E.P., Firoozabadi, A., 2004. Control-volume method for numerical simulation of two-phase immiscible flow in two- and three-dimensional discrete-fractured media. Water Resour. Res. 40, 1–20. https://doi.org/10.1029/2003WR002996

Morel, S., Schmittbuhl, J., Bouchaud, E., Valentin, G., 2000. Scaling of crack surfaces and implications for fracture mechanics. Phys. Rev. Lett. 85, 1678–1681. https://doi.org/10.1103/PhysRevLett.85.1678

Mulkern, M., Asadi, M., McCallum, S., 2010. Fracture extent and zonal communication evaluation using chemical gas tracers. SPE East. Reg. Meet. 156–169. https://doi.org/10.2118/138877-MS

Okouma Mangha, V., Guillot, F., Sarfare, M., San, V., Ilk, D., Blasingame, T.A., 2011.

Estimated Ultimate Recovery (EUR) as a Function of Production Practices in the Haynesville Shale, in: SPE Annual Technical Conference and Exhibition. https://doi.org/10.2118/147623-MS

Open CFD, 2013. OpenFOAM user guide. OpenFOAM Foundation.

Panichelli, P., Martínez, J.R., Crespo, P., Noguera, I.L., Chatterjee, M., 2017. Advanced Reservoir Characterization in Vaca Muerta using Chemical Tracer Technology. SPE Abu Dhabi Int. Pet. Exhib. Conf. https://doi.org/10.2118/188923-MS

Raterman, K.T., Farrell, H.E., Mora, O.S., Janssen, A.L., Busetti, S., McEwan, J., Roy, B., Friehauf, K., Rutherford, J., 2018. Sampling a Stimulated Rock Volume: An Eagle Ford Example. American Association of Petroleum Geologists AAPG/Datapages. https://doi.org/10.15530/urtec-2017-2670034

Robinson, B.M., Holditch, S.. A., Whitehead, W.S., 1988. Minimizing Damage to a Propped Fracture by Controlled Flowback Procedures. J. Pet. Technol.

Rojas, D., Lerza, A., Corp, C., 2018. Horizontal Well Productivity Enhancement through Drawdown Management Approach in Vaca Muerta Shale, in: SPE Canada Unconventional Resources Conference. Calgary, p. 189822. https://doi.org/10.2118/189822-MS

Roussel, N.P., Agrawal, S., 2017. Introduction to Poroelastic Response Analysis – Quantifying Hydraulic Fracture Geometry and SRV Permeability from Offset-Well Pressure Data. Proc. 5th Unconv. Resour. Technol. Conf. https://doi.org/10.15530/urtec-2017-2645414

Roussel, N.P., Florez, H.A., Rodriguez, A.A., 2013. Hydraulic fracture propagation from

infill horizontal wells, Proceedings - SPE Annual Technical Conference and Exhibition. https://doi.org/10.2118/166503-ms

Saad, Y., 1994. ILUT: A dual threshold incomplete LU factorization. Numer. Linear Algebr. with Appl. 1, 387–402. https://doi.org/10.1002/nla.1680010405

Saad, Y., Schultz, M.H., 1986. GMRES: A Generalized Minimal Residual Algorithm for Solving Nonsymmetric Linear Systems. SIAM J. Sci. Stat. Comput. 7, 856–869. https://doi.org/10.1137/0907058

Sardinha, C., Petr, C., Lehmann, J., Pyecroft, J., Merkle, S., 2015. Determining interwell connectivity and reservoir complexity through fracturing pressure hits and production-interference analysis. J. Can. Pet. Technol. 54, 88–91. https://doi.org/10.2118/171628-MS

Sarna, A., Xing, Q., Mork, J., Ershaghi, I., 2014. Impact of fracture closure on productivity decline of unconventional wells, in: Society of Petroleum Engineers - SPE Western North American and Rocky Mountain Joint Meeting. https://doi.org/10.2118/169590-ms

Seth, Puneet;Manchanda, Ripudaman;Zheng, Shuang;Gala,Deepen;Sharma, M., 2019. Poroelastic Pressure Transient Analysis: A New Method for Interpretation of Pressure Communication between Wells during Hydraulic Fracturing, in: SPE International Hydraulic Fracturing Technology Conference & Exhibition. p. 21.

Seth, P., Kumar, A., Manchanda, R., Shrivastava, K., Sharma, M.M., 2018a. Hydraulic Fracture Closure in a Poroelastic Medium and its Implications on Productivity. ARMA18 - 52nd US Rock Mech. / Geomech. Symp.

Seth, P., Kumar, A., Shrivastava, K., Sharma, M.M., 2019. Pressure Interference between Fractured Horizontal Wells: Impact of Complex Fracture Growth on Offset Well Pressure Measurements, 53rd US Rock Mechanics/Geomechanics Symposium held in New York, NY, USA.

Seth, P., manchanda, R., Kumar, A., Sharma, M., 2018b. Estimating Hydraulic Fracture Geometry by Analyzing the Pressure Interference Between Fractured Horizontal Wells.

Sharma, M.M., Manchanda, R., 2015. The Role of Induced Un-propped (IU) Fractures in Unconventional Oil and Gas Wells. SPE Annu. Tech. Conf. Exhib. https://doi.org/10.2118/174946-MS

Sheibani, F., Olson, J.E., 2013. Impact of Fracture Height on Mixed Mode Fracture Propagation: Insights from 3D Displacement Discontinuity Modeling, in: 47th U.S. Rock Mechanics/Geomechanics Symposium. San Francisco.

Shiriyev, J., 2018. A tri-axial electromagnetic induction tool for hydraulic fracture diagnostics. The University of Texas at Austin.

Shou, K.-J., Siebrits, E., Crouch, S.L., 1993. A higher order displacement discontinuity method for three-dimensional elastostatic problems. Int. J. Rock Mech. Min. Sci. 34, 317–322. https://doi.org/10.1016/s0148-9062(96)00052-6

Shrivastava, K., 2019. Hydraulic Fracture Modeling in Naturally Fractured Reservoirs. The University of Texas at Austin.

Shrivastava, K., Agrawal, S., Kumar, A., Sharma, M.M., 2018a. 3-D Interactions of Hydraulic Fracture with Natural Fracture, in: SPE International Hydraulic Fracturing

Technology Conference & Exhibition.

Shrivastava, K., Hwang, J., Sharma, M., 2018b. Formation of Complex Fracture Networks in the Wolfcamp Shale: Calibrating Model Predictions with Core Measurements from the Hydraulic Fracturing Test Site. SPE Annu. Tech. Conf. Exhib. https://doi.org/10.2118/191630-MS

Shrivastava, K., Sharma, M.M., 2018a. Mechanisms for the Formation of Complex Fracture Networks in Naturally Fractured Rocks. Woodlands, pp. 23–25.

Shrivastava, K., Sharma, M.M., 2018b. Proppant Transport in Complex Fracture Networks 23–25.

Spencer, J., Bucior, D., Catlett, R., Lolon, E., 2013. Evaluation of Horizontal Wells in the Eagle Ford Using Oil-Based Chemical Tracer Technology to Optimize Stimulation Design. 2013 SPE Hydraul. Fract. Technol. Conf. https://doi.org/10.2118/163846-MS

Tian, W., Shen, T., Liu, J., Wu, X., 2016. SPE-181857-MS Hydraulic Fracture Diagnosis Using Partitioning Tracer in Shale Gas Reservoir Analytical Methodolog i.

Van Dam, D.B., De Pater, C.J., Romijn, R., 2000. Analysis of hydraulic fracture closure in laboratory experiments. SPE Prod. Facil. 15, 151–158. https://doi.org/10.2118/65066-PA

Walser, D., Siddiqui, S., 2016. Quantifying and mitigating the impact of asymmetric induced hydraulic fracturing from horizontal development wellbores, in: Proceedings - SPE Annual Technical Conference and Exhibition. pp. 26–28. https://doi.org/10.2118/181656-ms

Wang, F., Zhang, S., 2014. Production Analysis of Multi-Stage Hydraulically Fractured

Horizontal Wells in Tight Gas Reservoirs. J. Geogr. Geol. 6, 58. https://doi.org/10.5539/jgg.v6n4p58

Wang, H., Sharma, M.M., 2018. Modeling of hydraulic fracture closure on proppants with proppant settling. J. Pet. Sci. Eng. 171, 636–645. https://doi.org/10.1016/j.petrol.2018.07.067

Wang, H., Yi, S., Sharma, M.M., 2017. A computationally efficient approach to modeling contact problems and fracture closure using superposition method. https://doi.org/10.1016/j.tafmec.2017.09.009

Warpinski, N., Kramm, R.C., Heinze, J.R., Waltman, C.K., 2005. Comparison of Single- and Dual-Array Microseismic Mapping Techniques in the Barnett Shale. Society of Petroleum Engineers (SPE), pp. 9–12. https://doi.org/10.2118/95568-ms

Warpinski, N.R., Teufel, L.W., 1987. INFLUENCE OF GEOLOGIC DISCONTINUITIES ON HYDRAULIC FRACTURE PROPAGATION. JPT, J. Pet. Technol. 39, 209–220. https://doi.org/10.2118/13224-pa

Weng, X., Kresse, O., Cohen, C., Wu, R., Gu, H., 2011. Modeling of Hydraulic Fracture Network Propagation in a Naturally Fractured Formation. Simulation i, 368–380. https://doi.org/10.2118/140253-MS

Whitfield, T., Hunter Watkins, M., James Dickinson, L., 2018. Pre-loads: Successful mitigation of damaging frac hits in the eagle ford. Proc. - SPE Annu. Tech. Conf. Exhib. 2018-Septe, 24–26. https://doi.org/10.2118/191712-ms

Wilson, K., Ahmed, I., Macivor, K., 2016. Geomechanical Modeling of Flowback Scenarios to Establish Best Practices in the Midland Basin Horizontal Program 1–3.

https://doi.org/10.15530/urtec-2016-2448089

Wood*, T., Leonard, R., Senters, C., Squires, C., Perry, M., 2018. Interwell Communication Study of UWC and MWC Wells in the HFTS, in: Proceedings of the 6th Unconventional Resources Technology Conference. https://doi.org/10.15530/urtec-2018-2902960

Wood, T., Leonard, R., Senters, C., Squires, C., Perry, M., 2018. Interwell communication study of UWC and MWC wells in the HFTs, in: SPE/AAPG/SEG Unconventional Resources Technology Conference 2018, URTC 2018. Unconventional Resources Technology Conference (URTEC). https://doi.org/10.15530/urtec-2018-2902960

Wu, K., Olson, J.E., 2014. Mechanics Analysis of Interaction Between Hydraulic and Natural Fractures in Shale Reservoirs, in: Proceedings of the 2nd Unconventional Resources Technology Conference. American Association of Petroleum Geologists, Tulsa, OK, USA. https://doi.org/10.15530/urtec-2014-1922946

Wu, W., Kakkar, P., Zhou, J., Russell, R., Sharma, M.M., 2017. An Experimental Investigation of the Conductivity of Unpropped Fractures in Shales. SPE Hydraul. Fract. Technol. Conf. Exhib. https://doi.org/10.2118/184858-MS

Xu, T., Zheng, W., Baihly, J., Dwivedi, P., Shan, D., Utech, R., Miller, G., 2018. Permian basin production performance comparison over time and the parent-child well study. Soc. Pet. Eng. - SPE Hydraul. Fract. Technol. Conf. Exhib. 2019, HFTC 2019 1–38. https://doi.org/10.2118/194310-ms

Xu, Y., Filho, J.S.A.C., Yu, W., Texas, A., 2016. Discrete-Fracture Modeling of Complex Hydraulic-Fracture Geometries in Reservoir Simulators. SPE Reserv. Eval. Eng. SPE-

183647, 1–21. https://doi.org/10.2118/183647-PA

Zemel, B., 1995. Tracers in the Oil Field. Dev. Pet. Sci. https://doi.org/10.1016/S0376-7361(06)80001-4

Zhang, P., Shiriyev, J., Sharma, M., 2019. Fast Inversion of Downhole Electrical Measurements for Proppant Mapping Using Very Fast Simulated Annealing. SEG Geophys.

Zheng, S., Manchanda, R., Sharma, M.M., 2019a. Development of A Fully Implicit 3D Geomechanical Fracture Simulator. J. Pet. Sci. Eng. submitted. https://doi.org/https://doi.org/10.1016/j.petrol.2019.04.065

Zheng, S., Manchanda, R., Sharma, M.M., 2019b. Development of a fully implicit 3-D geomechanical fracture simulator. J. Pet. Sci. Eng. 179, 758–775. https://doi.org/10.1016/j.petrol.2019.04.065